Alpine sensor network system for high-resolution spatial snow and runoff estimation

by

Sami Andrew Malek

A dissertation submitted in partial satisfaction of the

requirements for the degree of

Doctor of Philosophy

in

Civil and Environmental Engineering

in the

Graduate Division

of the

University of California, Berkeley

Committee in charge:

Professor Steven D. Glaser, Chair
Professor Alexandre M. Bayen
Professor Kristofer J. Pister

Fall 2019

Alpine sensor network system for high-resolution spatial snow and runoff estimation

Abstract

Alpine sensor network system for high-resolution spatial snow and runoff estimation

by

Sami Andrew Malek

Doctor of Philosophy in Civil and Environmental Engineering

University of California, Berkeley

Professor Steven D. Glaser, Chair

Monitoring the snowpack is crucial for water management, flood control and hydropower optimization. Traditional regression methods often result in low accuracy runoff predictions. Existing ground-based real-time measurement systems are in majority installed at low elevations with poor physiographic representation. This thesis presents a system for better Snow Water Equivalent (SWE) and runoff estimation. The autonomous end-to-end Wireless Sensor Network (WSN) that leverages the Internet of Things (IoT) technology provides mountain hydrology measurements in near real-time. At its core lies an ultra-low power, radio channel-hoping, and self-organizing mesh secured with a rugged weather-sealed design, data replication and remote network health monitoring. Three WSNs are installed throughout the North Fork of the Feather River in Northern California upstream of the Oroville dam. Elevation, aspect, slope and vegetation determine network locations. Data show considerable spatial variability of snow depth, and that existing operational autonomous systems are non-representative spatially, with biases reaching up to 50%. Combined with existing systems, WSNs better detect precipitation timing and phase, monitor sub-daily dynamics of infiltration and surface runoff, and inform hydro power managers about actual ablation and end-of-season date across the landscape. A wet and dry year exhibit strong multi-scale inter-year spatial stationarity with major rank conservation. Elastic Net regression shows that dominant features at the sub-km^2 scale are site-dependent and differ from the watershed scale. Based on the Nearest Neighbor (NN) with a Landsat assimilated historical product, explanatory variables consistently explain up to 90% of the variance in the watershed-scale SWE for both years. Lagged cross correlation of snowmelt with stream flow measurements show improvement of up to 100% compared to existing systems. Ensemble Optimal Interpolation (EnOI) update of background SWE fields from Landsat and LiDAR products provide accurate high resolution estimates of spatial SWE for areas with parsimonious sensors. Results show a minimum RMSE of 22% and 30% at 90 m and 50 m resolutions respectively. Compared with SNODAS, reduction in error is up to 55% and 80%, with LiDAR as reference.

To my family and friends.

Contents

Contents **ii**

List of Figures **v**

List of Tables **ix**

1 Introduction **1**
1.1 Background and motivation 1
1.1.1 Existing methods and their limitations 1
1.1.2 Research objectives 3
1.1.3 Thesis contributions 3
1.1.4 Document organization 5

2 Real-Time alpine measurement system using wireless sensor networks **7**
2.1 Introduction 7
2.2 Materials and methods 8
2.2.1 Hardware 8
2.2.2 Low-Power wireless mesh network 12
2.2.3 Software architecture 12
2.2.4 Deployment strategy 16
2.3 Results 18
2.3.1 Deployments 18
2.3.2 Examples of hydrologic data from WSNs 21
2.3.3 Network performance 27
2.4 Discussion 30
2.4.1 Value of the hydrologic product 31
2.4.2 Design choices: comparison with other wireless solutions 33
2.4.3 Comparison with existing WSN systems for snow monitoring 35
2.4.4 Challenges and lessons learned 37
2.4.5 Future R&D directions 38

3 Wireless sensor networks for improved snow water equivalent estimation and runoff forecast **40**
3.1 Introduction . . . 40
3.2 Materials and methods . . . 43
3.2.1 End-to-End system . . . 43
3.2.2 Data quality control and preparation . . . 44
3.2.3 Inter-Year spatial stationarity . . . 46
3.2.4 Feature selection . . . 47
3.2.5 Added explanatory variables . . . 48
3.2.6 Normalized cross correlation with runoff . . . 49
3.3 Results . . . 51
3.3.1 Spatial representativeness of snow pillows . . . 51
3.3.2 Conservation of inter-year spatial stationarity . . . 52
3.3.3 Feature importance . . . 54
3.3.4 Normalized coefficient of correlation with runoff . . . 61
3.4 Discussion . . . 61
3.5 Conclusion . . . 65

4 Near real-time estimation of high resolution spatial SWE using data blending from scarce in-situ measurements and a historical product **67**
4.1 Introduction . . . 67
4.2 Materials and Methods . . . 69
4.2.1 Ensemble Optimal Interpolation (EnOI) . . . 70
4.2.2 Experimental setup . . . 72
4.3 Results . . . 76
4.3.1 Feather River: from Landsat-derived products . . . 76
4.3.2 Tuolumne River: from LiDAR & Landsat-derived products . . . 79
4.4 Discussion . . . 79
4.4.1 Feather River: from Landsat-derived products . . . 81
4.4.2 Tuolumne River: from LiDAR & Landsat-derived products . . . 82
4.5 Conclusions . . . 83
4.6 Algorithms and datasets reference . . . 84

5 Thesis conclusions and future work **85**
5.1 Thesis conclusions . . . 85
5.2 Future work . . . 88
5.2.1 WSN-based monitoring systems . . . 88
5.2.2 SWE interpolation and runoff estimation . . . 89

Bibliography **91**

A PRISM and features **105**

A.1 Feature details 105

B Supplementary figures for Chapter 3 **107**

C Supplementary figures for Chapter 4 **110**

List of Figures

2.1 The hardware used. Circled numbers refer to specific modules of the system in Section 2.2.1. . . . 9
2.2 Contents of the electronics boxes. . . . 11
2.3 Software architecture (adapted from (Brun-Laguna et al. 2016)). . . . 13
2.4 Excerpt of the SOL registry. . . . 14
2.5 Different encodings of the same example compound SOL object (reproduced from Brun-Laguna et al. (2016)). . . . 15
2.6 Web frontend (Bucks Lake deployment). . . . 16
2.7 Maps of the deployments. . . . 20
2.8 Examples of mid-winter sensor data from Grizzly Ridge (15-Jan-2017 to 01-Mar-2017). Line colors for panels (e) to (h) are the same as panel (a). Because measurements of air temperature and relative humidity show relatively small variability within nodes, panels (b) and (c) only report maximum - minimum range and mean. Solar radiation is only measured at node 1 (pillow). . . . 22
2.9 Examples of spring sensor data from Grizzly Ridge (01-May-2017 to 15-Jun-2017). Line colors for panels (e) to (h) are the same as panel (a). Because measurements of air temperature and relative humidity show relatively small variability within nodes, panels (b) and (c) only report maximum - minimum range and mean. Solar radiation is only measured at node 1 (pillow). Soil moisture and temperature sensors at 25cm depth malfunctioned at both nodes 6 and 8 during the reported periods. These data are therefore missing. . . . 23
2.10 Comparison between snow depth measurements from the WSNs with manual measurements taken by monthly snow courses at the same locations (no snow courses are done at the Bucks Lake site). . . . 26
2.11 The PDR/RSSI "waterfall" plot. . . . 29
2.12 Network stability: the number of path_create and path_delete events generated per day over a month. The top line shows the total number of active links, as a reference. . . . 30

3.1 Feather River watershed elevation map (m) showing the snow-pillows across the basin. Three of the snow pillows (marked in blue) include a Wireless sensor Network. The red demarcation line contours the East Branch sub-basin. The black triangle label indicates where the East Branch flow meter is located. . . . 44
3.2 System architecture 45
3.3 SWE for water years 2017 and 2018 reported by snow pillows, snow courses and WSNs for the three study sites BKL, GRZ and KTL. The grey lines denote the SWE reported by each WSN site sensor node. The grey shading covers the range of those WSN measurements. 51
3.4 Daily coefficient of determination r^2 for the selected features that have high Elastic Net coefficients for water year 2017 at the WSN sites (a) BKL and (b) KTL (shaded colors). The WSN mean SWE scaled to the 0-1 range is added to each sub-figure for reference (solid black line). Shaded areas indicate time spans with not enough valid data. 55
3.5 Daily coefficient of determination r^2 for the top selected features from the Elastic Net fit of the SWE of the snow pillows across the watershed for water years (a) 2017 and (b) 2018. The snow pillows' mean SWE scaled to the 0-1 range is added to each sub-figure in black for reference. Shaded areas indicate time spans with not enough valid data. 56
3.6 Box plot for yearly statistics of the squared Pearson correlation coefficient of features with SWE for each of the sites (KTL is shown here, the rest are in the supplement) and water years. Only features with r^2 greater than 0.1 are included. 57
3.7 Box plot for yearly statistics of the squared Pearson correlation coefficient of features with SWE for the watershed. Only features with r^2 greater than 0.1 are included. 58
3.8 Box plot for yearly statistics of the relative feature importance of the Elastic Net for each of the sites (KTL is shown here, the rest are in the supplement) and water years. Negative coefficients indicate that given feature is negatively correlated to SWE. Only coefficients with relative importance of more than 15% are shown. . 59
3.9 Box plot for yearly statistics of the relative feature importance of the Elastic Net for the watershed. Negative coefficients indicate that given feature is negatively correlated to SWE. Only coefficients with relative importance of more than 15% are shown. 60
3.10 Normalized cross correlation coefficient of the SWE loss (snow melt) reported by each measurement system: snow pillow in yellow and aggregated WSN in blue, with runoff for different lags at (a) GRZ and (b) KTL. 62

4.1 Feather River basin sensor locations overlaid on a 90 meter resolution Digital Elevation Model (DEM). Elevation is in meters above sea level. KTL, GRZ and BKL each include a cluster of roughly 12 sensors (Sami A. Malek et al. 2017). . 74
4.2 Tuolumne basin's 4 snow pillow locations overlaid on a 50 meter resolution DEM. Elevation shown is in meters above sea level. 75

4.3 Feather River *menoi* RMSE as percentage of the daily spatial mean SWE with different ensemble selection for water-years 1998, 2002 and 2016. For each of *menoi_ynn*, *menoic* and *menoi* the covariance is represented by a sample of yearly nearest neighbor maps, climatologic maps and all maps respectively. 78
4.4 Tuolumne basin comparison with existing products. Dashed and solid lines represent products and simulations at 50m and 1km spatial resolution. 80
4.5 Tuolumne's April 1st 2017 1-km resolution spatial distribution of SWE in cm from (a) LiDAR, (b) SNODAS and (c) MENOI_Li. XY coordinates represent the 1-km grid cell number. 81

A.1 PRISM 30-year annual precipitation normal in inches covering period from 1981 to 2010. 105

B.1 BKL 2017 Daily r^2 108
B.2 BKL 2018 Daily r^2 108
B.3 GRZ 2017 Daily r^2 108
B.4 GRZ 2018 Daily r^2 108
B.5 KTL 2017 Daily r^2 108
B.6 KTL 2018 Daily r^2 109
B.7 Watershed Pillows 2017 Daily r^2 109
B.8 Watershed Pillows 2018 Daily r^2 109
B.9 Coefficient of Determination r^2: BKL 2017 109
B.10 Coefficient of Determination r^2: BKL 2018 109
B.11 Coefficient of Determination r^2: GRZ 2017 109
B.12 Coefficient of Determination r^2: GRZ 2018 109
B.13 Relative Feature Importance: BKL 2017 109
B.14 Relative Feature Importance: BKL 2018 109
B.15 Relative Feature Importance: GRZ 2017 109
B.16 Relative Feature Importance: GRZ 2018 109

C.1 Feather River *menoi* RMSE as percentage of the daily spatial mean SWE with different Ensemble selection for water-years 1985, 1986 and 1987. 111
C.2 Feather River *menoi* RMSE as percentage of the daily spatial mean SWE with different Ensemble selection for water-years 1988, 1989 and 1990. 112
C.3 Feather River *menoi* RMSE as percentage of the daily spatial mean SWE with different Ensemble selection for water-years 1991, 1992 and 1993. 113
C.4 Feather River *menoi* RMSE as percentage of the daily spatial mean SWE with different Ensemble selection for water-years 1994, 1995 and 1996. 114
C.5 Feather River *menoi* RMSE as percentage of the daily spatial mean SWE with different Ensemble selection for water-years 1997, 1998 and 1999. 115
C.6 Feather River *menoi* RMSE as percentage of the daily spatial mean SWE with different Ensemble selection for water-years 2000, 2001 and 2002. 116

C.7 Feather River *menoi* RMSE as percentage of the daily spatial mean SWE with different Ensemble selection for water-years 2003, 2004 and 2005. 117
C.8 Feather River *menoi* RMSE as percentage of the daily spatial mean SWE with different Ensemble selection for water-years 2006, 2007 and 2008. 118
C.9 Feather River *menoi* RMSE as percentage of the daily spatial mean SWE with different Ensemble selection for water-years 2009, 2010 and 2011. 119
C.10 Feather River *menoi* RMSE as percentage of the daily spatial mean SWE with different Ensemble selection for water-years 2012, 2013 and 2014. 120
C.11 Feather River *menoi* RMSE as percentage of the daily spatial mean SWE with different Ensemble selection for water-years 2015 and 2016. 121

List of Tables

2.1 Fields contained in a SOL object. 13
2.2 Location and size of deployments. 18
2.3 Sensor station features. 19
2.4 Estimated performance 28
2.5 Measured average PDR over the three deployment sites. 29
2.6 List of neighbors of sensor node 7 at Grizzly Ridge, with link quality and number of associated health reports. The mote does not constantly have two neighbors with high PDR that it can use as parents. It thus has to associate with neighbors with low link quality. Bold nodes are annotated in Fig. 2.7c 31

3.1 Features used in Elastic Net regression. 50
3.2 Changes in percent deviation from mean and relative rank for each sensor node and each site between water year 2017 and 2018. 53

4.1 Peak snow-season error statistics for each ensemble selection method for water years from 1985 to 2016. For each of *ynn* (*menoi_ynn*), *menoic* and *menoi* the covariance is represented by a sample of yearly nearest neighbor maps, climatologic maps and all maps respectively. (1) The last row, last three columns represent the average of the absolute bias metrics. 77

A.1 Source of features used in Elastic Net regression. 106

Acknowledgments

As my program advisor at the Civil Systems department, Prof. Steven D. Glaser was at the forefront of leading during my work on my PhD as student and graduate researcher. I thank him for conceiving and supervising the project, and for his guidance, advising and support even throughout all the bumps and difficulties along this journey. He always found a way. I thank him for encouraging me to train and prepare for the industry as well.

Special thanks to Prof. Babak Ayazifar for having me as graduate student instructor for two semesters in the EECS department.

I would like to thank Prof. Alex Bayen for his advice on this project. His valuable input on data blending and assimilation are much appreciated. I am also grateful for his positive sense of encouragement.

My thanks to Prof. Roger Bales for his guidance in hydrology, for his focused advice that helped me redirect and reshape some of my research.

I want to thank Prof. Kris Pister and Prof. Perry de Valpine as members of my PhD committee for their suggestions during my qualifications examinations. Their kind input helped further define the parameters of my intended study.

This work would not have been possible were not for the support we received from the California Energy Commission through the grant "Improving Hydrological Snowpack Forecasting for Hydropower Generation Using Intelligent Information Systems" (EPC-14-067), the Pacific Gas and Electric Co, the California Department of Water Resources, UC Water, and the UC Graduate Division.

I thank Thomas Watteyne for providing invaluable help and guidance in coding best practices, wireless sensor networks deployment guidance and collaboration on the SOL system. I will also remember all the fun we had together, from Paris to our mountain lions and drone-filming adventures in the Sierra mountains.

Also thanks to Carlos Oroza for his input on the WSN sensor placement locations, to Peter C. Hartsough and Tessa Maurer for managing deployment operations. Many thanks to Francesco Avanzi for his collaboration on water matters and his valuable insights into the hydrologic interpretation of the results and to Keoma Brun-Laguna for his collaboration on the SOL system.

I should not forget to thank Zeshi Zheng who endured with me hours of thorough scientific discussions, to Ziran Zhang for always trying to lift us up with his positive spirit, and to Joe Rungee for being a genuine friend.

Thanks to all those who helped and volunteered in the network deployment including Zeshi Zheng, Tessa Maurer, Amanda Lee, Robert Taylor, Ansel Mcclelland, Katya Rakhmatulina, Wassim Lababidi, Mohammad Tuqan and Ziran Zhang.

Last but not least, I would like to thank my parents for support and encouragement. I would have surely not made it to this point without them.

Chapter 1

Introduction

1.1 Background and motivation

Snow represents the predominant winter land surface cover for 50% of North America, Europe and Asia (Romanov, Gutman, and Csiszar 2000). Together with glaciers, snow provides one-sixth of the world's population with fresh water (Barnett, Adam, and Lettenmaier 2005). As a result, economic valuations of snow resources run in the trillions of dollars (Sturm and Goldstein 2017). Runoff from snowmelt is also an important source of hydropower for populous regions such as the Himalayas in Asia (Laghari 2013), the Sierra Nevada and Rocky Mountains in the Western United States (David E Rheinheimer et al. 2014; Ho et al. 2017), and the Alps in Europe (Finger et al. 2012). As climate change and population growth increase strain on water and energy systems, it is crucial to improve monitoring of the snowpack and snowmelt processes in the world's mountain regions to enhance control and forecasting of water supplies (Zhang, Steven D. Glaser, Watteyne, et al. 2016).

1.1.1 Existing methods and their limitations

Traditional methods of forecasting snowmelt and runoff rely on regressing current conditions against historical data. These approaches, become unreliable in the presence of climate change, especially with the predicted increased frequency of extreme weather events (Milly et al. 2008). More robust alternatives consist of physically-based models such as the Precipitation Runoff Modeling System (PRMS) (Markstrom et al. 2015), ALPINE3D (Lehning et al. 2006), or Snowmelt Runoff Model (SRM) (Martinec et al. 1998). They provide a more realistic representation of water-budget fluxes that ultimately translates into an adaptive decision support system for reservoir management (David E Rheinheimer et al. 2014), water conservation, hydro-power optimization and flood control. These models require a large amount of input data as well as a spatially explicit characterization of basin properties and parameters (Bavera et al. 2014). One of the main challenges is therefore to increase the spatial and temporal resolution of existing monitoring networks to provide the data necessary to improve the accuracy of snowmelt runoff forecasts.

High-resolution real-time sampling and accurate estimation of the snowpack spatial distribution often constitutes the initial conditions (or state) for runoff models that may translate into improved runoff forecast in mountainous regions (Jorg-Hess, Griessinger, and Zappa 2015). As Dozier, Bair, and R. E. Davis (2016) states, spatial snow water equivalent (SWE) estimation is "currently the most important unsolved problem in snow hydrology". Yet, current runoff forecasting in California is largely estimated using statistical regression between historical peak snowpack and streamflow (Rosenberg, Wood, and Steinemann 2011). These approaches lack the necessary physical base to cope with a changing climate that is characterized by an increased frequency of extreme weather and the earlier-than-usual onset of snow melt (California Department of Water Resources 2017; Roger C. Bales et al. 2006; Stewart, Cayan, and Dettinger 2004; Stewart, Cayan, and Dettinger 2005).

Snow distribution in mountains is not spatially homogeneous at any scale and has been shown to depend, during both accumulation and ablation periods, on various physiographic and vegetative features among others. Operational snow pillows, consisting of sparsely scattered point measurements of SWE across California's mountain basins, have been installed and maintained by DWR since the 60s (*Department of Water Resources California Data Exchange Center* n.d.). Snow pillows, lacking spatially representative information on SWE, are complemented by manual monthly snow-course measurements that are often located near the snow pillows. It has been shown that those surveys underestimate peak season snow because peak snow does not regularly occur during those sampling dates (L. Montoya, Dozier, and Meiring 2014). Such techniques suffer from lack of spatio-temporal representativeness and a better sampling approach is needed. Additionaly, practical challenges and difficulties are associated with such measurement techniques. Snow-pillows require a flat surface and are often installed in open areas mostly accessible in lower but less representative locations. Harsh remote environments are isolated from the power grid and thus power consumption is a major limitation for such systems. Manual snow surveys, although more representative, are labor and resource intensive, and not frequent or widespread.

Other techniques such as remote sensing of SWE provide large spatial coverage but suffer from two main limitations. First, cloud cover that is especially prominent during the accumulation season masks most of the desired information. Second, SWE under canopy is not accurately captured. Satellite observations of SWE such as AMSR-E (25 km resolution) are much coarser than the desired resolution. Landsat (30 m resolution) and MODIS (500 m resolution) on the other hand, do not observe SWE but rather fractional snow cover that, by converting to SWE via models, is likely to produce uncertain estimates, especially when pixels are totally saturated with snow. Airborne LiDAR is an attractive remote sensing option in terms of accuracy and spatial resolution, but is limited in range, expensive, and impractical at high temporal resolution.

With the advent of the Internet of Things (IoT) and wireless sensing technology, it has become possible to gather large amounts of mountain hydrologic data, and most importantly SWE, in near real-time and to stream such inputs from remote elevated regions down to the servers in the lab. The development of Wireless Sensor Networks (WSN) has shown to be very promising in collecting and transmitting the needed data. Notwithstanding, many

challenges remain in instrumenting mountainous regions, securing high quality seamless flow of measurements, processing the data, and blending it with available remote sensing products to increase the accuracy of larger spatial-scale Snow Water Equivalent (SWE) estimates and subsequently runoff forecasts.

1.1.2 Research objectives

This thesis presents research that aims at addressing the above hurdles. First, it describes the extent to which a newly developed end-to-end measurement system is able to meet the very taxing demands a rugged mountainous environment poses; how robustly it operates, performs and self-heals; the kind of reports it produces, and how it compares with other measurement methods and similar systems in operation. We present the installation and operation of large-scale wireless sensor networks in the Sierra Nevada Mountains to collect real-time hydrologic parameters such as temperature, humidity, soil moisture, snow depth and solar radiation. This requires developing reliable and scalable software for the cyber physical system. The project builds on and further develops currently operating basin-scale prototype information systems.

Moreover, collecting data that is spatially representative is one important aspect of the implementation of WSNs. Therefore, the second main objective of this research is to evaluate the data from various spatial scales to characterize the determining mountainous and hydrologic features on SWE estimates; such as elevation, slope, aspect and canopy. Also the contribution of the new WSNs in terms of estimating runoff is highlighted in comparison to existing operational measurement systems.

Satellite observations, though tend to have lower temporal resolution and accuracy, are able to show the distribution of snow over topography, which surface measurements do not. Finally, the study aims at advancing and evaluating a method of blending measurements available at different time and space scales (ex: WSNs, MODIS satellite data...), and from sparse sensor data, with historical remote-sensing-based products that would improve the accuracy of basin-scale near-real-time high-resolution spatial SWE estimates. Particularly, this seeks to address the limitations that stem from parsimoniously instrumented areas, a fact still prevalent in the majority of the investigated mountainous regions.

This synergistic integration should culminate in real-time distribution maps of Snow Water Equivalent or Snow Depth and serve to decouple the long standing runoff forecast dependency on climate change affected historical data. The research project outcome would potentially benefit many stakeholders including partnered entities such as the California Energy Commission, the Department of Water Resources and Pacific Gas & Electricity.

1.1.3 Thesis contributions

My approach to tackling the above objectives can be summarized as follows, through a set of core contributions:

Validation of WSN technology for real-time representative sampling of alpine SWE

- We present the hardware and software design of a state-of-the-art distributed Wireless Sensor Network (WSN)-based autonomous measurement system with real-time remote data transmission that gathers data of snow depth, air temperature, air relative humidity, soil moisture, soil temperature, and solar radiation in physiographically representative locations. Elevation, aspect, slope and vegetation are used to select network locations, and distribute sensors throughout a given network location, since they govern snow pack variability at various scales.

- Up to four WSN clusters totaling 48 sensor stations, approximately 120 repeaters and 336 sensors were installed in the Sierra Nevada of Northern California throughout the North Fork of the Feather River, upstream of the Oroville dam and multiple powerhouses along the river. The WSNs succesfully gathered hydrologic variables and network health statistics throughout the 2017 and 2018 water years, the latter being one of northern Sierra's wettest years on record.

- We compare snow data time series collected by the installed clusters with co-located existing manual and autonomous measurement systems.

- An end-to-end software suite is conceived to improve the remote ground measurement system reliability, ease of use and seamless data visualization. A simple and efficient Time-Len-Value packet encoding protocol with compression is used. The network sensing components are upgraded with firmware for minimal power consumption (reaching on average 2 mA with sensors), uncertainty-tagged sensor measurements and automatic data recovery features. Other infrastructure components are augmented to increase the resilience to data loss due to weather and wildlife disturbance and allow for real-time topological visualizations of the network health.

WSN data analysis to quantify results biases of existing monitoring systems and to identify physiographical features that are determinative of SWE spatial variability

- Two years of spatio-temporally dense WSN data collection (15 min and 3x1 km^2) are presented after filtering out noise with the aid of complementary uncertainty measurements.

- The data is used to quantify the measurement biases of exiting snow monitoring systems compared to the installed WSNs, and to inform on the inter-year and intra-year stationarity of spatial snow patterns from the 1 km to the basin-scale.

- Up to 15 features that potentially affect SWE's spatial variability across both the 1 km and basin-scales are evaluated using Elastic Net regression and ranked according to the explained variance.

Demonstrated potential contribution of WSN-based measurement system to runoff forecasting

- The forecasting potential of WSN data retrieved from two WSN sites (KTL and GRZ) is quantified as the lagged cross-correlation of snowmelt with stream flow measurements across different lags in days, and compared to that of the existing snow pillows.

Developed a data assimilation framework for blending real-time in-situ and historical remote-sensing based products to generate basin-scale daily maps of SWE in real-time and at multi-spatial resolutions.

- Presented a scheme aimed at estimating daily spatial SWE maps in real-time and at high spatial resolution from both scarce in-situ SWE measurements from IoT devices at actual sensor locations and historical SWE maps. The method consists of finding a background spatial SWE field, followed by an update step using the Ensemble Optimal Interpolation (EnOI) to estimate the residuals. This first time application of the quantitative EnOI method for SWE interpolation allowed for areas with parsimonious sensors to have accurate estimates of spatial SWE without explicitly discovering and specifying the spatial interpolation features. The framework allows for easy integration of noisy, incomplete and intermittent measurements at various temporal and spatial scales.

- Different schemes of sampling the EnOI ensemble representing the co-variance are studied and compared: selecting the yearly nearest neighbor SWE maps, all available SWE maps, and finally a climatologic sample.

- Evaluated the scheme on California's Feather River basin by generating 30-year daily SWE simulations at 90 m resolution using an existing remote sensing Landsat-assimilated product as the historical dataset determining the covariance. The choice of the historical product allows for swift experiment replication across the entirety of California's Sierra Nevada Mountain chain.

- Evaluated the scheme on California's Tuolumne River basin by generating 4-year biweekly SWE simulations at 50 m resolution using additionally a LiDAR-based product as the historical dataset determining the covariance. Results are presented and compared with three existing methods in the literature, as well as the operational SNODAS.

1.1.4 Document organization

The dissertation is organized in three main chapters that present the detailed objectives for each of the main goals of the research. Each chapter describes the research background, the methods and materials, the results, and the implications for future research and development directions. Chapter 2 describes in details the architecture of the end-to-end SOL system with its embedded four wireless sensor networks developed and operational at various

locations and elevations across the North Fork of the Feather River in Northern California. It presents the deployment phase, and a comprehensive evaluation of the system performance in comparison with other methods and similar systems. The content in this chapter was also published in the journal Sensors (S. Malek et al. 2017).

Chapter Two first deals with the reliability and validity of the data produced by the measurement system for a wet and dry year and compares it to existing co-located systems. It also analyzes the inter-year stationarity and ranking conservation for each network station leveraging data collected from the WSN system presented in Chapter One across two years. Afterwards, existing and newly presented hydrologic and topographic features that explain the spatial distribution and variance of SWE are selected using the Elastic Net linear regression method and their importance determined from the near-real time data. Finally, the potential predictability of runoff from SWE and its dynamics is quantified by means of the normalized cross correlation (NCC) of SWE with natural runoff, at the East Branch of the North Fork of the Feather River where the WSNs have been installed. The content in this chapter was also published in the journal IEEE Access (S. A. Malek, S. D. Glaser, and R. C. Bales 2019).

WSNs currently cannot cover the entirety of the basin of interest due to limited resources. Moreover, very few have been installed relative to the size of the basin which presents a challenge in estimating the basin-wide SWE without additional information. Hence, in Chapter Three, research focus is given to the real-time estimation of high resolution spatial SWE from scarce in-situ observations and is applied on the Feather River and Tuolumne basins. Simulated in-situ observations at actual measurement locations are assimilated into background fields of Landsat and LiDAR-derived historical products using the Ensemble Optimal Interpolation (EnOI) method. Additionally, performances of covariance structures from three different sampling schemes are compared across a 30-year simulation time span at the Feather River. The content in this chapter is to be submitted to the journal AGU Water Resources Research.

Chapter 2

Real-Time alpine measurement system using wireless sensor networks

2.1 Introduction

Current snow measurement systems include *(i)* manual ground-based snow courses (K. Elder, Cline, et al. 2009), which measure single snapshots of snow properties in time at various scales (plot, transect, slope etc.); *(ii)* automated ground-based systems at point scale, such as snow pillows and snow depth sensors (Serreze et al. 1999; Ryan, Doesken, and Steven R Fassnacht 2008; Avanzi et al. 2014; Johnson et al. 2015); and *(iii)* terrestrial and airborne remote sensing products like laser scanning (Prokop et al. 2008; Revuelto et al. 2016; Painter et al. 2016), Unmanned Aerial Vehicles (Bühler et al. 2016; De Michele et al. 2016; Harder et al. 2016), or satellite platforms (Dietz et al. 2012). While automatic ground systems provide data with a relatively high temporal resolution at specific, usually flat and open locations, remote sensing measures snow patterns at larger geographic scales but with coarser temporal and spatial resolutions. Bridging the gap between these two sources of data fulfills the need for both spatially and temporally high-resolution information that current products cannot provide.

This chapter presents a recent deployment of a wireless sensor network (WSN) designed for snow hydrology, a new method of environmental sensing which collects and sends out data every 15 min from sensor node clusters covering tens of hectares. The location of each node corresponds to specific physiographic features known to impact snow distribution like elevation, aspect, slope, and canopy. These WSNs, deployed in the Feather River basin in the California Sierra Nevada (USA), constitutes the second generation of fully wireless systems deployed to the Sierra Nevada and aims primarily at assisting hydropower operations and ultimately water resources management at the State level. The design of first-generation WSNs (Zhang, Steven D. Glaser, Watteyne, et al. 2016) has been renovated to specifically fulfill hydropower real-time forecast needs in snow-dominated contexts. The deployment of these networks is the result of a partnership between the University of California, Pacific

Gas & Electric, California Department of Water Resources, California Energy Commission, and the Institut de recherche en informatique et en automatique.

The remainder of this chapter is organized as follows. Section 2.2 describes the hardware and software design of the deployment, with a focus on how it addresses the resiliency of the system in harsh alpine conditions. Section 2.3 presents two types of results; Hydrologic results include the data collected during water year (WY) 2017, one of Northern California's wettest on record, and Networking results show the performance of the WSNs during this challenging WY based on self-reported network health data. Section 2.4 discusses how this network compares to other wireless sensor networks and traditional snow survey techniques.

2.2 Materials and methods

This section describes all the hardware (Section 2.2.1) and software (Section 2.2.3) in sufficient detail to allow the interested reader to replicate the results. This is greatly simplified as all the software is published under a BSD open-source license[1]. Section 2.2.2 provides necessary information for understanding the low-power wireless networking technology we are using. Section 2.2.4 describes the methodology we employ when deploying a new network, further allowing the interested reader to replicate the results.

2.2.1 Hardware

Four different types of hardware are used in the system:

- Sensor stations (Fig. 2.1a) are installed at physiographically representative locations within network clusters and measures snow and meteorological variables, which are transmitted to the base station.
- In case the sensor station is too far from the base station for direct communication, repeater nodes (Fig. 2.1b) are installed to serve as data relays. They also maintain the redundancy of a full mesh network.
- The base station (Fig. 2.1c) serves as a collection point for all the data gathered by the sensor stations, and forwards this data to the server over a cellular Internet link.
- The server receives, stores and displays the data (not shown).

Each type of hardware is detailed in a subsequent section. Circled numbers (e.g. ①) refer to annotations in Fig. 2.1.

[1] https://github.com/realms-team/

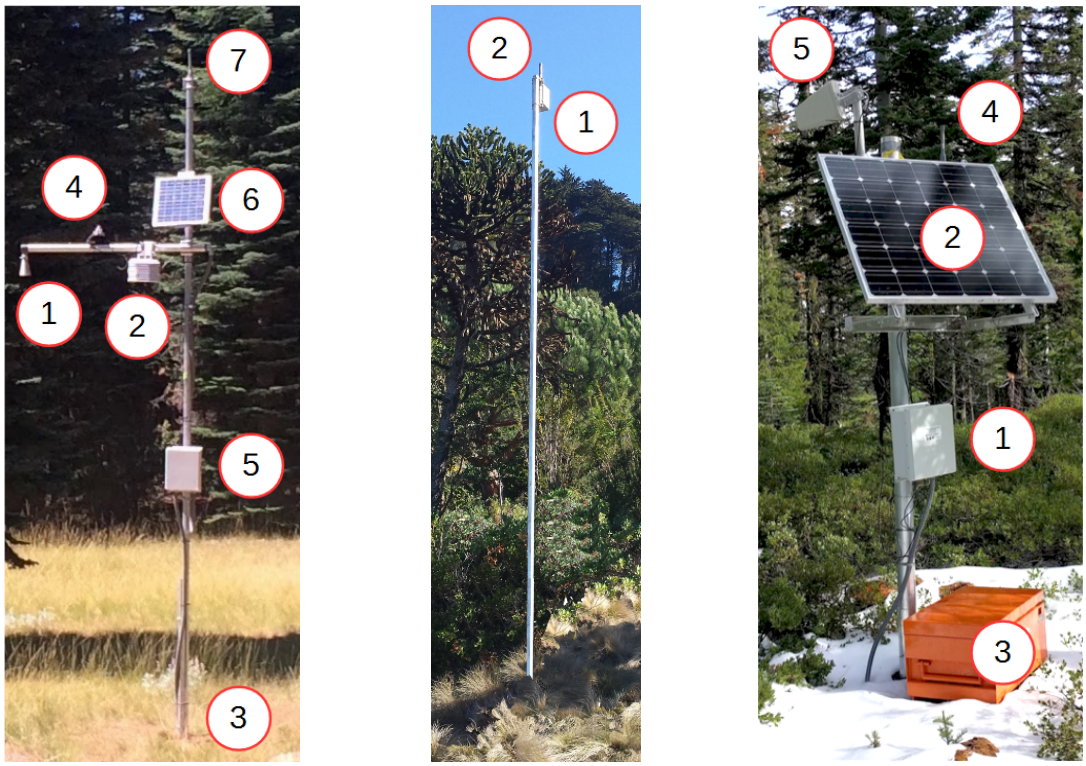

(a) Sensor station (b) Repeater node (c) Base station

Figure 2.1: The hardware used. Circled numbers refer to specific modules of the system in Section 2.2.1.

Sensor station

A sensor station (Fig. 2.1a) consists of a 5 m high schedule 80 aluminum pole with sensors attached, and a mote to control the sensors, make local calculations and communicate the sensor measurements to the base station. Up to 4 types of sensors can be mounted onto the pole.

- MB7363 Maxbotix ultrasonic range-finder ① can be mounted on the tip of the crossarm, oriented downwards. It measures the distance to ground or snow by measuring the round-trip time of an ultrasonic pulse. It has a resolution of 1 mm, an accuracy of 1%, and a range of 50 cm to 10 m. Like all ultrasonic devices, it is less accurate while it is snowing. We obtain the snow height by subtracting the distance measured when there is no snow.

- Temperature and relative humidity is measured by a Sensirion SHT25 sensor②. It is enclosed in a radiation shield, and mounted about halfway across the crossarm.

- Decagon GS3 soil-moisture sensor ③ which measures soil dielectric constant, electric conductivity and temperature. Soil moisture is more accurately estimated via a calibration relation[2]. Results reported have not been locally calibrated. Two such sensors are installed per sensor station, at depths of 25 cm and 50 cm into the ground.

- Hukesflux LP02 pyranometer solar radiation sensor ④. One solar radiation sensor per WSN is installed in an open area. Unshaded solar radiation tends to be uniform across a 1-2 km^2 area.

A sensor station typically features one ultrasonic range-finder, one temperature and relative humidity sensor, and two soil-moisture sensors (installed at different depths). In addition, one sensor station in the deployment features a solar radiation sensor.

These sensors are connected through wires to a NeoMote. The NeoMote by Metronome Systems[3] is a multi-purpose, ultra-low mote. It features a 16-bit ARM programmable system on chip (PSOC), a versatile micro-controller capable to interfacing to virtually any sensor and actuator. Up to 40 different types of sensors can be interfaced to the PSOC. It also features a SmartMesh IP wireless module by Analog Devices, allowing it to transfer its sensor measurements to the base station in a reliable, ultra low-power and secure way. Additionally, the NeoMote contains an SD card for local backup, and a real-time clock (RTC) for timestamping. The NeoMote and sensor are powered by a 17 Ah Li-Ion battery, which is recharged by a solar panel ⑥. A 2.4 GHz, 4 dBi, omnidirectional antenna is mounted on the top of the pole ⑦ to allow the wireless module to communicate.

To install a sensor station, a steel U-channel is concreted into the ground. The main pole is then bolted onto the U-channel. This setup allows the pole to be removed when needed. All the electronics are housed in a waterproof NEMA 4 fiberglass enclosure ⑤ attached to the pole. All sensor and solar panel wires are routed to the electronics box via the crossarm and metal-reinforced conduit to prevent exposure to weather and wildlife. They enter the box through conduit holes at the bottom of the box to prevent water from leaking into the enclosure. The cross-arm is bolted onto the main pole 4 m from the ground.

Repeater node

The role of the repeater node (Fig. 2.1b) is to provide connectivity between the sensor stations and the base station and maintain the redundancy of the mesh network. Mechanically, it resembles the sensor station: it consists of a 5 m aluminum pole bolted to a U-channel. It is, however, much simpler than a sensor station, as it only contains a waterproof fiberglass enclosure ① with a Metronome Systems Wireless Sensing Relay Board. This node contains only the SmartMesh IP wireless module and is powered by a 17 Ah primary battery. An antenna is mounted on the top of the box ②.

[2] `http://manuals.decagon.com/Manuals/13822\_GS3\_Web.pdf`

[3] `http://www.metronomesystems.com/`

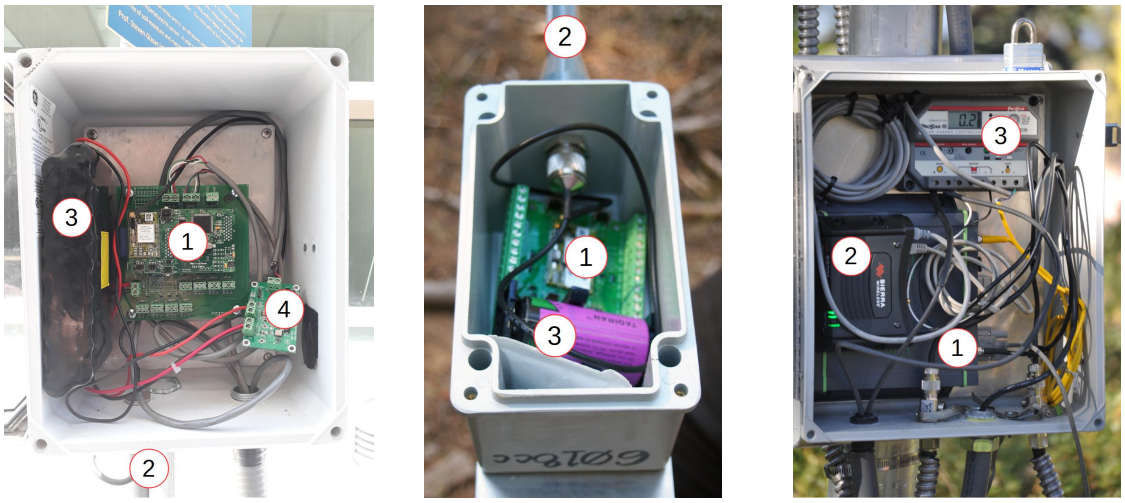

(a) Sensor station (b) Repeater node (c) Base station

Figure 2.2: Contents of the electronics boxes.

Base station

The role of the base station (Fig. 2.1c) is four-fold: *(i)* control and maintain the network, up to 100 nodes; *(ii)* collect the sensor measurements from the sensor stations, *(iii)* locally store the data, and *(iv)* transmit the data to the server on the Internet through a cellular connection.

The base station is built around a 100 mm diameter aluminum pole. The waterproof fiberglass enclosure mounted 1.5 m from the ground contains several elements. First, it contains a Network Manager from Metronome Systems (Fig. 2.2c, ①), which acts as the gateway of the SmartMesh IP network. The Manager contains two main elements: a SmartMesh IP module and a GNU/Linux computer consuming only 50 mA. They are connected to one another by an internal serial interface. This Network Manager uses a 2.4 GHz omni-directional antenna (Fig. 2.1c, ④) to build a multi-hop mesh network with the sensor stations and repeater nodes. Second, it contains a Sierra Wireless AirLink GX450 cellular modem (Fig. 2.2c, ②) for the Manager to connect to the Internet. This modem uses a directional antenna (Fig. 2.1c, ⑤) which is pointed at the nearest cell phone tower. Manager and cellular modem are connected over Ethernet. Combined, the electronics consume around 200 mA. A 150 W solar panel (Fig. 2.1c, ②) is used to charge two deep-cycle 66 Ah rechargeable sealed batteries which are enclosed in a Rigid box (Fig. 2.1c, ③).

Server

The role of the server (Fig. 2.1c) is three-fold: *(i)* receive the data sent by the base stations of multiple deployments, *(ii)* store the data in a database, and *(iii)* offer a web interface to navigate and download the data. The server is rack-mounted and located at UC Berkeley.

It is equipped with an 3 GHz Intel Core i7 CPU, a 1 TB drive, and 8 GB of RAM memory.

2.2.2 Low-Power wireless mesh network

Each device (sensor station, repeater node, base station) is equipped with the same SmartMesh IP LTC5902-IPM[4] wireless module. This module contains a combined radio and micro-controller system-on-chip, an antenna connector, and all required passives and crystals. It comes pre-programmed and takes care of all the networking aspects. It either runs entirely standalone ("master" mode) or can be driven by an external micro-controller through a serial interface ("slave" mode).

When switched on, all of these devices form a low-power wireless multi-hop mesh network. The fact that it is multi-hop means that if a sensor station is too far from the base station to transmit its data directly, other device(s) serve as relays. Both sensor stations and repeater nodes can relay data; they are equivalent from a networking point of view. The fact that the network is a mesh means that a device connects with multiple other devices, providing redundancy, which leads to high end-to-end reliability. A device can make an arbitrary number of connections, meaning that theoretically, the mesh could have hundreds of devices and excessive redundancy. However, to balance trade-offs like cost, logistics, and limiting the network's footprint, we aimed to provide each node with at least two parent nodes to prevent single path failures. More information is available in Section 2.2.4. Fig. 2.7 shows snapshots of the mesh network topology on three deployments (detailed description in Section 2.3.1).

In a SmartMesh IP network, all devices are tightly synchronized, with a maximum device-to-device de-synchronization below 15 μs across the network. Time is sliced up into slots; all communication in the network is orchestrated by a communication schedule. The schedule indicates to each node what to do in each time slot: transmit, listen or sleep. This allows the network to avoid internal interferences and keeps the energy consumption down. The network continuously optimizes the network, automatically making adjustments to the schedule when needed (e.g. a new device needs to publish more data, a wireless link breaks, etc). A SmartMesh IP network is expected to yield over 99.999% end-to-end reliability. With an average current consumption below 50 μA, a device operates for over a decade when powered by a pair of AA batteries. Examples of applications of the time synchronization used by a SmartMesh IP network are detailed in Watteyne, Weiss, et al. (2015) and K. S. J. Pister and Doherty (2008). The NIST-certified security provides confidentiality, integrity, and authentication to the communication.

2.2.3 Software architecture

The Sensor Object Library (SOL) software architecture was fully developed for the deployments described in this article. The details about SOL System have been previously pub-

[4] `http://www.linear.com/product/LTP5902-IPM` SmartMesh IP Wireless 802.15.4e PCBA Module with Antenna Connector

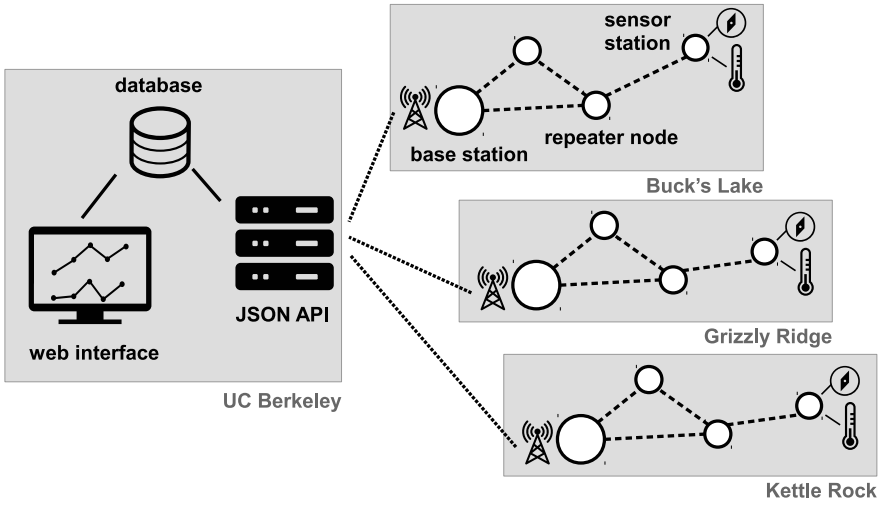

Figure 2.3: Software architecture (adapted from (Brun-Laguna et al. 2016)).

Table 2.1: Fields contained in a SOL object.

M	address of the device which created the object
T	timestamp of when the object was created
t	type of the object, as defined in the SOL registry
L	length of the value field
V	value of the object

lished in (Brun-Laguna et al. 2016). This section provides the necessary overview, illustrated by Fig. 2.3.

SOL resides in four different locations: the sensor station (Section 2.2.3), the repeater node (Section 2.2.3), the base station (Section 2.2.3) and the server (Section 2.2.3). All the code developed is provided under a BSD open-source license[5]. The code is being developed using state-of-the-art software development project management tools, and is production-ready.

Sensor Object Library (SOL)

The driving concept in the design of SOL is that each sensor measurement or network statistics is represented as an atomic SOL object. Conceptually, this self-contained SOL object is formed by the fields listed in Table 2.1. This format is an equivalent to the well-known Type-Length-Value (TLV) scheme, to which we have added address and timestamp fields.

A publicly-maintained SOL registry[6] lists the different SOL object types, and for each

[5]As an online addition to this paper, all source code can be found at `https://github.com/realms-team`.
[6]`https://github.com/realms-team/sol/blob/master/registry.md`

```
{
        'type':         SOL_TYPE_TEMPRH_SENSERION_SHT25_RS232_RAW,
        'description':  'Sensirion SHT25 SOL object format',
        'structure':    '>II',
        'fields':       ['temp', 'rH'],
},
```

Figure 2.4: Excerpt of the SOL registry.

the format of the value **V**. Fig. 2.4 shows an excerpt of the SOL registry, on the format of a SOL object corresponding to the Sensirion SHT25 temperature and humidity sensor. It indicates that the value **V** field is 4 bytes long: a 2 byte temperature value followed by a 2 byte relative humidity value. The SOL registry currently contains 55 entries.

A SOL object can be encoded in 2 different formats, and example of which is shown in Fig. 2.5. When the sensor station generates a SOL object, it encodes it in a compact binary format, typically 10-50 bytes. This is what the sensor station writes into the packets it sends to the base station across the low-power wireless mesh network. The base station converts the binary encoding into the equivalent JSON encoding. JSON (Bray 2014) is a text-based encoding ubiquitous in machine-to-machine communication on the Internet, and well-supported by tools, including the database and web interface on the server.

We have developed Python and C core libraries to manipulate SOL objects, including serialization, de-serialization, conversion and validation routines. The software running on the sensor station, base station and server builds around these libraries.

Sensor station firmware

The SmartMesh IP module of the sensor stations comes pre-programmed. The only modification applied is that it is configured to operate in "slave" mode, allowing the PSOC to drive it over a serial port. It is also configured to automatically join the network. The PSOC firmware handles the following basic tasks: *(i)* it samples the different external sensors; *(ii)* it saves those measurements locally on the SD card; *(iii)* it sends that information to the SmartMesh IP module. These different steps are executed every 15 min; between those activity periods, the PSOC is in ultra low-power mode. The PSOC also implements advanced features, such as the ability to request the sensor station to resend some of the previous measurements stored on its SD card. The firmware comes with a library of drivers for the different sensors. Reading a sensor can be as simple as reading a single value over a digital bus (this is the case for example for the Sensirion temperature/humidity sensors). More advanced drivers include the one of the ultrasonic range finder, which triggers 28 snow depths measurements and reports their filtered average and standard deviation.

```
20 00 17 0d 00 00 18 ac
50 06 e0 52 9d 21 00 1A
00 17 0d 00 00 18 22 60
09 BB 35 43 21 00 15
```

(a) binary encoding *(31 bytes)*

```
[
  {
    "mac":
"00-17-0d-00-00-18-ac-50",
    "timestamp": 115364509,
    "type":      33,
    "value":     26
  },
  {
    "mac":
"00-17-0d-00-00-18-22-60",
    "timestamp": 163263811,
    "type":      33,
    "value":     21
  }
]
```

(b) JSON encoding *(156 bytes)*

Figure 2.5: Different encodings of the same example compound SOL object (reproduced from Brun-Laguna et al. (2016)).

Repeater node configuration

The repeater node's SmartMesh IP module comes pre-programmed as well. We configure it so it runs in "master" mode: it joins and participates in the network without needing to be driven by an external micro-controller.

Base station software

The SmartMesh IP module of the base station comes pre-programmed as manager for up to 100 nodes, and is used as-is. The GNU/Linux computer, running a Debian Jessie instance, handles the following tasks: *(i)* it drives the cellular modem connected to it; *(ii)* it waits for notifications from the SmartMesh IP manager, containing the sensor measurements generated by the sensor stations; *(iii)* it stores those notifications locally in a back-up file; *(iv)* it converts the SOL objects contained in the notifications from their binary to their JSON encoding; *(v)* it sends these objects to the server. The cellular modem is configured to switch to low power standby mode when its input voltage drops below a threshold of 11V.

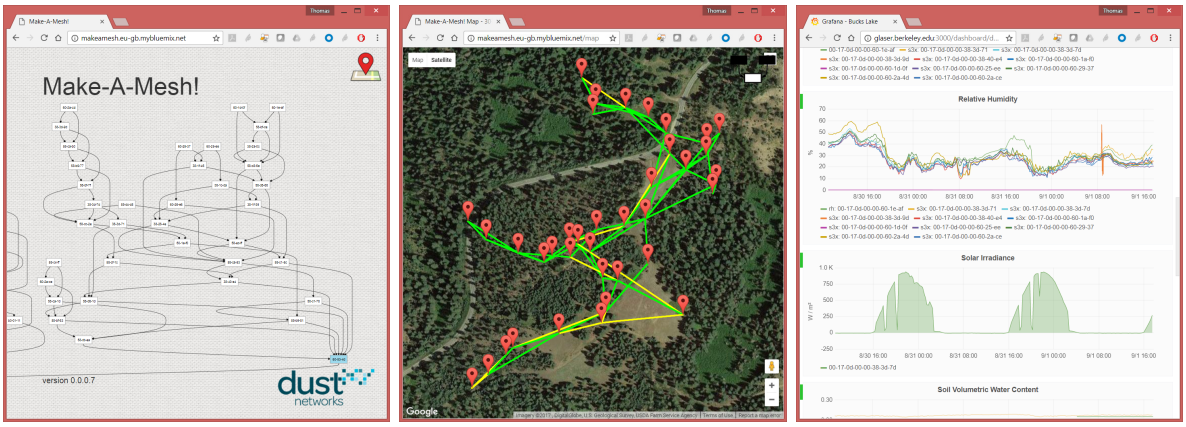

(a) Topology view (b) Map view (c) Data view

Figure 2.6: Web frontend (Bucks Lake deployment).

Server software

The server runs Ubuntu 14.04.1 LTS, a flavor of GNU/Linux. Three base services are deployed: *(i)* a Python-based program offers a RESTful HTTPS/JSON interface for base stations to send their data to; *(ii)* an InfluxDB time series database[7] holds all the SOL objects; *(iii)* a Grafana web frontend[8] allows a user to navigate the data. The server builds a web frontend on top of these base services, allowing the user to see the logical topology of the network (Fig. 2.6a), see the map of the network (Fig. 2.6b), and navigate the sensor data (Fig. 2.6c).

2.2.4 Deployment strategy

The deployment strategy can be subdivided into four components: site selection, base station siting, sensor station placement, and repeater placement.

Site selection. At the highest level, the goal is to identify one or multiple deployment sites. A deployment site is roughly 1 km^2. Our site selection process over the Feather River was driven by a desire to expand current monitoring capabilities on the North Fork, where most of the powerhouses are located, with particular focus on the under-monitored and largely undeveloped East Branch. Networks were chosen to be co-located with existing snow pillows that measure snow water equivalent (SWE). These sites where chosen by our partners Pacific Gas & Electric. Co-located SWE measurements enable better estimation of snow-water storage across the landscape. Sites were chosen to sample along a large elevation gradient, as hydrological processes in mountainous regions are driven by factors that change with elevation. Finally, sites were selected to capture hydrologic variability induced from

[7] `https://www.influxdata.com/`
[8] `https://grafana.com/`

a ridge that produces a rain shadow between the North Fork and the East Branch of the Feather River.

Base station siting. Once a deployment site is identified, the next step is to survey the 1 km^2 area and identify where there is cellular connectivity, if any. Field teams survey the proposed network sites with a cellular modem attached to a directional antenna. The base station is placed where there is high cellular connectivity, as close as possible to the center of the field site. This minimizes the number of hops to the farthest nodes in the final mesh network, thereby reducing power consumption and increasing reliability. If no cellular connectivity is found, the back-up option is to use a satellite connection.

Sensor station placement. Once the possible locations for the base station are identified, the next step is to identify the locations of the sensor stations. This is done based on a combination of hydrologic and network considerations. The goal is to identify 12 locations[9] within the 1 km^2 deployment area which capture the variability of variables known to affect snow cover: slope, aspect, vegetation and elevation. This is done by a machine-learning program developed in our laboratory (Oroza, Zheng, et al. 2016). An additional constraint is that, given multiple potential sensor station locations, we prefer locations that are close to the base station to limit the number of repeaters. One node per site was installed at the same location of the snow pillow to enable direct comparisons between our measurements of snow depth and pillow SWE (henceforth, this node is referred to as the pillow node). At the same location, a rain gauge is usually available.

Repeater placement. Once the position of the sensor stations and the base station is determined, repeaters are added to connect the sensor stations to the base station and establish the network mesh. Prior studies have evaluated strategies for pre-computing optimal repeater placements for wireless mesh networks (Lee and Younis 2012; Mehajabin et al. 2016; Kashyap, Khuller, and Shayman 2006). These methods often rely on simplifying assumptions, such as a flat environment and a fixed transmission range. Such assumptions are too restrictive for wireless-mesh networks in mountain environments, which feature terrain variability, complex spatial patterns of canopy cover, and variable snow depth, all of which affect path quality (Kerkez et al. 2012; Rice and Roger C Bales 2010; Oroza, Zhang, et al. 2017) and cause complicated multi-path effects. In practice, networks must be structured by field teams on the ground using real-time measurements of network health measured at the base station. The base station is placed near the center of the network, so members of the field team start there and build the network out towards each sensor station.

Three priorities guide the field teams' selection of repeater placement: First, placements with an unobstructed path (i.e. free from terrain intersection or canopy cover) are prioritized over paths with obstructions. Second, field teams aim to ensure that the failure of a single node in the mesh cannot disconnect the network (i.e. that the final mesh be 2-vertex connected). This is not always possible if there is a limited budget for repeater placements. Where possible, 1-vertex-connected components of the graph are limited to nodes that are

[9] In the deployments covered in this article, the limit of number of sensor stations per deployment site is 12, based on budgetary considerations.

Table 2.2: Location and size of deployments.

	Bucks Lake	Grizzly Ridge	Kettle Rock
Latitude	39.850000	39.917000	40.140000
Longitude	-121.242000	-120.645000	-120.715000
Deployment area	20 ha	27 ha	42 ha
Num. sensor stations	12	12	12
Num. repeater nodes	22	25	31
Num. base stations	1	1	1
Total num. devices	**35**	**38**	**44**

farthest away from the base station, so failure of the node will only affect a single sensor station. Third, a rule provided by Analog Devices, the manufacturer of the SmartMesh IP solution, requires that each node in the mesh must have at least 3 good neighbors (*SmartMesh IP Application Notes* 2017). A link between two devices is "good" when the quality is above 50%, i.e. over 50% of the packets exchanged between the neighbors are done so without retries. After the deployment, field teams evaluate the network statistics generated by the network and potentially add repeaters for sparsely connected regions.

2.3 Results

This section details three classes of results. Section 2.3.1 starts by detailing the deployments using the technology described in Section 4.2. Section 2.3.2 then details the hydrological information provided from the sensor measurements taken. Section 2.3.3 presents the networking results, i.e., it analyzes the performance of the low-power wireless mesh network.

2.3.1 Deployments

The technology described in Section 4.2 has been deployed in three DWR-maintained independent sites across the Feather River basin in California, USA. The sites are Bucks Lake (BKL), Grizzly Ridge (GRZ) and Kettle Rock (KTL). Table 2.2 gives the position of the deployments, as well as the geographical size and number of devices. Tables 2.3a, 2.3b and 2.3c summarize the topographical features of the sensor station locations in each deployment. The number in the "Sensor station" column is the same as the one in Fig. 2.7. "Slope" indicates the slope of the ground at the sensor station location. "Aspect" indicates the orientation of the slope relative to North. "Vegetation" indicates the percentage of vegetation at the sensor station location. This feature was estimated basing on the NLCD canopy dataset[10]. The original cell size of 30 m was downscaled to 10 m using bilinear interpolation for the scope of this work. Fig. 2.7 shows a bird's eye view of the deployments.

[10] `https://www.mrlc.gov/`

Table 2.3: Sensor station features.

(a) Bucks Lake

Sensor station	Elevation (m asl)	Slope (°)	Aspect (°)	Vegetation (%)
0	1752.18	4.87	237.70	69
1	1739.24	12.73	272.04	65
2	1769.00	0.45	158.07	52
3	1715.75	14.70	276.87	69
4	1768.86	2.15	109.49	66
5	1754.57	9.60	318.66	57
6	1702.77	17.03	221.94	84
7	1771.00	2.00	132.53	70
8	1753.43	4.45	89.80	24
9	1736.49	7.69	323.98	43
10	1700.23	14.04	338.58	77
11	1744.54	3.84	53.72	71
Mean (site)	1746.35	8.39	198.33	65
25° perc.	1737.28	4.35	92.49	60
75° perc.	1758.34	11.74	314.79	77

(b) Grizzly Ridge

Sensor station	Elevation (m asl)	Slope (°)	Aspect (°)	Vegetation (%)
1	2083.36	4.68	15.25	13
2	2063.50	11.09	53.60	70
3	2101.94	5.18	102.18	55
4	1997.44	15.23	57.83	63
5	2098.09	17.77	348.08	67
6	2109.13	10.49	327.77	55
7	2075.89	6.10	109.41	38
8	2081.81	3.24	73.01	19
9	2019.66	11.09	47.71	51
10	2115.61	7.15	324.20	51
11	2015.63	12.17	59.33	41
12	2070.13	16.44	39.50	73
Mean (site)	2089.93	9.30	131.73	48
25° perc.	2075.19	5.35	39.76	34
75° perc.	2113.57	12.05	228.65	64

(c) Kettle Rock

Sensor station	Elevation (m asl)	Slope (°)	Aspect (°)	Vegetation (%)
1	2228.09	17.96	196.39	45
2	2239.26	7.80	231.00	40
3	2276.69	12.30	153.34	45
4	2171.84	14.96	179.93	88
5	2198.68	13.51	54.50	35
6	2166.72	14.18	154.13	58
7	2210.55	8.20	179.41	0
8	2234.77	14.89	98.82	2
9	2217.44	11.40	213.00	50
10	2157.93	8.99	156.45	61
11	2131.82	15.29	179.94	63
12	2234.41	11.67	13.83	32
Mean (site)	2213.69	10.64	159.40	42
25° perc.	2180.32	8.25	142.26	23
75° perc.	2246.90	12.95	174.52	61

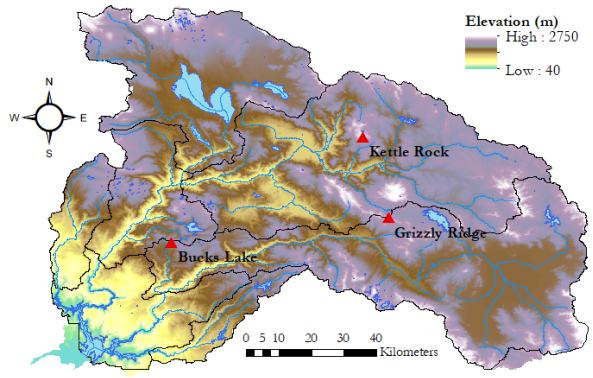

(a) Elevation map of the Feather River basin, with the deployment locations indicated

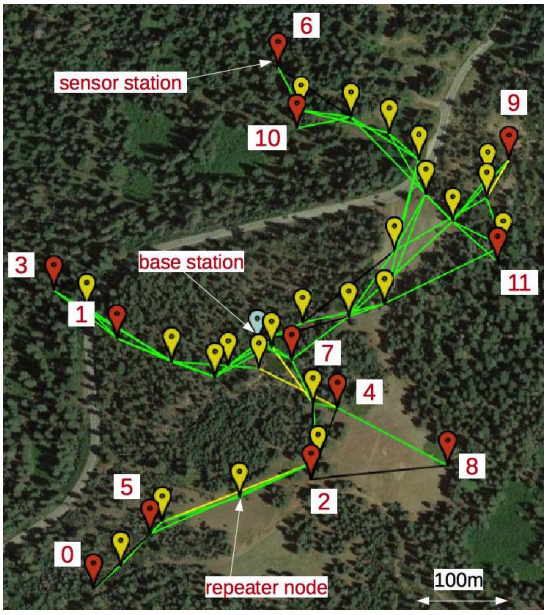

(b) Bucks Lake deployment

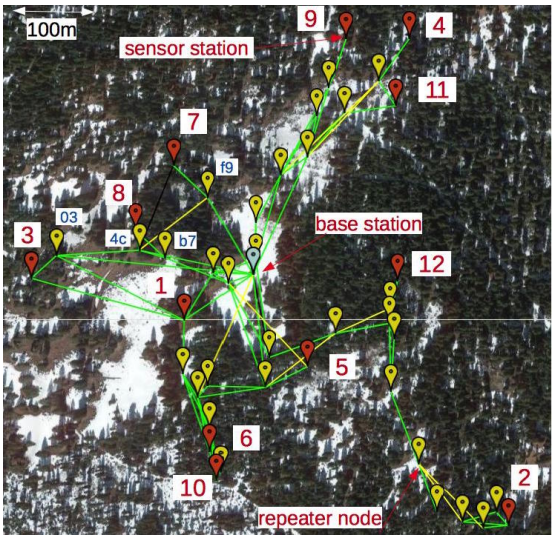

(c) Grizzly Ridge deployment

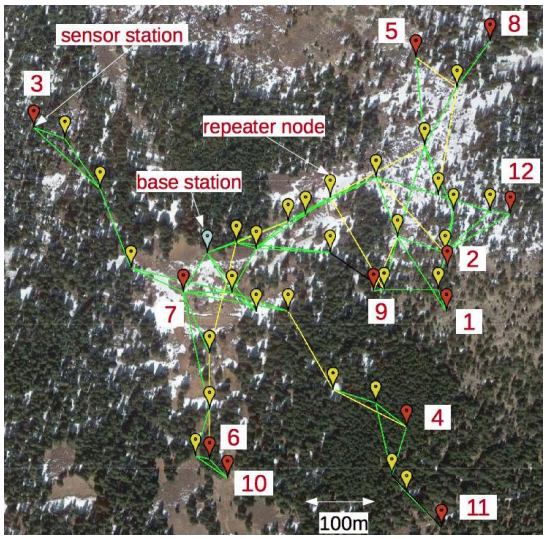

(d) Kettle Rock deployment

Figure 2.7: Maps of the deployments.

2.3.2 Examples of hydrologic data from WSNs

Fig. 2.8 shows an example of mid-winter sensor data from Grizzly Ridge beginning 15-Jan-2017 and ending 01-Mar-2017. Fig. 2.9 reports a second example from the same site, but in this case spans 01-May-2017 and 15-Jun-2017 (snowmelt season). These two temporal windows are used to exemplify the entire spectrum of hydrologic fluxes and states that were monitored during the 2016/17 water year using wireless sensor networks.

Accumulation period

The 2016/2017 snow season at Grizzly Ridge started in mid-November but only a shallow snowpack persisted until January 1st (around 30 cm, data not shown). Between January and March, frequent atmospheric rivers from the Pacific Ocean hit the California coast and caused a marked increase in snow accumulation across the entire Sierra Nevada, making this water year one of the wettest on record[11]. In the Feather River, January and February were the wettest in 110 years of recorded data[12]. Because of complex topographic transitions between rainfall and snowfall, some of these precipitation events exhibited both an increase in snow depth and massive snowmelt. An example is the rain-on-snow event between February 6th and 10th, when about 325 mm of precipitation fell over the basin (source: DWR), with dramatic consequences for the State's water system and local population due to simultaneous damage of the Oroville dam spillway at the downstream outlet of the Feather River.

Figure 2.8 focuses on three of these large precipitation events, which showed consistent patterns between nodes in terms of increasing snow depth (Fig. 2.8a), saturated air (Fig. 2.8c), and decreased solar radiation (Fig. 2.8d). This similarity between nodes is due to the fact that precipitation events occur at a much larger scale than that of single sensor stations. Simultaneous measurements of snow depth and air temperature at nodes allow us to tentatively classify these events as either snowfall (18-Jan-2017 to 22-Jan-2017, and 19-Feb-2017 to 20-Feb-2017, average air temperature around -5.8 / -0.6 °C and -4.3 / -0.1 °C, respectively) or mixed rain and snow (03-Feb-2017 to 09-Feb-2017, average air temperature around -2.2 / +4.4 °C). Blending sensor information and co-located rain gauge data[13] shows occurrence of rainfall after 08-Feb-2017, when snow depth at nodes started to decrease but the rain gauge recorded an increase. This pattern is again consistent with sensor data on relative humidity, radiation, and temperature (average air temperature around 0 / +3 °C). Relative humidity and temperature data show little variability between nodes during precipitation events and larger spatial heterogeneity during periods with no precipitation (e.g., 12-Feb-2017 to 15-Feb-2017, consistent with data of radiation and of the co-located rain gauge). These three precipitation events were separated either by periods of possible snowmelt (30-Jan-2017 to 31-Jan-2017, decreasing snow depth and temperatures above 0°C) or settling

[11] http://cw3e.ucsd.edu/how-many-atmospheric-rivers-have-hit-the-u-s-west-coast-during-the-remarkably-wet-water-year-2017/

[12] Source: California Department of Water Resources – DWR

[13] `https://cdec.water.ca.gov/`

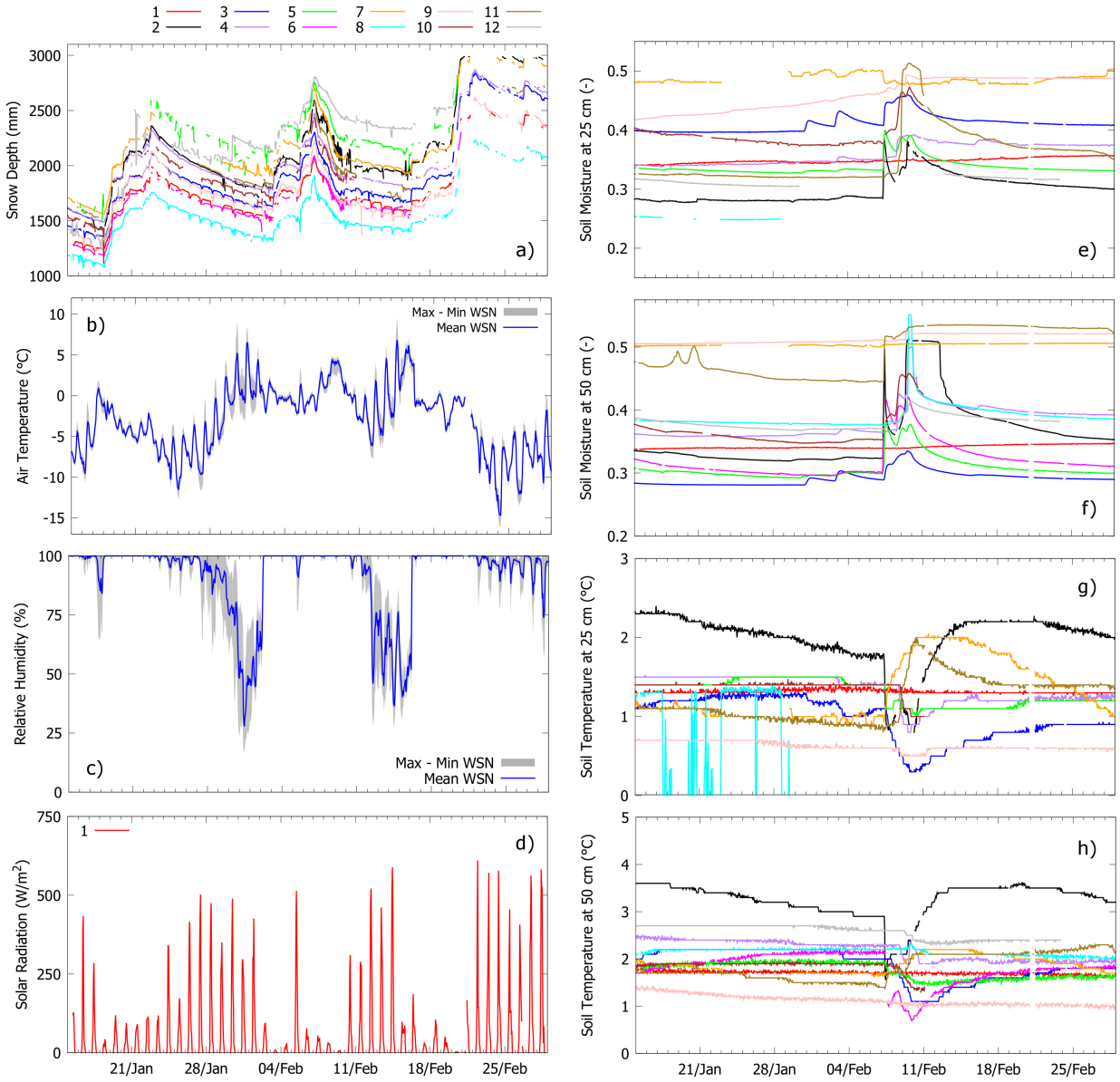

Figure 2.8: Examples of mid-winter sensor data from Grizzly Ridge (15-Jan-2017 to 01-Mar-2017). Line colors for panels (e) to (h) are the same as panel (a). Because measurements of air temperature and relative humidity show relatively small variability within nodes, panels (b) and (c) only report maximum - minimum range and mean. Solar radiation is only measured at node 1 (pillow).

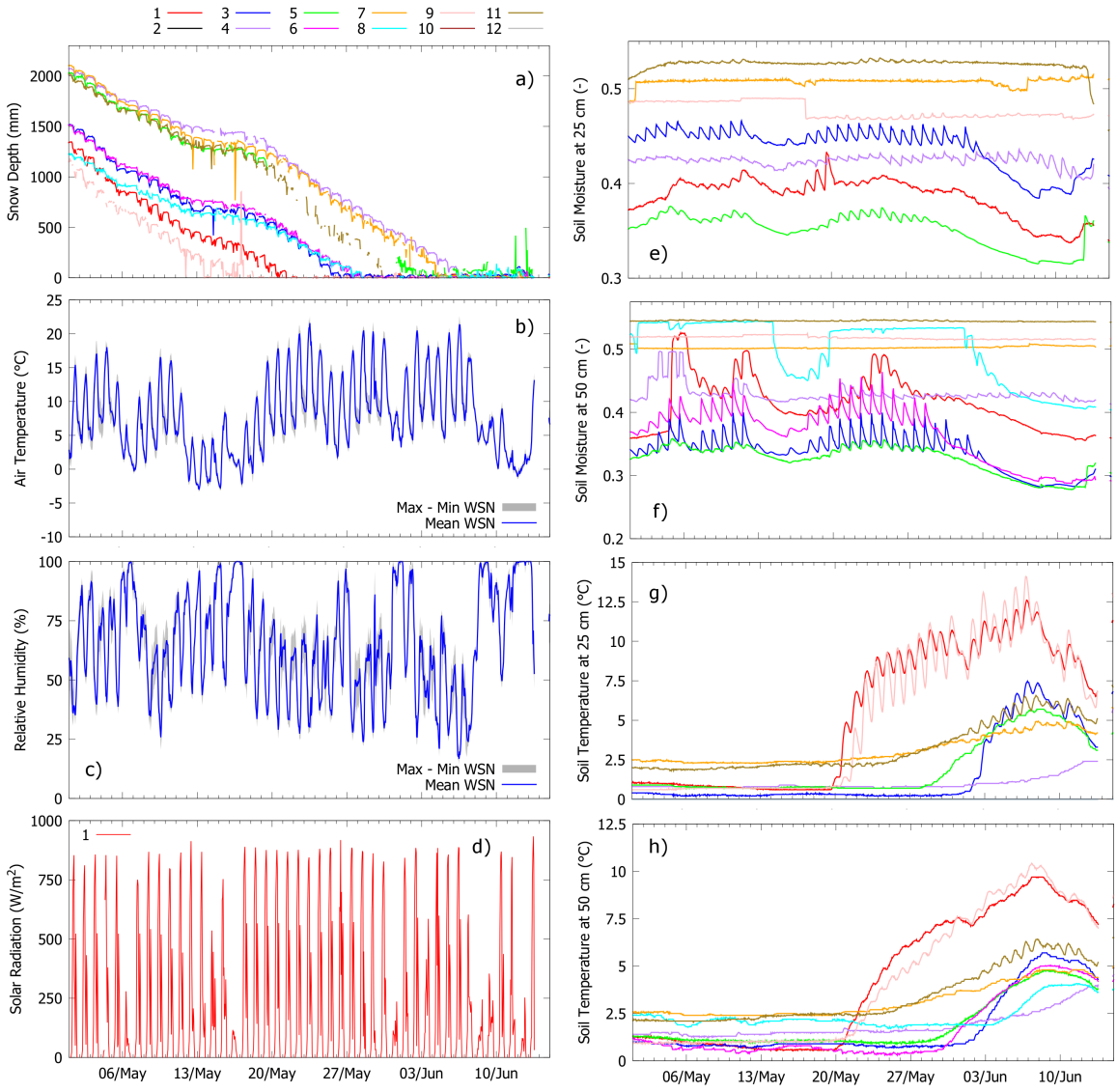

Figure 2.9: Examples of spring sensor data from Grizzly Ridge (01-May-2017 to 15-Jun-2017). Line colors for panels (e) to (h) are the same as panel (a). Because measurements of air temperature and relative humidity show relatively small variability within nodes, panels (b) and (c) only report maximum - minimum range and mean. Solar radiation is only measured at node 1 (pillow). Soil moisture and temperature sensors at 25cm depth malfunctioned at both nodes 6 and 8 during the reported periods. These data are therefore missing.

(25-Jan-2017 to 28-Jan-2017, again decreasing snow depth but temperatures below 0°C), with clearly different implications for runoff forecasting in snow-dominated contexts.

Simultaneous soil moisture data (Fig. 2.8e-f) show no significant infiltration during the two snowfall events but strikingly different patterns of soil moisture between nodes during the February rain-on-snow event. These increases and decreases in soil moisture may be related to differences in moisture conditions across nodes and in precipitation phase at local scale While nodes recorded stable winter soil temperature at seasonal scale ($\sim$ 1 - 3 °C), some of them showed either decreasing/increasing soil temperature from 07-Feb-2017 to 10-Feb-2017, which again could be related to local-scale energy processes during rain-on-snow events like snow pack phase change, soil thawing, or rainfall temperature.

Snowmelt period

The 2017 snowmelt season in Grizzly Ridge started in March. Depending on the location, canopy coverage, and peak snow depth of nodes, the end-of-season date ranged between 13-May-2017 (Node 9) and 06-Jun-2017 (Node 4). Figure 2.9 focuses on this key period of the water year when snowmelt runoff represents an important input to the surface and sub-surface hydrologic system of Californian Alpine watersheds.

All nodes showed a constantly decreasing snow depth during the period considered (Fig. 2.9a). This decreasing trend due to snowmelt is consistent with simultaneous daily cycles in solar radiation (Fig. 2.9d), relative humidity (Fig. 2.9c), and temperature (Fig. 2.9b), which are all proxies of stable atmospheric conditions and absence of precipitation (confirmed by the co-located rain gauge). The only period of constant snow depth was recorded between 14-May-2017 and 17-May-2017 and was marked by simultaneous negative air temperature, saturated air, and decreased solar radiation. While these conditions might be indicative of precipitation, a cross-check with snow depth data (constant) and co-located soil moisture data (decreasing at most nodes) can exclude significant precipitation events during this temporal window (again in agreement with the co-located rain gauge).

In terms of soil temperature, the end-of-season date was marked by diurnal temperature cycles that were not observed during periods of snow on the ground (Fig. 2.9g-h, Lundquist and Lott (2008)). Shallower temperature probes (Fig. 2.9g) showed more pronounced cycles than deeper sensors (Fig. 2.9h), which is consistent with expected temperature profiles with depth. Soil moisture showed clear differences in daily temporal patterns between nodes (Fig. 2.9e-f): while some nodes present recharge-discharge dynamics due to snowmelt infiltration into the ground, others show constant saturation, which may have impeded infiltration in favor of surface runoff. After snow disappeared, soil moisture decreased at most nodes due to the absence of inputs from the ground surface and concurrent evapotranspiration. The observed increase in superficial soil moisture at some nodes around 12-Jun-2017 to 15-Jun-2017 may be related to light rainfall and possibly snowfall on 12-Jun-2017 (minimum daily temperature around -1 °C). This conclusion agrees with simultaneous relative humidity (Fig. 2.9c) and radiation (Fig. 2.9d) readings. Also, some nodes measured a slight increase in snow depth, although on a scale comparable to background noise (see Fig. 2.9a). The rain

gauge did not measure any increase in precipitation, even though light rainfall/snowfall may be missed due to precision and under-catch.

Comparison with pre-existing survey techniques: snow courses

Figure 2.10 compares the range of variability of WSN snow depth measurements with manual measurements taken by monthly snow courses at the same locations (no snow courses are done at the Bucks Lake site). Snow courses are performed by manually measuring snow depth along transects and then averaging measurements to provide a representative value for the site. Daily snow depth at each node was estimated by calculating the median of all available readings on each day. Median values were preferred to means to reduce the impact of noise. Minimum, mean, and maximum snow depth across all nodes at a site were then calculated from these median values. These three statistics were calculated when at least eight different node values are available, which explains gaps in the time series. In addition, for the purposes of comparison, we highlight the depth recorded by the sensor node placed at the snow pillow. This node represents the same location as the pre-existing, standard snow and meteorological station. While this station also measures SWE, this variable is not directly measured by our wireless sensor networks.

The datasets show similar temporal patterns: accumulation occurs from December to February; peak accumulation in March; and snowmelt from April to May. Snow courses, however, tend to overestimate the mean site snow depth and may even exceed the maximum measurement from sensor nodes. The coarse temporal resolution of the snow courses makes it difficult to capture important hydrologic statistics such as date of peak snow or snow meltout date. The WSN data reveals that spatial variability increases over time in response to different solar radiation inputs across the nodes, mainly due to different aspects and vegetation coverage. This considerable variation cannot be captured by a single index station. Maximum differences in snow depth are on the order of 1.5 - 2 m, resulting in significantly different end-of-season dates from node to node: the difference between the first and last meltout date recorded by sensor nodes is 19 days in GRZ, 39 days (KTL), and 25 days (BKS). Since snowmelt is the primary driver of streamflow during the ablation period, this timing may significantly impact runoff forecasting. Snowfalls, on the other hand, reduce spatial variability since snow events are dictated by weather conditions at larger scales than that of WSNs. Several snow depth sensors saturated during last season, which means that the distance between the sensor and the surface of snow was too short for the sensor to make measurements. This was also treated as a node gap for the purposes of comparison.

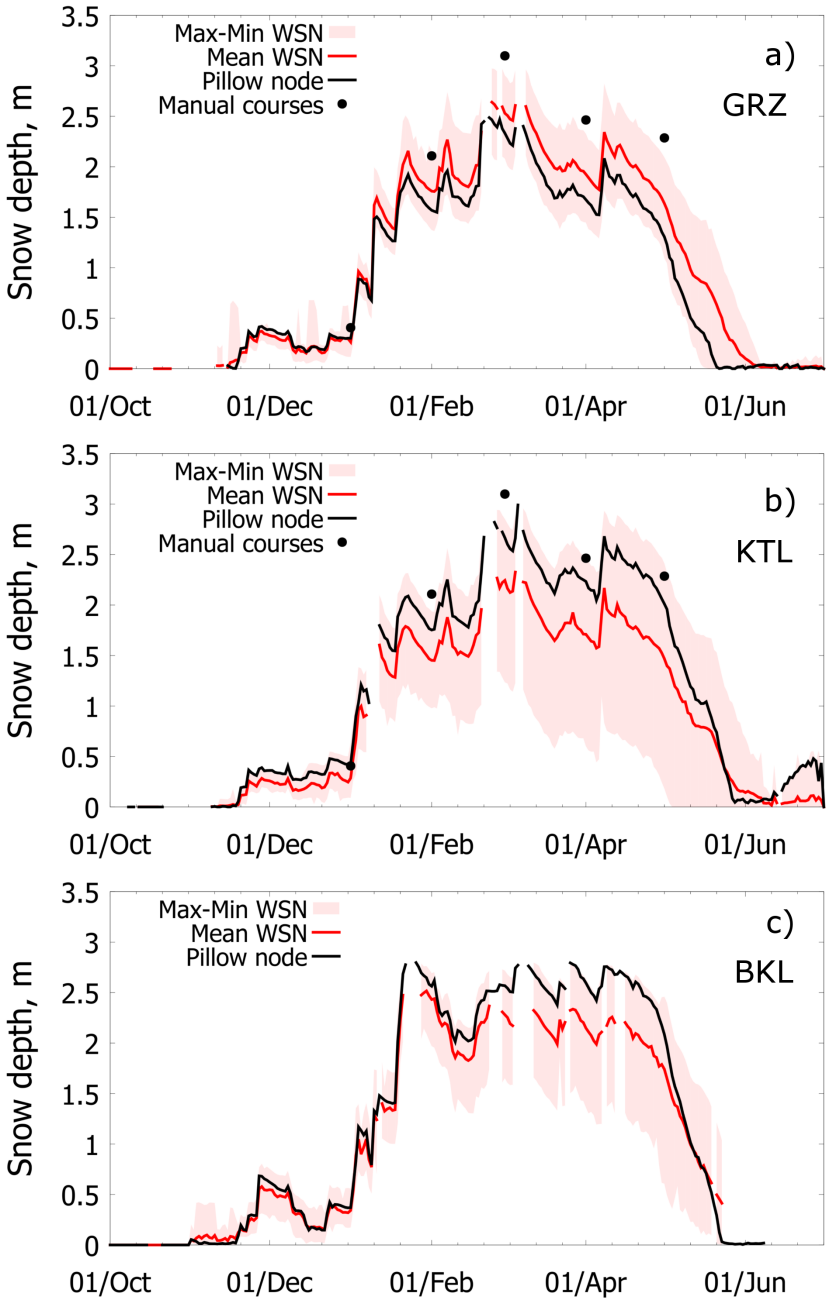

Figure 2.10: Comparison between snow depth measurements from the WSNs with manual measurements taken by monthly snow courses at the same locations (no snow courses are done at the Bucks Lake site).

2.3.3 Network performance

Estimated performance

We use the Dust Networks SmartMesh Power and Performance Estimator[14] (Watteyne, Weiss, et al. 2015) to calculate the performance of the network. Table 2.4a provides a full list of the input parameters. We use Fig. 2.6a to count the number of devices at each hop. All other input parameters correspond exactly to the application deployed. Table 2.4b lists the key estimated performance indicators.

The **average current** consumption of a device depends on its position in the network: the closer to the base station (the lower its "hop" value), the more stations it has to relay for, and the more current it consumes. All SmartMesh IP modules consume **<50 μA**. For repeater nodes that joined the network, that is the maximum current consumed (there are no other components). Since a repeater node is powered by a 17 Ah battery, this translates to tens of years of battery lifetime[15]. A sensor station is equipped with many more electronics, including the PSOC and the sensors. The current draw of the SmartMesh IP module becomes negligible. The sensor station is powered by a 17 Ah battery pack, recharged by a 15 W solar panel, which is enough to perpetually power all electronics.

Table 2.4b also indicates that the average latency (the time it takes for a sensor measurement to travel from the sensor station to the base station) is **<6 s** max. It takes **<30 min** for the entire network to build at installation. The network only builds once during the entire lifetime of the deployment; during that period, a device is "searching" for the network, consuming 500 μA on average.

Measured performance

Every 15 minutes each mote generates a network statistic message that contains information about the mote itself and the neighbors it uses to communicate. Results in this section are extracted from over 7 million network statistics gathered from the 3 deployment sites.

When a mote transmits a packet, it waits for an acknowledge (ACK) to confirm that the receiver mote received the packet correctly. If the transmitting mote does not receive an ACK, it retransmits its packet. Because the motes are using channel hopping, retransmissions occur on a different channel than the first transmission, increasing the probability of reception (Watteyne, Mehta, and K. Pister 2009). The *Packet Delivery Ratio* (PDR) is the number of successful transmissions (i.e. transmissions that received an ACK) divided by the total number of transmissions. The PDR gives an idea of the "quality" of a wireless link.

Table 2.5 presents the measured PDR of the three sites over the following periods: i) Bucks Lake from 23-Sep-2016 to 07-Dec-2016 (2.5 months - 363k measurements) ii) Griz-

[14] `http://www.linear.com/docs/42452`

[15] A device consuming 49.7 μA should live for 39 years when powered by a 17 Ah battery. That being said, the shelf life of the Tadiran TLH-5930 D-cell battery is 20 years. The effective maximum lifetime is hence 20 years.

Table 2.4: Estimated performance

Hop	Number of devices
1	5
2	8
3	9
4	9
5	2
6	1

Input parameter	Value
Requested service	900 s
Reporting interval	900 s
Payload size	50 B
Hardware type	5800 8dBm
Supply voltage	3.6 V
Downstream frame size	1024
Join duty cycle	10%

(a) Input

Hop	Average current	Mean latency
1	49.7 μA	0.95 s
2	38.7 μA	1.87 s
3	37.3 μA	2.79 s
4	29.5 μA	3.70 s
5	32.2 μA	4.62 s
6	27.2 μA	5.54 s

Estimated performance indicator	value
Manager ave. current	218 μA
Network build time	24.1 min
Mote search current	500 μA

(b) Output

Table 2.5: Measured average PDR over the three deployment sites.

	Bucks Lake	Grizzly Ridge	Kettle Rock
Average PDR	89%	79%	82%
PDR stand. dev.	16%	22%	20%
(Transmit/Fails)	(15,654K/1,757K)	(64,027K/13,297K)	(15,654K/1,757K)

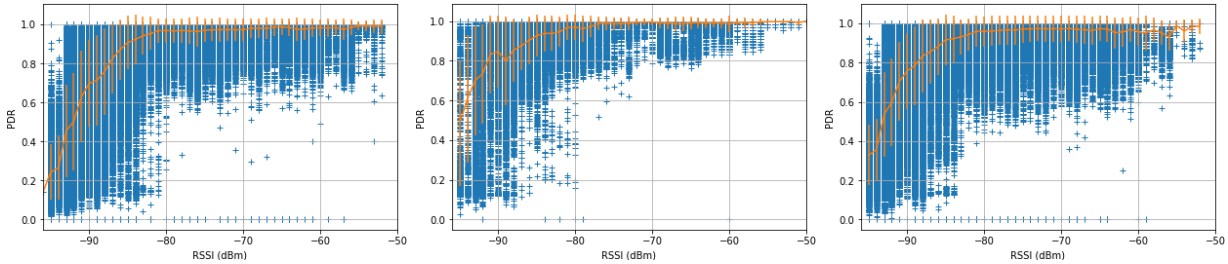

(a) Grizzly Ridge (b) Bucks Lake (c) Kettle Rock

Figure 2.11: The PDR/RSSI "waterfall" plot.

zly Ridge from 24-Sep-2016 to 21-Mar-2017 (6 months - 1,209k measurements) iii) Kettle Rock from 09-Oct-2016 to 21-Mar-2017 (5.5 months - 1,094k measurements)

To better understand the level of external interference, Fig. 2.11 presents the relation between the RSSI and the PDR and shows the average and and standard deviation of the data in yellow. Those "waterfall plots" show that the average PDR of the links is very good (>95%) for transmissions above -80 dBm for every site. Below -80 dBm, the PDR decreases, indicating that frequent retransmissions is occurring on those links. They also indicate that the three sites do not suffer from external interferences, otherwise, the steep decrease plotted would be shifted to the right.

In SmartMesh networks, the deployment recommendation is that every node has to have at least 3 neighbors. To do so, each mote keeps track of the PDR of links to its neighbors, and periodically sends that information as regular data packets. This mechanism allows the software running on the base station to have a complete view of the connectivity in the network.

Every time a wireless link is created or deleted between neighbor nodes, these motes generate a path_create and path_delete event. We monitor those events to quantify the stability of the topology, or "churn", which consumes energy. Fig. 2.12 shows the number of path_create and path_delete events per day, over a month, for the Grizzly Ridge and Bucks Lake sites. The Kettle Rock site is not reported here as neighbors path_create and path_delete events were not collected at this site. The total number of links in the network is also depicted, as a reference.

At Bucks Lake, the churn alternates between periods with less than 10 events per day, and periods with almost 200 events per day. During the period with 10 events per day, once links are established, they remain useful for days/weeks at a time, resulting in a very stable

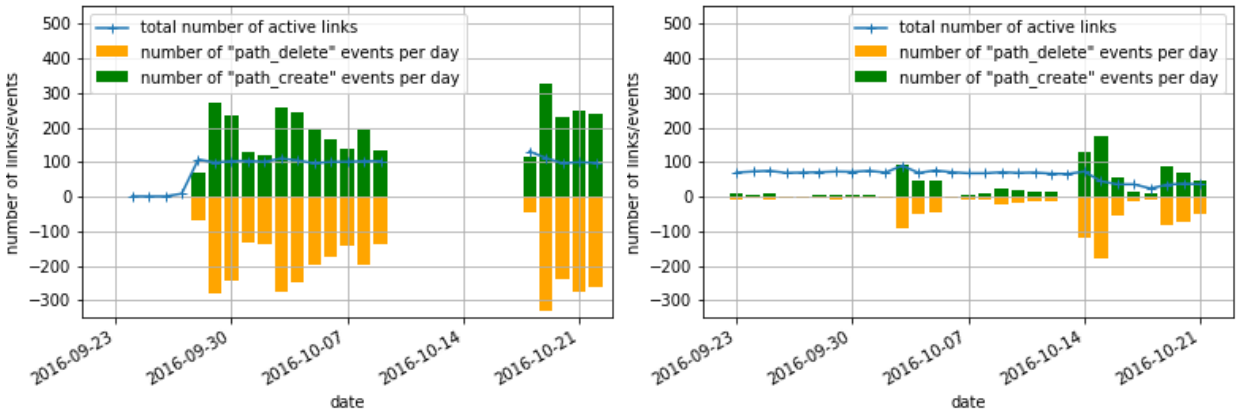

(a) Grizzly Ridge (b) Bucks Lake

Figure 2.12: Network stability: the number of path_create and path_delete events generated per day over a month. The top line shows the total number of active links, as a reference.

topology. We attribute the high churn present in Grizzly Ridge to the lack of links with good quality (i.e PDR>70). As every mote tries to ensure it has at least two parents, it associates with neighbors even with a low quality link if no parent with high quality is present. Selecting low quality links highly increases the number of path_create and path_delete events. Installation of a couple more repeaters would solve this problem.

At Grizzly Ridge, 8 motes out of 45 (5.6%) generate 69% of the path events. Table 2.6 lists the motes with which sensor node 7 (i.e., the mote that generate the most events) communicated as well as the quality of the link with each of those motes and the number of network statistics gathered for each link (i.e. health reports). We can see that only two links have a PDR >30% and that one of these links was reported only twice, meaning that it was not available for the rest of the time. This means that most of the time, the sensor node 7 was looking for a second parent to associate with and had to select links with low quality. To solve that issue, the solution is to add one repeater mote to increase the density and thus, reduce the number of path events.

2.4 Discussion

WSNs provide dense spatio-temporal hydrologic data at physiographically representative locations. These data can support better real-time monitoring of hydrologic fluxes across the landscape (see Section 2.3.2). As demonstrated by David E. Rheinheimer et al. (2016), better hydrologic information can potentially increase hydropower revenue. To that end, this deployment of WSNs demonstrates the capability of collecting more comprehensive hydrologic data, which can potentially translate into lower uncertainty in streamflow forecasts at various temporal and spatial scales and improved economic viability of hydropower.

The design, deployment, and maintenance of wireless sensor networks require more effort

Table 2.6: List of neighbors of sensor node 7 at Grizzly Ridge, with link quality and number of associated health reports. The mote does not constantly have two neighbors with high PDR that it can use as parents. It thus has to associate with neighbors with low link quality. Bold nodes are annotated in Fig. 2.7c

Destination node	PDR	#HR
Repeater node d3	14%	349
Repeater node 03	11%	72
Repeater node b7	9%	4
Repeater node f9	97%	1422
Repeater node ad	100%	2
Repeater node 4c	14%	73
Repeater node ac	9%	22
Sensor node 8	25%	1297

and a higher budget compared to a standard weather station. The installation in high-mountain environments also poses challenges due to harsh, remote conditions; damage from wildlife; and potentially extreme weather conditions, as occurred during the 2017 water year. This section provides a broader context about existing snow hydrologic surveys to show the value of WSN hydrologic information and elaborates on strengths and challenges of this system during the extreme conditions of the past water year.

2.4.1 Value of the hydrologic product

WSNs provide several important advantages when compared with traditional index stations. Standard instrumentation often includes a snow pillow, rain gauge, temperature sensor, and possibly wind speed and radiation sensors. These instruments, especially snow pillows, are typically located in areas that are flat and free of vegetation, making them inherently biased estimates of snow distribution in alpine regions (Zhang, Steven D. Glaser, Roger C. Bales, Martha, Robert, et al. 2017). Snow pillows also prevent infiltration into the ground from the snow they are measuring and insulate snow from thermal exchanges with soil, further biasing data such as end-of-season date. The end-of-season date signals a shift from snowmelt-dominated runoff towards other processes like groundwater discharge and evapotranspiration, making it an important metric for hydropower forecasters.

WSNs can also compensate for some well-known problems with traditional sensors. For example, rain gauges provide information on precipitation amount, but not phase (rain or snow). They are also prone to under-catch during intense snowfall/rainfall events. Blending data from surface and subsurface sensors WSNs and co-located standard instrumentation allows us to detect precipitation timing and phase, which can be critical in determining the timing of subsequent streamflow peaks. Another example is infiltration: most existing networks do not routinely measure soil moisture, whereas our WSNs do. Since overland flow

is a much faster process of streamflow generation than infiltration, soil moisture information can support short-term runoff forecasting at downstream reservoirs and powerhouses.

Finally, compared to traditional sites, WSNs can monitor how areas characterized by different canopy or aspect respond to precipitation, potentially allowing data collected under specific conditions to be generalized to uninstrumented areas with similar situations (see Section 2.4.5). Due to the complex interaction between snow melt and topography in mountain watersheds, data collected by traditional instruments are nearly impossible to distribute. WSNs, on the other hand, can tease out effects of canopy interception or geology on snowfall and snowmelt rate and infiltration patterns.

More specifically, snow depth and snow water equivalent are manually measured monthly using poles and vertical samplers, respectively (Sturm 2015). Compared to WSN systems, manual surveys are more time consuming, sometimes risky in avalanche-prone areas, and only provide snapshots of snow accumulation patterns at specific sites at monthly or seasonal scales. They are often performed only in areas accessible during winter, such as flat, open areas where a helicopter can land.

Autonomous sensors have also been deployed on entire mountain ranges for both water resources monitoring and avalanche forecasting [16]. Because of their often remote and distributed locations, data transmission within most of these networks is wireless, which make them technologically similar to WSNs. Compared to the latter however, such systems lack spatial representativeness of their region because they are deployed as one index station per site (Roger C. Bales et al. 2006). Recent results by Zhang, Steven D. Glaser, Roger C. Bales, Martha, and Daniel (2017) for example show that traditional stations are not representative of actual mean SWE at a $1km^2$ scale when compared to collocated WSNs. Moreover, traditional stations typically include only one of each type of sensor; should extreme alpine conditions damage the sensor midseason, the data are often lost. Finally, the footprint of autonomous sensors like snow pillows is significantly larger than that of single nodes. We estimate a minimum footprint for pillows in $\sim 10 \times 10$ m including rain gauge and equipment shelter [17].

At a smaller scale, several examples exist of highly equipped snow stations whose extension match that of WSNs (Leppänen et al. 2016; Reba et al. 2011; Krajči et al. 2017; Wever et al. 2015; Morin et al. 2012). In a broader context, such observatories have for a long time represented the main source of data for experimental hydrology bloschl16hydrological. A commonly employed method for data transmission in intensive study plots consists of wiring peripheral sensors to a central manager or laboratory. These sensors can be more vulnerable in alpine conditions, as they do not feature the self-healing characteristics of WSNs. Experience from field deployments indicates, for example, that wires are frequently damaged

[16] https://www.wcc.nrcs.usda.gov/snow/, http://bcrfc.env.gov.bc.ca/data/asp/, http://www.jma.go.jp/jma/indexe.html, http://www.slf.ch/schneeinfo/messwerte/stationsdaten/index_EN, http://www.meteomont.gov.it/infoMeteo/mappaStazioniAutomatiche.do, https://www.nve.no/hydrology/, http://www.meteo.fr/temps/france/nivose/france_niv.html

[17] https://www.wcc.nrcs.usda.gov/about/mon_automate.html

by wildlife. In addition, wired systems are more invasive than wireless counterparts, which makes WSNs a preferred solution in remote locations.

Remote sensing represents the most recent innovation in snow surveys (Sturm 2015; Parajka and Blöschl 2006; Margulis et al. 2016; Dietz et al. 2012; Prokop et al. 2008; Revuelto et al. 2016; Painter et al. 2016; Bühler et al. 2016; De Michele et al. 2016; Harder et al. 2016). The spatial extent of remote sensing products is generally larger than WSNs, and sensors with different wavelengths allow them to capture a broad range of snow properties like albedo and snow wetness. On the other hand, the temporal resolution of available surveys is usually limited and hampered by cloud obstruction (Dietz et al. 2012), whereas other techniques like laser scanning may be expensive and time consuming. Moreover they often require ground truthing from in-situ sensors or manual snow surveys. Some datasets, like MODIS, only provide direct information about snow covered area and are available at daily timesteps but at relatively coarse spatial scales (500 m), whereas other platforms only provide bi-weekly snapshots (see the US Landsat mission) or are still in an experimental phase (see for example the EU SENTINEL mission). Remote sensing is a promising complementary tool to WSNs, as it may provide information on broader spatial patterns that WSNs lack. WSNs provide the finer temporal resolution necessary for short-term streamflow forecasting. In California, for example, the Airborne Snow Observatory is now providing maps of snow depth at an unprecedented spatial resolution (Painter et al. 2016), even though the spatial and temporal extent of these scans is still limited by budgetary constraints. Synergy between these techniques can potentially provide the necessary data needed by water resources managers in real time.

2.4.2 Design choices: comparison with other wireless solutions

Numerous wireless solutions – both academic and off-the-shelf commercial – are available which may be considered for our application. Below, we offer a brief comparison and justification for selecting the w system.

Low-power wide-area network (LPWAN) technology has received attention in the last year, with two competing approaches, Sigfox and LoRA. They are similar in that compliant radios send small frames to one or more base stations up to 15 km away. The range makes it a very appealing technology, and remote environmental monitoring could be an ideal target application. However, we have identified several potential drawbacks which rule out LPWAN for our purposes.

First, the amount of data LPWAN technology can carry is too little. A Sigfox node, for example, can send only 140 frames per day, each carrying only 8 B of payload. This is roughly an order of magnitude below what our sensor stations produce. Second, though both Sigfox and LoRA offer some downstream capability (the ability to send commands to the device), it is not comprehensive enough for our use. Only a handful of frames per day can be sent; this is several orders of magnitude too little and prevents the user from being able update firmware remotely. Over-the-air reprogramming, especially of the firmware, is a crucial requirement, as our deployments are inaccessible during the entire winter. Third, LPWAN technologies

are best-effort; that is, when a device sends a frame, it has no way of knowing whether a base station received it. For example, early field trials of LoRA show end-to-end reliability as low as 90%, even with thirteen base stations[18]. For our application, it is critical to lose as little data as possible, as real-time forecasting of the yield of hydroelectric power plants are based on the data collected. Finally, proven technology that offers wire-like reliability already exists, which can be seamlessly integrated with a single cheap cellular uplink connection. These more viable options, coupled with the fact that no LPWAN technologies have been deployed in the Feather River basin, make LPWAN technology a less than ideal option.

In terms of the base station's connection to the Internet in remote regions, a few options exist depending on availability. Cellular connection is the most attractive in terms of data rate and pricing. Cellular coverage can be limited in remote areas, but directional antennas can improve connections. Otherwise satellite linkage must be used. This is not preferred as, compared to cellular, satellite costs far more to transmit and is finicky to maintain.

Rationale for using SmartMesh IP

The analysis above has lead us to opt for SmartMesh IP, coupled with a single cellular connection at the base station. The result is a complete end-to-end solution with key benefits, which we list below.

Low complexity and cost. The low-power wireless network connects all sensor stations to the base station locally at the deployment site. This means that only the base station (not the sensor stations) needs to connect to the Internet, improving reliability and resiliency of the system.

Multi-km^2 deployment area. Given its multi-hop nature, a sensor station can be arbitrarily far from the base station. A deployment can span several km^2.

Ultra low-power operation. The SmartMesh IP modules consume <50 μA on average, allowing over a decade of battery lifetime.

Wire-like reliability. SmartMesh IP was designed for critical industrial applications, and offers over 99.999% end-to-end reliability.

Fully bi-directional communication. At any point in time, a network administrator or monitoring program can send commands to any of the devices in the network. This ability permits, for example, tuning parameters midseason.

Over-the-air reprogramming. As a corollary to having bi-directional communication, all SmartMesh IP modules can be securely reprogrammed over-the-air.

Built-in diagnostics. Each SmartMesh IP device regularly generates diagnostic data allowing a network administrator to have full visibility over the health of the network.

Proven and truly off-the-shelf. Over 60,000 SmartMesh networks have been deployed so far. One vendor alone, Emerson, claims over 31,900 networks, with cumulated node oper-

[18][in French] http://www.orange-business.com/fr/blogs/usages-dentreprise/machine-to-machine/qualite-de-service-d-un-reseau-iot-base-sur-lorawantm-enseignements-et-elements-mis-en-oeuvre

ating hours above 9 billion[19]. While SmartMesh IP was designed for industrial applications, it has been used in numerous other spaces, including smart buildings[20], smart cities[21] and smart agriculture (Watteyne, Diedrichs, et al. 2016). SmartMesh IP is a proven technology; we chose to use it because our system operates well within the limits of a SmartMesh IP network. For example, SmartMesh IP network as a whole cannot generate more than 36 packets per second, with each packet carrying at most 90 bytes of application payload. In our case, each sensor station generates a 20-byte data packet every 15 min, well within the limit. The typical latency from a sensor station to the base station is on the order of 1-2 seconds. Given the relatively slow-moving nature of the data that we are measuring, this delay is acceptable.

2.4.3 Comparison with existing WSN systems for snow monitoring

Multiple research projects, described below, aim to use WSNs to monitor snow properties. A 57-node WSN was successfully deployed across a forested, 1-km^2 headwater catchment in the southern Sierra Nevada of California using SmartMesh IP technology as the system backbone but with different sensors, hardware and software design (Kerkez et al. 2012). The software and hardware used did not allow for data recovery. It was determined that a 50-m node-to-node spacing would conservatively lead to a good PDR. More importantly, Kerkez et al. (2012) highlight the importance of network reconfiguration during the actual deployment using information of RSSI and PDR collected by the network to avoid network collapse. A histogram of PDR values showed that after readjustment, about 80% of all network paths are performed within the desired 8590% design value, and over 50% of all paths are at 100% PDR (Kerkez et al. 2012). On the other hand, we deployed repeaters at distances greater than 50 m whenever line-of-sight between them was available. Thanks to the newly developed SOL, we were able to visualize in real-time the quality of links in terms of RSSI and PDR, detect issues, and identify potential adjustments (see Fig. 2.7). Moreover, the base station in Kerkez et al. (2012) is installed at the network edge, which not only represents a regional point of failure, but also increases the operational burden and power consumption of repeaters close to the base station given that they must route all incoming network packets to the base station.

A similar system of 14 WSNs was deployed in the high elevations of the American River basin to measure the snowpack in real-time (Zhang, Steven D. Glaser, Roger C. Bales, Martha, and Daniel 2017). Each WSN consists of 10 sensor stations placed within a 1 km^2 area. Zhang, Steven D. Glaser, Roger C. Bales, Martha, and Daniel (2017) frame the system as capable of long-term operation with minimal maintenance and highlight the ease of installation. The system uses the same networking hardware as our deployments, which is

[19] http://www.emerson.com/en-us/expertise/automation/industrial-internet-things/pervasive-sensing-solutions/wireless-technology

[20] http://versasense.com/

[21] http://www.linear.com/docs/41387

capable of multi-level storage. However, it uses different sensors and has no data-recovery functionality. Moreover it uses different deployment strategies for base stations, sensor stations, and repeaters as the one described in Section 2.2.4, as well as a different software suite. The paper also calls for future work to develop tools to verify the performance of the network, interfaces to assist during network deployment, visualization of the network health information, real-time displays of sensor data, and logging of maintenance activity, all of which are implemented by the system presented in this paper.

Henderson et al. (2004) plan to build 50-100 WSNs to monitor and forecast avalanches in the Wasatch Mountains in Utah, by measuring different properties of the snow. Their mote will use a chipcom CC1000 RF transceiver by Texas instruments that will need interfacing and considerable low-level protocol design and programming to reach an efficient and usable wireless system adequate for alpine environments. The research work presented is still in its starting phase where only lab tests of sensors have been performed with no indications of field deployment.

SnowFort (Liao et al. 2014) presents a full WSN-based system for infrastructure and environmental monitoring with server-side data analytics. Although the main focus of their work is structural health monitoring, the framework described is meant to fit broader applications such as snow monitoring. The system's high-level conceptual design is similar to the one presented in this article. The main system components are the TelosB, used as mote, and a Raspberry-pi, used as a base station. TelosB is is 18 year old technology developed as a teaching tool at the University of California Berkeley. It is programmed via the older tinyOS, another teaching tool. The device uses an 8-bit MCU and is hindered by one megabyte of on-board storage memory. Unlike the system presented in this paper, SnowFort only supports single-hop star network topology, which presents a spatial coverage issue. SnowForts suggestion for increasing spatial coverage is to install multiple base stations. However, base stations can consume orders of magnitude more power than motes and even more when they transmit data to the Internet. Each base station would require a cell network connection. This represents a shortcoming for monitoring snow across spacious alpine regions.

Conceptually, the closest WSN-based system found in the literature is SnowCloud (Skalka and Frolik 2014), which uses the TelosB with different core mesh protocol and components. This system has been deployed at the Sagehen Creek, CA experimental field station (Moeser et al. 2011). Nodes communicate via a TinyOS network. The core component of each sensor station is a MEMSIC TelosB mote, with all the issues described above. Their sensor station consists of two parts: a surface node that is very similar to our sensor node, and a ground node that communicates wirelessly with the surface node through the snow. A critical difference between the two systems is power consumption at the sensor node: while the TelosB platform has a 20 to 30 mA consumption on average, a NeoMote consumes 2 mA on average. Authors rightly note that network time synchronization would certainly provide a more robust system and allow nodes to periodically operate in low-power mode. This is at the core of our system provided by the SmartMesh IP mesh protocol and for SnowCloud, this can be achieved by jettisoning the use of tinyOS and using openWSN (Watteyne, Vilajosana, et al. 2012). They are also currently developing the gateway capability of the manager and

remote time synchronization of the sensor station's real-time clock to combat clock drifts. Both of those features are present in our system.

2.4.4 Challenges and lessons learned

The key variable for choosing among the most appropriate technological solutions available on the market was the ability to hold up under the harsh alpine environment like of the California Sierra Nevada. In-lab and local field testing further the range of potential failures found in the field. Still, several problems ranging from minor to critical were encountered during the system operation. The following lessons learned would improve future deployments:

1. We experienced prolonged power failures at the Bucks Lake manager due to the misplacement of the manager node in a poorly irradiated location shaded by canopy. The manager cell modem was configured to shutdown at 11V to stop draining the battery, which was devoted to powering the WSN network manager. This allowed the WSN to keep operating locally, but without real-time publishing, a major issue for a real-time system. Both Kettle and Grizzly managers were better placed and did not exhibit such a problem, highlighting the need for considering canopy coverage during the design phase. Additional batteries were added to the Bucks Lake base station to prevent future outages. Relocating the solar panel could also be a solution, where/when feasible.

2. Some repeaters disconnected due to the original design of repeater layout. A choice was initially made to connect the repeater antennas through the top of the repeater box, sealing the mechanical connection with silicone caulk to prevent water seepage into the enclosure. Poor construction of the antennas prevented water from draining out of the bottom of the vented antenna. This disconnected some nodes from the network. Real-time link health maps 2.7 allowed for the timely discovery of the issue, and after drilling small holes in the clogged antennas, repeaters became functional again.

3. A firmware/hardware bug prevented some sensor nodes from sampling and sending data after a power recovery from a total battery discharge. The bug was attributed to the gradual voltage increase during recharge that mainly affected the real time clock component. The problem was subsequently fixed by adding a power-up voltage threshold and a delay to guarantee the different NeoMote components are operational before the main code starts. Only a few nodes exhibited this behavior, which was resolved by the code update.

4. We experienced extensive rodent damage to exposed antenna, sensor and solar power wires, especially at Bucks Lake. The cables close to the ground were all in metal conduit but the wires from the solar panel and temp/rH at the 5 m level were exposed. The 5 m of snow in 2017 allowed the pesky rodents to access these exposed wires System resiliency can be improved by appropriately shielding all wires from wildlife.

5. Solar panels, antennas, and snow depth sensors at several nodes were buried in snow for a few days during peak accumulation. This design issue was due to the abundant precipitation that occurred in the 2017 winter (we estimate about 4,000 mm of total precipitation at Bucks Lake, with peak SWE around 1400 mm). This season demonstrated that choosing the most suitable height *a priori* depends on consideration of extremes and could be difficult in a context of climate change-related extreme weather events. We recommend allowing for unanticipated extreme events during the design phase. In particular, efforts should be made to keep the base and sensor stations' antennas and the solar panel at the base station functional, as this is the most sensitive part of the network, Sensor stations can last several months on a full charge, so buried solar panels were of limited consequence. Also, redundancy of nodes at the same site makes the network resilient to localized failures compared to standard index stations.

The potential impacts of these problems was limited by the networks multi-level data replication feature, which means that data are stored at the sensor node, manager node, and server-side allowing for multi-layer data recovery. When disconnected sensor nodes rejoin the network, they automatically resend previously unsent data, safely stored on the internal SD card, allowing for a more timely recovery.

In view of the above problems, we can identify a few best practices for future deployments:

1. **Hierarchy of criticalities**: In such large-scale systems, it is important to identify and classify system elements based on their importance to the overall system operation. For instance, the base station power and connectivity to the Internet are far more critical than that of a sensor node, which in turn is more important than that of a repeater.

2. **Adequate testing**: In-lab testing for such systems is crucial. Moreover, testing in similar but easily accessible environments would also be an asset. Failures of temperature and humidity sensors that were then observed in the field first occurred in the UC Botanical Garden test network where weather conditions are closer to the mountains than lab settings.

2.4.5 Future R&D directions

This work opens up numerous research directions, both from a systems and a hydrologic perspective. While WSNs represent a well-established alternative to traditional sensing systems in many applications (see above), their use as a decision-support system for hydropower is relatively new and several improvements could be put in place to streamline their use in operational hydrology.

From a networking point of view, we are currently testing new server capabilities to provide advanced real-time network health analysis. This is key information from a decision support standpoint. We currently have the ability to visualize the quality of network links, giving administrators an intuitive interface to analyze network health. We are working to

generate notifications of certain events, such as a downed link or an extreme snow melt/accumulation. Such improvements are needed to make these systems more user-friendly and expand their use outside academic or experimental case studies. We are also working on improving the sensor stations' firmware to reduce the join duty cycle in the event that they lose connectivity to the network. Finally, work is being done to allow remote reprogramming of the PSOC on the sensor stations to increase flexibility and seriously reduce cost of field operations.

From a network planning point of view, we are working on tools to help a network installer with positioning repeater and sensor nodes in tandem. This tool builds on previous work on placing sensor stations (Oroza, Zheng, et al. 2016) based on propagation models in alpine environments (Oroza, Zhang, et al. 2017). The result will be a tool which, given environmental information about the deployment site, identifies the optimal repeater locations to ensure good connectivity within the network. Maintaining, moving, or replacing repeaters has represented an important part of our summer fieldwork after the first winter of operations. This emphasizes repeaters as a crucial component of a WSN that has received little attention in terms of deployment strategies compared to sensor stations. Replacing trial-and-error techniques for repeater placement with more automatic (and repeatable) techniques could increase the applicability of WSNs in real-world applications. However, this would require better pre-characterization of canopy properties, e.g., LIDAR, compared to available satellite-based images, which could increase the overall cost of deployment. More research is needed to determine whether it is worth pursuing. Future studies could also explore optimization methods for the overall system design to ensure long-term operation at minimal cost (explored in the context of WSNs monitoring oil pipelines by Xia, W. Liu, and Deng (2015)) and assessing overall system reliability (e.g. through a Markov-model of the system evolving in multiple environments (B. Liu et al. 2016)).

Finally, we intend to generate real-time SWE maps by blending our WSN data with remote sensed products such as MODIS and Landsat fractional snow cover. These spatial snowpack maps can then be assimilated into runoff models such as PRMS in an attempt to improve reservoir inflow forecasting. From a hydrologic perspective, this is the most important direction of future developments and the real testing ground for the value of WSNs. Snow patterns are highly variable in space and time and this heterogeneity has important feedbacks with various aspects of the biosphere, including vegetation distribution and streamflow timing during the dry season. While these results show potential for an improved monitoring of hydrologic fluxes at locations that are representative of relevant physiographic features, leveraging this information to provide real-time and spatially consistent information at catchment scale will expand the dataset and provide more useful tools for water resources managers. A specific challenge here is to conceive multi-cluster WSNs that can expand monitoring capabilities of single networks along large altitudinal, longitudinal, and latitudinal ranges that could better meet the typical scale of interest of hydrology.

Chapter 3

Wireless sensor networks for improved snow water equivalent estimation and runoff forecast

3.1 Introduction

Various civil systems can be improved by using Internet of Things (IoT) technologies to provide solutions in measurement and monitoring. IoT applications research spans from home automation and optimization (Baraka et al. 2013) to wider scale interests such as smart buildings, industrial monitoring, intelligent traffic systems and cities (Daponte et al. 2018). We present a study that leverages IoT in measuring hydrologic variables and monitoring snowpack, with the long-term goal of optimizing water management and electricity generation given accurate runoff forecasts.

Mountain snowpack plays an important role in water and energy budgets, especially in the state of California where seasonal snow cover is the primary source of water for the population, for one of the most productive agriculture sector in the world and for various other industries. More than half of the state's water originates from its snowpack. Runoff from snowmelt is stored in reservoirs and provides fresh water during the summer dry months as well as electricity. Therefore a more accurate and timely runoff forecast allows for improved flood control, improved resource management and potentially increased hydropower revenue, by continuously informing the decision making (David E. Rheinheimer et al. 2016). The state of California aims to increase procurement of eligible renewable energy resources to 33% by 2020 and 50% by 2030. Hydro electricity accounts for 10% to 30% of in-state electricity generation (Commission 2017) and is considered an essential support in the scheme of meeting those goals. Large hydro plants serving both water storage and electricity generation are crucial to compensate for the intermittent nature of renewable sources, while optimizing water management.

High-resolution real-time sampling and accurate estimation of the snowpack spatial dis-

tribution constitutes the initial conditions for runoff models that may translate into improved runoff forecast in mountainous regions (Jorg-Hess, Griessinger, and Zappa 2015). As Dozier, Bair, and R. E. Davis (2016) states, spatial snow water equivalent (SWE) estimation is "currently the most important unsolved problem in snow hydrology". Yet, current runoff forecasting in California is largely estimated using statistical regression between historical peak snowpack and streamflow (Rosenberg, Wood, and Steinemann 2011). These approaches lack the necessary physical base to cope with a changing climate that is characterized by an increased frequency of extreme weather and the earlier-than-usual onset of snow melt (California Department of Water Resources 2017; Roger C. Bales et al. 2006; Stewart, Cayan, and Dettinger 2004; Stewart, Cayan, and Dettinger 2005).

To mitigate the effects of such adverse climatic conditions, multiple stakeholders such as Pacific Gas and Electric (PG&E) and the California Department of Water Resources (DWR) are starting to adopt physically based process models, as is the National Weather Service (Franz et al. 2003). These models can use continuous update by measurement-derived products of snow and soil moisture. This in turn begets the crucial problem of accurately estimating the various states and inputs of such models, most importantly the spatial SWE in real-time (Sami A. Malek et al. 2017), which is the main goal of this paper.

Snow distribution in mountains is not spatially homogeneous at any scale and has been shown to depend, during both accumulation and ablation periods, on physiographic and vegetative features. Operational snow pillows, consisting of sparsely scattered point measurements of SWE across California's mountain basins, have been installed and maintained by DWR since the 60s (*Department of Water Resources California Data Exchange Center* n.d.). They directly measure SWE from the weight of deposited snow and upload them via GOES satellites. Data are seamlessly published and can be retrieved from the California Data Exchange Center (CDEC) (*Department of Water Resources California Data Exchange Center* n.d.). Snow pillows, lacking spatially representative information on SWE, are complemented by manual monthly snow-course measurements that are often located near the snow pillows. It has been shown that those surveys underestimate peak season snow because peak snow does not regularly occur during those sampling dates (L. Montoya, Dozier, and Meiring 2014). Such techniques suffer from lack of spatio-temporal representativeness and a better sampling approach is needed. Moreover, there are practical challenges and difficulties associated with those measurement techniques. Snow-pillows require a flat surface and are often installed in open areas mostly accessible in lower but less representative locations. Harsh remote environments are isolated from the power grid and thus power consumption is a major limitation for such systems. Extreme weather events and wildlife tend to damage the equipment. Manual snow surveys, although more representative, are labor and resource intensive, and not frequent or widespread.

Other techniques such as remote sensing of SWE provide large spatial coverage but suffer from two main limitations. First, cloud cover that is especially prominent during the accumulation season masks most of the desired information. Second, SWE under canopy is not accurately captured. Satellite observations of SWE such as AMSR-E (25 km resolution) are much coarser than the desired resolution. Landsat (30 m resolution) and MODIS (500

m resolution) on the other hand, do not observe SWE but rather fractional snow cover that, by converting to SWE via models, is likely to produce uncertain estimates, especially when pixels are totally saturated with snow. Airborne LiDAR is an attractive remote sensing option in terms of accuracy and spatial resolution, but is expensive and impractical at small temporal scales.

Welch et al. (2013) demonstrated that SWE exhibits strong inter-annual stationarity at the 500m resolution in the American River and exploited this knowledge to devise a rank-based sensor placement algorithm. Using a similar principle, Zheng et al. (2018) reported superior spatial interpolation results incorporating the nearest historical LiDAR derived SWE scan of the basins and distributed the residuals using Gaussian process regression with features such as canopy, slope, aspect and elevation. Erickson, Williams, and Winstral (2005) from Colorado also shows consistent patterns between years with dependency on dominant wind direction at each site.

Features that have been frequently included in SWE interpolation are elevation, vegetation, slope, aspect, and northness (Kerkez et al. 2012; Rice and Roger C Bales 2010; Varhola et al. 2010; S. R. Fassnacht, Dressler, and R. C. Bales 2003). Physiographically representative snow pack monitoring with high spatial and temporal resolutions is imporatnt for increasing the accuracy of SWE estimates and snowmelt runoff forecasts. Some studies found it desirable to include satellite observations of fractional snow cover as an explanatory variable in regression (D. Schneider, N. P. Molotch, and J. S. Deems 2017). The majority of temporally dense studies of snow reported in the literature have been conducted on the watershed-scale from which the described legacy features have been discovered. On the other hand, studies on the sub-km^2 are conducted at few snapshots (Grünewald et al. 2010; López-Moreno et al. 2014), often not more than one, of the snow season and the temporal evolution of the extracted features' effects is lacking.

Wireless Sensor Networks based systems provide an ideal solution that bridges the gap between high spatial and high temporal resolutions (Zhang, Steven D. Glaser, Watteyne, et al. 2016). Such systems allow for distributed autonomous sampling of virtually as many measurements as desired and can be deployed in rough topographic locations as well as under dense canopy. Thanks to time synchronization in wireless mesh communications, the WSN we use operates with ultra-low power with the coordinator and sensors power demands being met by solar power and Li-ion batteries. All electronics are housed in water-tight enclosures with interface holes drilled in the bottom of the boxes. Repeaters are placed so that each sensor node has at least two paths to the manager to increase redundancy and reliability. Backup storage of sensor data is replicated at the sensor node, manager node and server to minimize data loss.

Given the major implications in interpolation skill, we wish to know using WSN technology whether the inter-year consistency of snow patterns documented in the literature extend to the Feather River and to the sub-1 km^2.

The research reported here addressed four questions:

1. To what extent was the WSN-based system able to capture the spatial snow patterns,

beyond existing operational systems?

2. Give the major implications in interpolation skills, to what extent did the WSNs show a stationarity in the inter-year snow patterns?

3. What features describe most of the variance exhibited by the WSN and pillow SWE measurements on the local km^2 scale and watershed scale, respectively?

4. What is the potential improvement in lagged correlation with runoff from the WSN deployment?

In Section 3.2.1 we first describe the WSN-based end-to-end system. Then follows the collection and filtering process of SWE in 3.2.2, and the methods underlying each of the stationarity analysis in 3.2.3, the features selection in 3.2.4 and 3.2.5, and the runoff analysis in 3.2.6. Sections III and IV focus on presenting the results and answering the four basic questions set to lead this study.

3.2 Materials and methods

Three Wireless Sensor Networks (WSN) were deployed across the North Fork Feather River Basin in Northern California. Each WSN contains a cluster of 12 sensor nodes placed at physiographically representative locations that span across areas of approximately 1 km^2. A DWR snow pillow is located in each of our sites (Fig. 3.1).

3.2.1 End-to-End system

The WSN-based system samples hydrologic and network performance data. It integrates hardware and software components to cover all aspects of the data pipeline, from local raw measurements to remote user-friendly representations. The main elements of this end-to-end system are illustrated in Fig. 3.2, and is fully described and evaluated in the second chapter of this thesis.

Data sampling

Each site has a cluster of sensor node stations installed to capture the different features of the landscape that affect the spatial distribution of snow, including canopy cover density, slope, aspect and elevation.

Every 15 minutes, each mote in the cluster is triggered by an interrupt from the on-chip real-time clock (RTC). The various types of sensors connected to the mote then take measurements of temperature, relative humidity, snow depth, solar radiation, and soil moisture.

A series of 28 readings are taken for the snow depth to mitigate the effects of noise interference. Their mean and standard deviation are calculated and reported, with the standard deviation quantifying uncertainty.

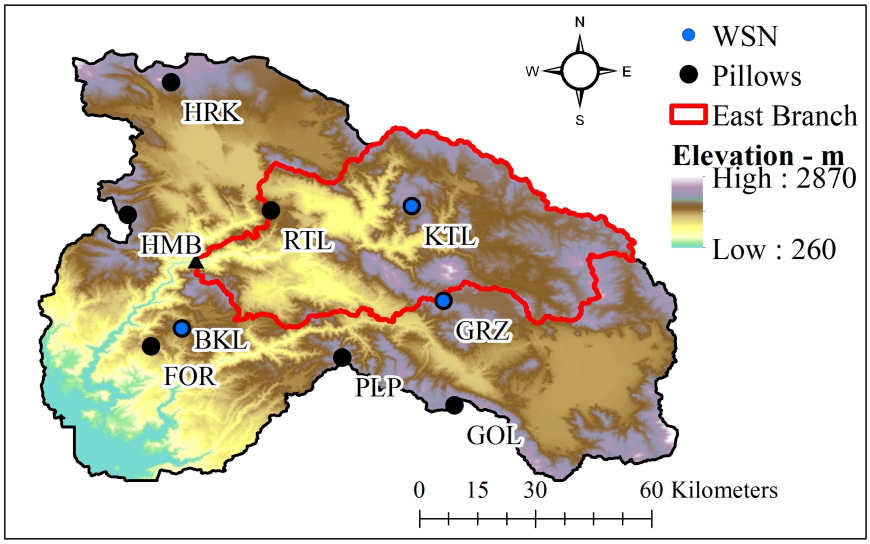

Figure 3.1: Feather River watershed elevation map (m) showing the snow-pillows across the basin. Three of the snow pillows (marked in blue) include a Wireless sensor Network. The red demarcation line contours the East Branch sub-basin. The black triangle label indicates where the East Branch flow meter is located.

Data collection and storage

The mesh properties of the wireless sensor network secure reliable and redundant paths from the sensor nodes to the manager. The manager forwards all received packets from the mesh network to the remote server via the cellular infrastructure or a satellite connection.

The system is capable of multi-level storage through the end-to-end Sensor Object Library (SOL) system that produces data representations appropriate for each level, while facilitating transmission throughout. First, the sensor nodes host an SD card where measurements are saved locally. Next, the manager stores data in its file system upon reception from the network. Finally, data that reaches the server is kept in a time series database.

3.2.2 Data quality control and preparation

To be able to analyze and compare measurements from the WSNs and existing systems, raw measurements must be converted into usable and similar time series. As is described in the sections below, WSN data require more filtering and transformation steps than the other data sources since it is required to transform 15-min distance-to-snow surface measurements into daily SWE. Measurements from all systems are converted into a final daily SWE product with gaps left unfilled.

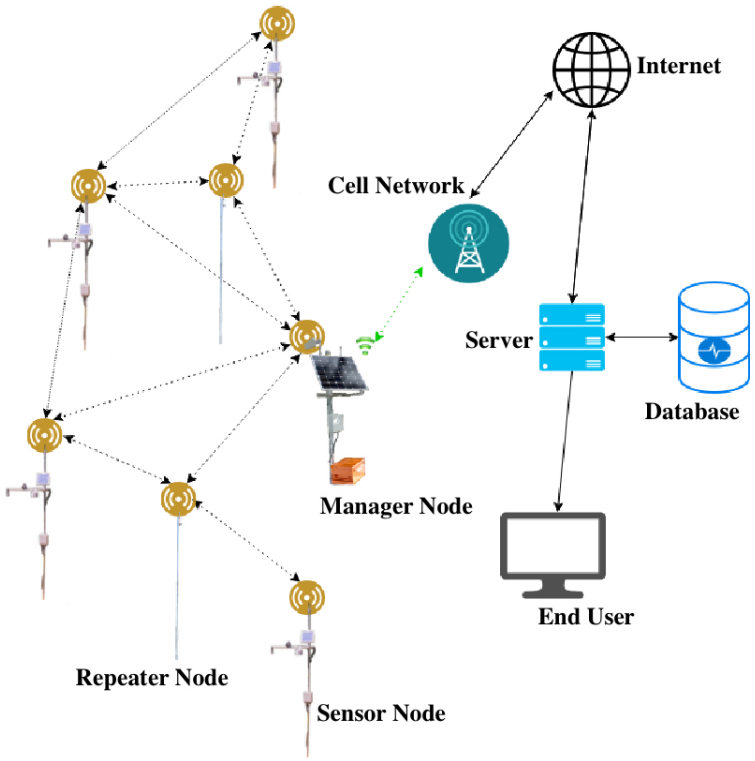

Figure 3.2: System architecture

Snow pillows/courses SWE estimate

Data from snow pillows and snow courses are downloaded from the California Data Exchange Center (CDEC) (*Department of Water Resources California Data Exchange Center* n.d.). All negative values are set to zero.

Sensor network SWE estimate

For every node of the WSN, distance-to-snow measurements taken every 15 minutes are aggregated daily using a weighted mean with weights computed from the standard deviation of the instantaneous 28 measurements described in 3.2.1. In this manner, measurements with high standard deviation are considered uncertain and thus receive less weight and their effect on the daily mean is reduced.

To get the snow depth for each sensor node, the distance-to-snow is subtracted from the height of the ultrasonic sensor. Next, a maximum-rate-of-change filter is applied to remove unrealistic jumps in the snow depth. Sensor measurements with standard deviations higher than the measurement are filtered out. We assume that such jumps are caused by electrical noise or vegetation blocking the sensor's range and causing sudden reduction in the distance-to-snow value, and consequently a sudden increase in snow depth measurement. They can also be due to heavy precipitation events. The ultrasonic wave could have reflected off water

and snow falling between the sensor and its ground reference, thus giving a deflated reading of distance to snow and consequently an inflated reading of SWE. Such phenomena are very volatile due to the nature of the precipitate movements in air. Their readings are captured by the high standard deviation of the 28 samples. Invalid data are filtered out, and represented as missing data in Fig. 3 and 4. Analysis of these samples is omitted.

To get the SWE from snow depth, the density of the snow is needed. For every site, one sensor node is co-located with the snow pillow, referenced as pillow node. Using snow depth from the pillow node and SWE from the snow pillow, we generate a time series of density. The snow density is assumed spatially homogeneous for every 1 km^2. Previous studies have shown that the spatial variation in the density has a little effect on SWE compared to the snow depth (Sturm and Goldstein 2017; Kirchner et al. 2014). Such an assumption is more liberally adopted in the literature (Zheng et al. 2018; Painter et al. 2016; Zhang, Steven D. Glaser, Roger C. Bales, Martha, Robert, et al. 2017). The date of the total melt of snow for each sensor node is further confirmed by the step increase in the soil temperature at 25 cm depth beneath it. For some sensor nodes, snow takes longer to melt compared to the snow pillow. Using the density value at the pillow during this time period is not desirable, as density could prematurely reach the maximum value. To solve this issue, the density time series at the pillow is first stretched in time to match the longer melt period of the sensor nodes and then applied in the conversion at those sensor nodes.

3.2.3 Inter-Year spatial stationarity

The study to analyze the inter-annual spatial stationarity of SWE was conducted on December to April data for each water year, using only stations that have less than 50% gaps for both years. Temporal mean deviation from the instantaneous WSN mean Δx_i for each sensor node i, is computed as:

$$\Delta x_i = \frac{1}{\Delta t} \sum_{t_i}^{t_f} (x_{i,t} - \mu_t) \tag{3.1}$$

where $x_{i,t}$ is the instantaneous SWE of sensor node i and μ_t is the instantaneous WSN mean. Δx_i quantifies the average yearly share of the WSN mean each station contributed. We can thus compute this metric for every water year to observe how it changes between the different years. Note that this method is vulnerable to unrealistic outliers, and thus outlier sensor nodes must first be removed. A higher change would imply weak spatial stationarity and vice versa. The metric can also be computed for each site to get an idea of the basin-scale spatial stationarity.

We also computed the rank of each sensor node in each site in terms of temporal mean SWE, or similarly the rank of each WSN site in a basin. For instance, the site, or station that has the highest mean SWE during the period of interest is assigned rank 1, the next highest rank 2, and so on until all sites or stations are sorted.

3.2.4 Feature selection

We use the Elastic Net (Hastie, Tibshirani, and Friedman 2009) as a method to select the most important features out of a pallette of 15, Table 3. We wish to know how those features linearly explain the daily variance in both the WSN SWE for the sites and snow pillow SWE for the watershed. Elastic net is a regularized linear regression with combined $L1$ and $L2$ regularization. $L1$ and $L2$ regularization alone are called LASSO and Ridge regularization respectively. The method is typically used with large feature sets, larger than the observed variable set. Assuming n is the number of samples and b the total number of features, it aims to find $\hat{\beta}$ that minimizes the objective function

$$\underset{\hat{\beta}}{\operatorname{argmin}} \left(\|y - X\beta\|^2 + \lambda_2 \|\beta\|^2 + \lambda_1 \|\beta\|_1 \right) \tag{3.2}$$

X is the design matrix that holds the n samples' b+1 feature values with dimension ($n \times b$+1), y is the observations vector with dimension ($n \times 1$) and β is the vector of $b + 1$ coefficients to be estimated, including the intercept with dimension ($b + 1 \times 1$).

The added regularization to the objective function updates the objective to simultaneously find both those coefficients that minimize the distance of the observations to the predictions, while minimizing the norm of the coefficients.

In other words, features that receive coefficients with large values are necessarily those that were able to effectively minimize that fitting distance. Features that are unable to minimize the distance are shrunken.

λ_1 and λ_2 are weights for the L1 and L2 norms of β respectively, and are chosen to be 0.5 each.

If the group of features has correlations, LASSO randomly chooses one and sets the coefficient of others to zero, even if they have a strong contribution to the observed variable. This is because setting the correlated features' βs to zero minimizes the L1 norm but not the L2 norm. For instance, in a hypothetical case where two features are exactly equal, using the L1 norm would set one of their coefficients to zero while using the L2 norm will set their coefficients equally to a certain variable. This elimination effect of LASSO is not always desirable, since first, the eliminated feature might better explain unobserved locations, and second, a little correlation is acceptable in our goal to visualize explanatory features. On the other hand, LASSO might better fit the data when the features predict well the observed variable and the sample size is small compared to Ridge. This is due to the lower L1 penalty term relative to the distance term. Elastic net combines both methods. The optimization to find $\hat{\beta}$ is performed using the coordinate descent algorithm. More details can be found in Hastie, Tibshirani, and Friedman (2009) and Zou and Hastie (2005).

Features with a high variance inflation factor were not chosen to avoid strong multicollinearity. Features that have high magnitude coefficients after fitting the elastic net model regression with the data are extracted and their individual coefficient of determination r^2 is computed daily for each site - that is the proportion of the variance in the dependent variable that is predictable from the independent variables. The experiment is similarly done on the

watershed scale using only available snow-pillow data. Note that r^2 does not necessarily reflect the predictive performance, but simply what features were able to fit best all the data collected since we are not using withholding experiments or cross-validation.

3.2.5 Added explanatory variables

The novel features introduced are: (1) *nnMarg*, (2) *sur-canopy*, (3) *inorth*, *ieast*, *isouth* and *iwest*, defined below and described in table 3.1.

Nearest Neighbor

The Nearest Neighbor (NN) scheme consists of finding the daily historical SWE map that minimizes the distance between all current SWE observations and the historical SWE values at the same locations. We name it *nnMarg*. Assuming the collection of historical maps $\mathbf{y}$ range from days 1 to N, and that each vector $\mathbf{x}_d$ of n SWE measurements at specific locations and specific day d is associated with its full spatial SWE map $\mathbf{y}_d$ from the collection, *nnMarg* can be expressed using the following equation: For a given vector of observations $\mathbf{x}_k$ on day $d = k$, and i ranging from 1 to N, where N is the number of historical SWE maps, we find the day $\hat{i}$ that minimizes the Euclidean distance:

$$\underset{\hat{i}}{\operatorname{argmin}}\{\|\mathbf{x}_k - \mathbf{x}_i\| \mid i \in [1, N]\} \tag{3.3}$$

And more precisely:

$$\underset{\hat{i}}{\operatorname{argmin}}\{\sum_{j=1}^{n}(x_{kj} - x_{ij})^2 \mid i \in [1, N]\} \tag{3.4}$$

The best match historical scene is then the map $\mathbf{y}_{\hat{\mathbf{i}}}$ of past day $\hat{i}$.

The historical dataset used for the Feather River is a newly developed state-of-the-art SWE Bayesian reanalysis dataset over the Sierra Nevada (US) based on the assimilation of remotely sensed fractional snow-covered area data over the Landsat 58 record (Margulis et al. 2016). The reanalysis dataset ranges from 1985 to 2015. The product's spatial and temporal resolutions are 90 m and daily, respectively. A comparison with in-situ data showed a mean and root-mean-square errors (RMSE) less than 3 and 13 cm, respectively (Margulis et al. 2016). Although the general NN method have been used previously to find a spatial background estimate of SWE (Zheng et al. 2018), it was never used as regression variable nor with the state-of-the-art product described above. The advantage of using it as a regression feature over a fixed background estimate is the possibility of scaling introduced by the regression coefficients, allowing for an effectively larger historical space. Dominik Schneider and Noah P. Molotch (2016) used a similar regression-based approach but by finding a match from a historical 500-m reconstruction-based ensemble that minimized the cross-validation error with the station observations.

Surrounding canopy

We use the feature named *sur-canopy* to quantify the extent of surrounding canopy at each point. It consists of averaging the surrounding canopy values of a pixel and subtracting its own value. Such feature should show effects of snow redistribution during precipitation and potentially shading effects during snowmelt.

Incident storms

We introduce a set of novel features that attempt to capture the effect of topography on incoming storms from the four directions. The storm directional path is abstracted by a raking light source at zero altitude and its effect the same as hillshade. Hillshade is computed using aspect and slope of the topography and using the zenith and azimuth of the point source as the following equation shows - all angles in radians:

$$\begin{aligned} Hillshade = 255.0 \times [(\cos(zenith)\cos(slope)) + \\ (\sin(zenith)\sin(slope)\cos(azimuth - aspect))] \end{aligned} \tag{3.5}$$

As its name indicates, it models the shading caused by reliefs blocking the point source. Fully illuminated slopes are expected to have very little hillshade. Conversely, fully "illuminated" slopes are expected to receive the majority of snowfall, at least more than the shaded regions. *inorth*, *ieast*, *isouth* and *iwest* are computed from equation 3.5 with *azimuths* 0, 90, 180 and 270°, respectively. The *zenith* angle for all is set to 90°, modeling the shading effect of a raking light. This is a different approach than the wind effects previously used in the literature such as the wind sheltering-exposure indices presented in Lapen and Martz (1993) or the drift zones delineations in Winstral, K. Elder, and R. E. Davis (2002).

Other topographic features

TPI, the Topographic Position Index compares the elevation of each cell in a Data Elevation Model (DEM or elevation) to the mean elevation of a specified neighborhood around that cell. The higher and lower its value is, the more convex and concave the surface is respectively. *TPI100* is the same index computed on a down-sampled DEM of 100-m resolution allowing for a wider delineation of ridges and valleys compared to *TPI*. *Roughness* describes the maximum change in DEM between the pixel and its surrounding.

3.2.6 Normalized cross correlation with runoff

To quantify the potential predictability of runoff from SWE and its melt dynamics, we compute the normalized cross correlation (NCC) between the measured SWE and negative ΔSWE (approximating snow melt), and the measured natural flow downstream of the sites at the outflow of the East Branch of the North Fork of the Feather River. We correlate lagged runoff with both the mean SWE of the WSN stations and the SWE of the snow pillow to

Table 3.1: Features used in Elastic Net regression.

Feature Name	Description	Units	Res.
elevation	elevation from sea level	m	10 m
canopy	canopy coverage percentage	%	10 m
aspect	direction of steepest drop	-	10 m
longitude	longitude of the pixel	dec	N/A
sur-canopy	relative surrounding canopy percentage	%	10 m
inorth	northern exposure to precipitation	-	10 m
isouth	southern exposure to precipitation	-	10 m
ieast	northern exposure to precipitation	-	10 m
iwest	western exposure to precipitation	-	10 m
hillshade	shading caused by elevation	-	10 m
TPI	difference between the value of a cell and the mean value of its 8 surrounding cells	-	10 m
TPI100	down-scaled topographic position index (see above row)	-	100 m
roughness	largest inter-cell difference of a central pixel and its surrounding cell	-	10 m
nnMarg	nearest neighbor with historical Landsat-assimilated SWE map	mm	90 m
northness	orientation of the slope relative to North	-	10 m

evaluate the WSN's spatial sampling advantage's potential effect on runoff forecasting. NCC can be expressed as:

$$NCC(d) = r \star s = \sum_{n} \frac{r[n+d] \times s[n]}{\sqrt{s^T \cdot s \times r^T \cdot r}} \tag{3.6}$$

Where d, s and r are the lag days, SWE and runoff respectively. The above function is computed after specifying a lag d. The lag represents the number of days the runoff time series is shifted in the past relative to the SWE time series before the metric is computed. NCC is computed for every lag from 0 to 200 days.

3.3 Results

3.3.1 Spatial representativeness of snow pillows

The daily SWE reported by the snow pillow, the snow courses surveys and each sensor node of the WSN are shown in Fig. 3.3, after quality control and assurance, and the transformation operations described in 3.2.2 were applied on the data.

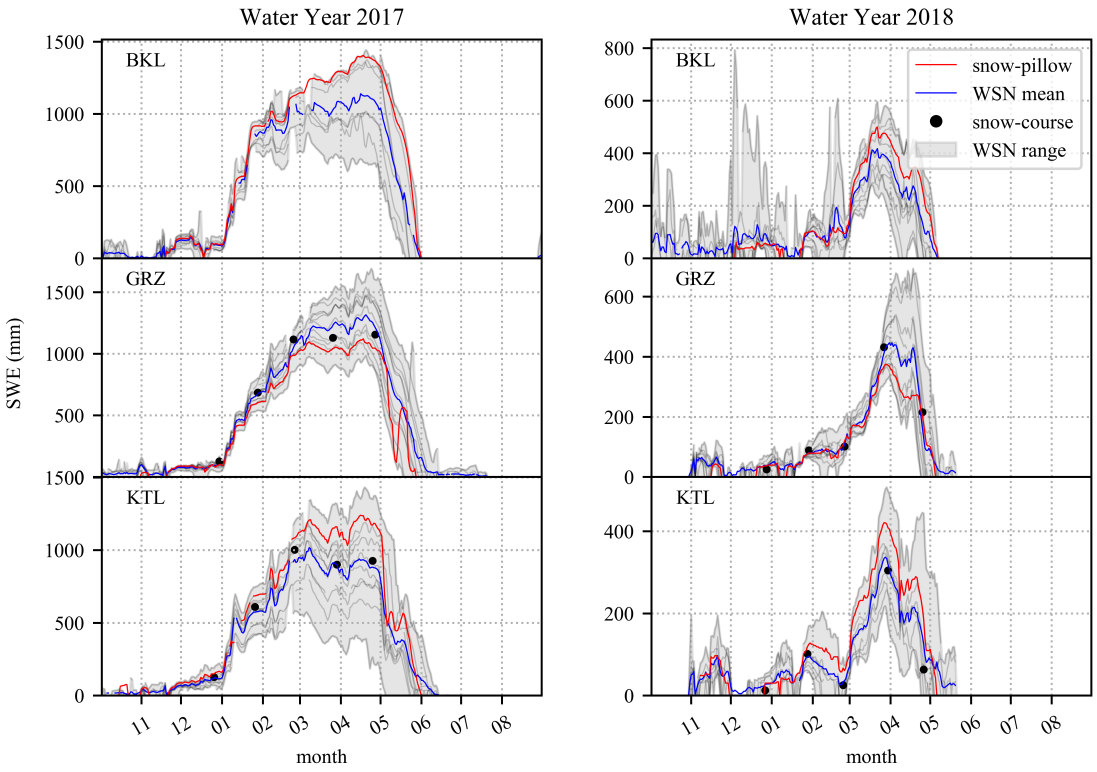

Figure 3.3: SWE for water years 2017 and 2018 reported by snow pillows, snow courses and WSNs for the three study sites BKL, GRZ and KTL. The grey lines denote the SWE reported by each WSN site sensor node. The grey shading covers the range of those WSN measurements.

The SWE of the WSN sensor nodes drawn in gray lines show a high deviation from their mean, reaching up to 28%, 40% and 58% during peak snow season of water year 2017 for the lowest SWE reporting node at GRZ, BKL and KTL respectively. The final part of the melt season shows an even higher proportion of deviation, reaching 100%. Note that the envelope around the mean, which encloses the range of deviation from the mean, increases with snow accumulation and melt events and thus on average increases continuously as the season progresses. This would also be reflected in the coefficient of variation, which is high

during peak snow season and highest during the final melt period where the WSN mean SWE decreases, but the amount of deviation from the mean does not decrease.

On most days, the snow-pillow SWE measurements were higher, lower and higher than the WSN mean for sites BKL, GRZ and KTL respectively.

Snow pillows were biased compared to the mean WSN for all years and all 1 km^2 sites, and their bias sign was consistent for both a wet and medium water years, 2017 and 2018, respectively.

The snow pillow over-estimates the regional 1 km^2 scale SWE when compared to the mean of 12 sensor nodes at BKL, severely for WY 2017, and slightly for WY 2018. It under-estimates the regional 1 km^2 scale SWE when compared to the mean of 12 sensor nodes at GRZ, significantly for both water years. And it over-estimates the regional 1 km2 scale SWE when compared to the mean of 12 sensor nodes at KTL, significantly for both water years.

The pillow bias from the WSN mean is highest during the peak snow season for all cases. At melt, the majority (around 90%) of the WSN sensor nodes at BKL report a disappearance of snow before the snow pillow does for both water years. Conversely, the mean WSN SWE at KTL reaches zero more than 10 days after the snow pillow.

Snow courses measurements all fall within the WSN range, and are in the majority of cases (16 out of 20) closer to the WSN mean than the pillow is.

3.3.2 Conservation of inter-year spatial stationarity

The temporal mean deviation from the WSN mean is computed for each site sensor node, and is shown in Table 3.2. There is a strong intra-site preservation in the direction of deviation between the two years 2017 and 2018. At BKL, KTL and GRZ, 75%, 75% and 90% of the stations analyzed preserved the direction of their deviation from their WSN mean respectively.

The Change(%) column presents how each node varies in the amount of deviation between the years. The majority of the nodes, 21 out of 26, showed less than 10 percent inter-year deviation. Only BKL 4 diverged with some significance from the trend.

As another indicator of spatial stationarity, the rank allows us to see where each sensor node stands in terms of SWE amount compared to the others at the same site, and to what extent this standing between the years remains conserved. At BKL four out of eight stations showed a preservation of their rank (+-1) relative to the other stations between water years 2017 and 2018. At GRZ, a majority of seven out of ten nodes preserved their relative rank (+-1). Best stationarity was observed at KTL, with 100% of the stations maintaining their rank (+-1). Again, of all the surveyed nodes only BKL 4 (+6) exhibited significant rank change.

The last three rows of Table 3.2 show the analysis applied to the three sites after aggregating their sensor nodes' measurements. The sign of the deviation was preserved for GRZ and KTL, but not for BKL. BKL shows an inter-site mean in the amount of deviation higher (31%) than GRZ and KTL during the dry year and lower (-17%) than GRZ during the wet year 2017. It also increased in rank at the expense of GRZ, while KTL preserved its lowest

Table 3.2: Changes in percent deviation from mean and relative rank for each sensor node and each site between water year 2017 and 2018.

Site node_id	2017(%)	2018(%)	Change(%)	2017R	2018R	RChange
BKL 1	-8	-18	-10	4	1	-3
BKL 2	10	2	-8	5	5	0
BKL 3	-7	-9	-2	3	3	0
BKL 4	-11	23	34	2	8	6
BKL 6	-23	-19	4	1	2	1
BKL 7	11	-1	-12	6	4	-2
BKL 8	16	15	-1	7	7	0
BKL 10	15	13	-2	8	6	-2
GRZ 2	17	18	1	10	9	-1
GRZ 3	-8	-12	-5	4	2	-2
GRZ 4	9	8	-1	8	8	0
GRZ 5	10	1	-9	9	6	-3
GRZ 6	-8	-9	-1	3	4	1
GRZ 7	10	5	-5	6	7	1
GRZ 8	-17	-13	4	1	1	0
GRZ 9	-14	-9	5	2	3	1
GRZ 10	1	-5	-6	5	5	0
GRZ 11	6	21	15	7	10	3
KTL 2	-8	-6	2	3	4	1
KTL 3	9	-1	-9	6	5	-1
KTL 4	-25	-18	8	1	1	0
KTL 5	0	-9	-9	4	3	-1
KTL 6	-18	-17	1	2	2	0
KTL 7	9	11	2	7	7	0
KTL 8	5	3	-2	5	6	1
KTL 12	26	37	11	8	8	0
BKL Mean	-17	31	49	2	3	1
GRZ Mean	50	19	-31	3	2	-1
KTL Mean	-33	-50	-17	1	1	0

Percent deviation from mean (2^{nd} and 3^{rd} columns), 2017 to 2018 change in the percent deviation (4^{th} column), rank (5^{th} and 6^{th} columns), 2017 to 2018 change in the rank (7^{th} column) of each WSN sensor node and site.

rank. KTL had uniformly the lowest amount of SWE for both years, even though it has the highest elevation. Moreover, BKL as the least elevated site had the highest of the three sites during the dry 2018 water year.

3.3.3 Feature importance

We show in Fig. 3.4 to 3.7 sample results that characterize the importance of the features at the local 1 km^2 and the watershed scale, for years 2017 and 2018, with the rest presented in the supplement. Results show that the most important features are different at each WSN site, Fig. 3.4. Both newly introduced *iwest* and *isouth* explained significant amount of the 2017 SWE variance at BKL and KTL, respectively. At the watershed-scale, *nnMarg* remains prominent for both the dry and the wet year, Fig. 3.7.

Fig. 3.4 reveals the coefficients of determination (r^2) of the linear fit of daily SWE with the important features chosen from a pool of 15, for each of the WSN sites KTL and GRZ. Fig. 3.5 is similar to Fig. 3.4 but using available snow-pillow data across the watershed. The choice is based on the magnitude of the Elastic Net coefficients described in 3.2.4.

At BKL, Fig. 3.4a shows that *iwest* and *TPI100* have consistently high r^2 during the majority of the water year 2017, where they are highest during the beginning of the season reaching 0.8 for each and decreasing linearly throughout the remainder of the season where the two features diminish in importance during the latter part of spring melt. We note that *iwest*'s r^2 peaks with the majority of the snow accumulation events and is sometimes accompanied with *elevation* and *roughness* (Fig. B.1).

nnMarg's r^2 is mostly prominent during melt phases at the beginning (0.78) and end (0.65) of the season at KTL when there is relatively little snow 3.4b. *Northness*, *sur-canopy*, *inorth* and *TPI*, show up substantially in an exponential increase at the final spring melt phase (Fig. B.1).

During 2018, the *nnMarg* feature is uniformly relevant at BKL (Fig. B.2), followed by *iwest* and *sur-canopy* (Fig. B.10 and B.14). Yet there were no coefficients higher than 0.6 during the peak of the snow season (Fig. B.2).

At GRZ, *longitude* is the most prominent feature compared to the other sites (Fig. B.11 and B.12). *nnMarg* could explain SWE variability during the non-peak 2017 snow season (Fig. B.3), as also observed at BKL 2017 (Fig. B.1).

During water year 2018 at GRZ, *TPI* was able to explain up to 70% of the spatial variability after the melt of mid-February as shown in Fig. B.4, and is generally significant for all sites after melt events. *Aspect* and multiple other features had weak contributions as shown in Fig. B.4. *TPI100* maintained an explanation of around 0.4 throughout most of the season. *longitude* was prominent as well and peaked in the end of the season.

At KTL, the most consistent explanatory variable during the peak snow season of water year 2017 was *isouth* (Fig. 3.4b). *nnMarg* at r^2 up to 0.8 explained well the SWE distribution during accumulation and melt, unlike other sites. *Elevation* reached a r^2 of around 0.2 on average at KTL, much less than other features. During final melt, *aspect* and *nnMarg* were

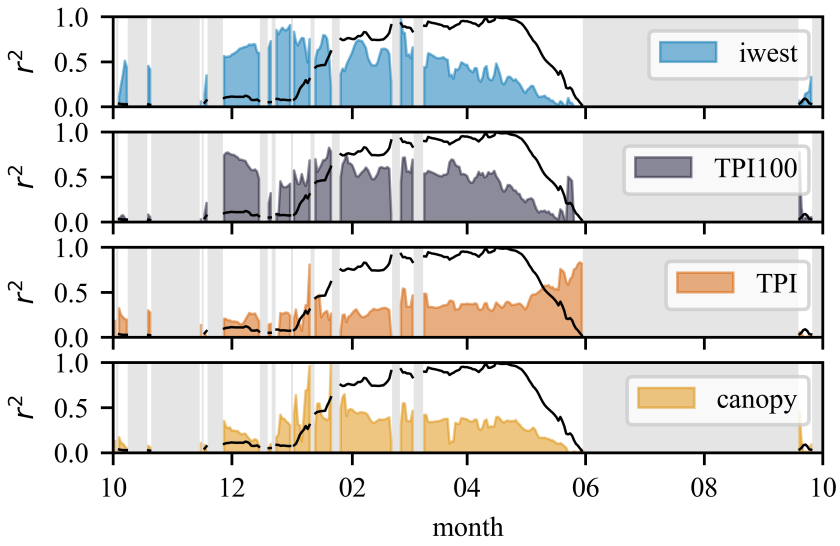

(a) BKL, water year 2017

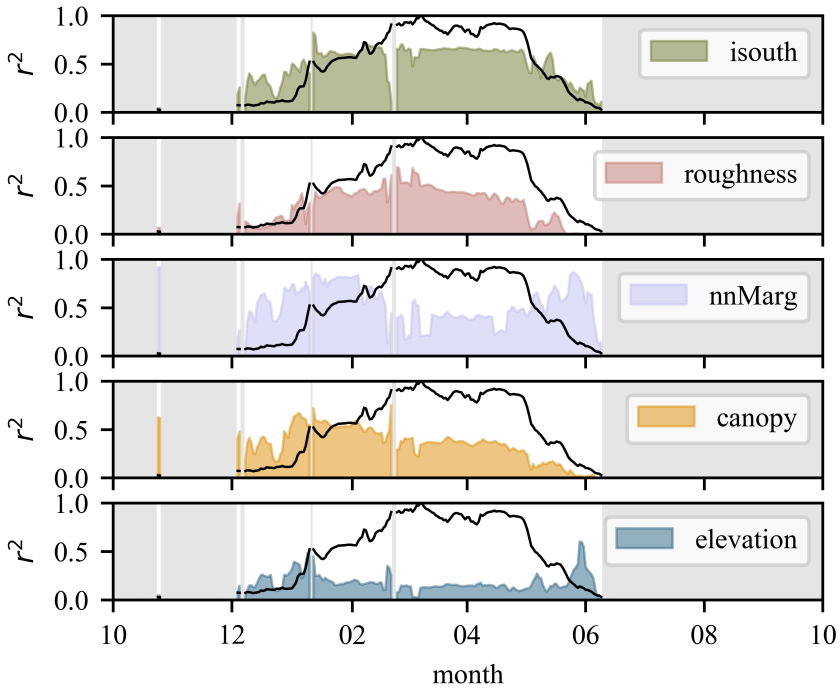

(b) KTL, water year 2017

Figure 3.4: Daily coefficient of determination r^2 for the selected features that have high Elastic Net coefficients for water year 2017 at the WSN sites (a) BKL and (b) KTL (shaded colors). The WSN mean SWE scaled to the 0-1 range is added to each sub-figure for reference (solid black line). Shaded areas indicate time spans with not enough valid data.

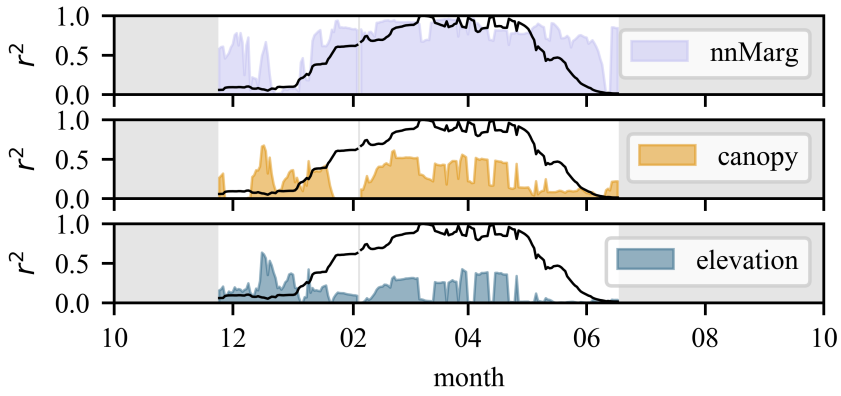

(a) Watershed snow pillows, water year 2017

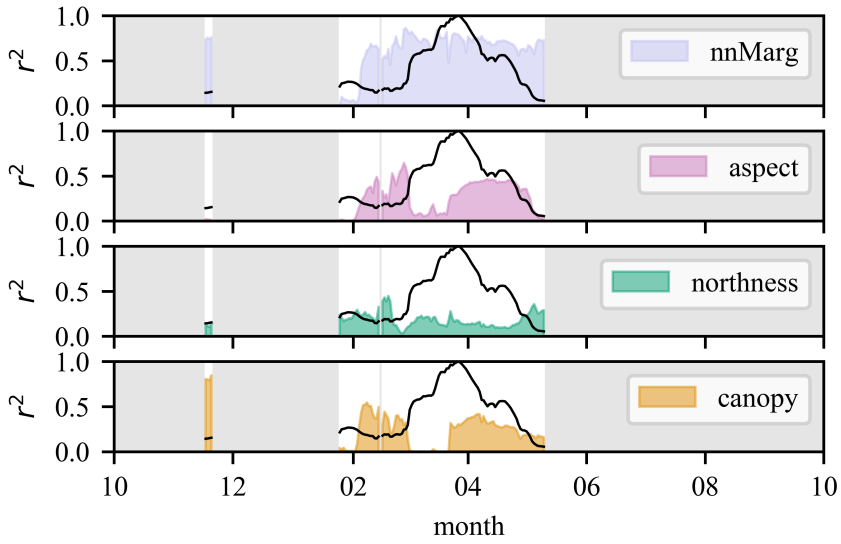

(b) Watershed snow pillows, water year 2018

Figure 3.5: Daily coefficient of determination r^2 for the top selected features from the Elastic Net fit of the SWE of the snow pillows across the watershed for water years (a) 2017 and (b) 2018. The snow pillows' mean SWE scaled to the 0-1 range is added to each sub-figure in black for reference. Shaded areas indicate time spans with not enough valid data.

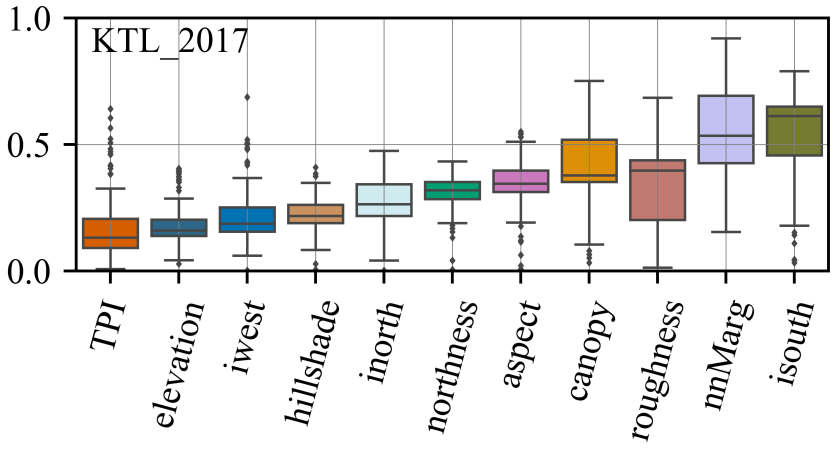

(a) r^2

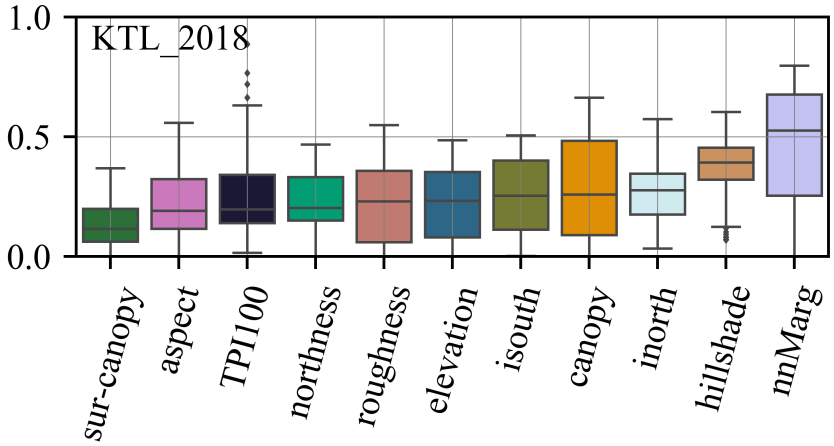

(b) r^2

Figure 3.6: Box plot for yearly statistics of the squared Pearson correlation coefficient of features with SWE for each of the sites (KTL is shown here, the rest are in the supplement) and water years. Only features with r^2 greater than 0.1 are included.

dominant. *nnMarg* explained relatively well KTL's dry 2018 year SWE distribution up to a coefficient of 0.8 (Fig. B.6).

With respect to the basin-wide snow pillows, the most significant features are represented daily in Fig. 3.5. See supplement for additional features. They show that *nnMarg*'s r^2 was continuously high compared to other features reaching above 0.97 and 0.87 for some days of the water years 2017 and 2018, respectively. *Canopy* had the second highest during the wet year's snow season only with average r^2 of around 0.45. *aspect*, *canopy* and *iwest* were observed during the spring snow melt period of water year 2018.

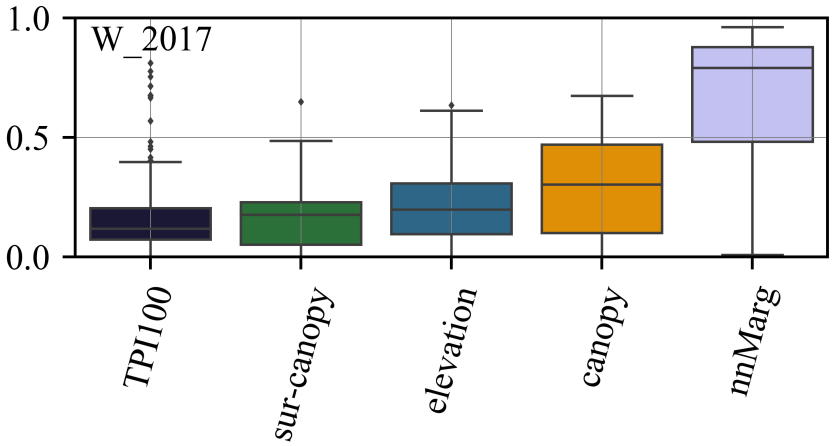

(a) r^2, basin-wide snow-pillows

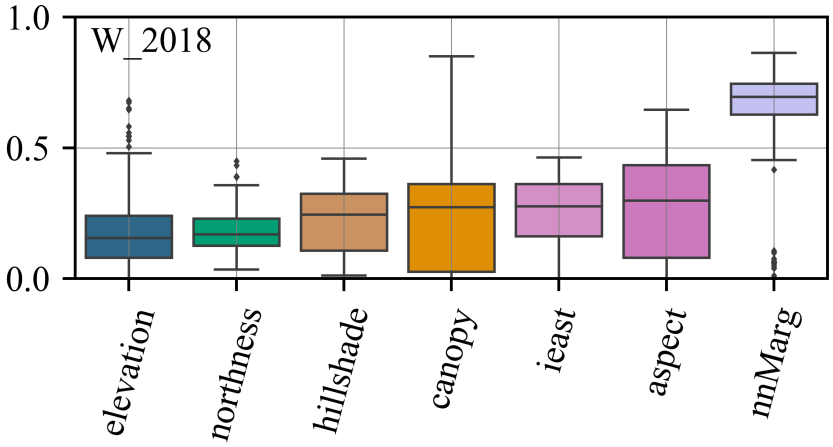

(b) r^2, basin-wide snow-pillows

Figure 3.7: Box plot for yearly statistics of the squared Pearson correlation coefficient of features with SWE for the watershed. Only features with r^2 greater than 0.1 are included.

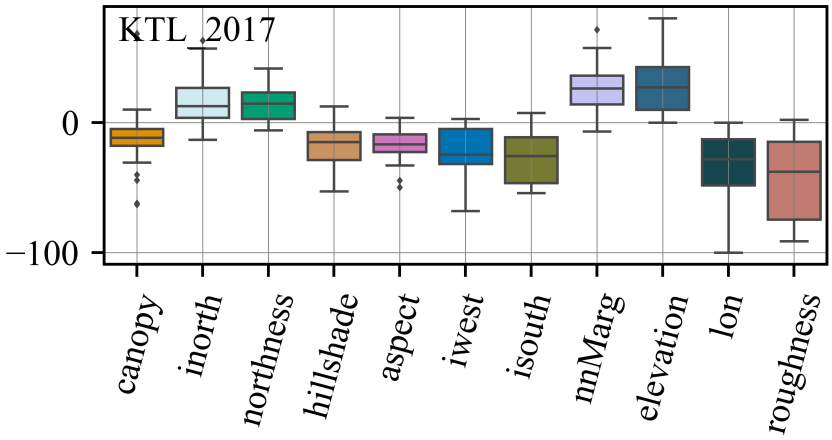

(a) Importance

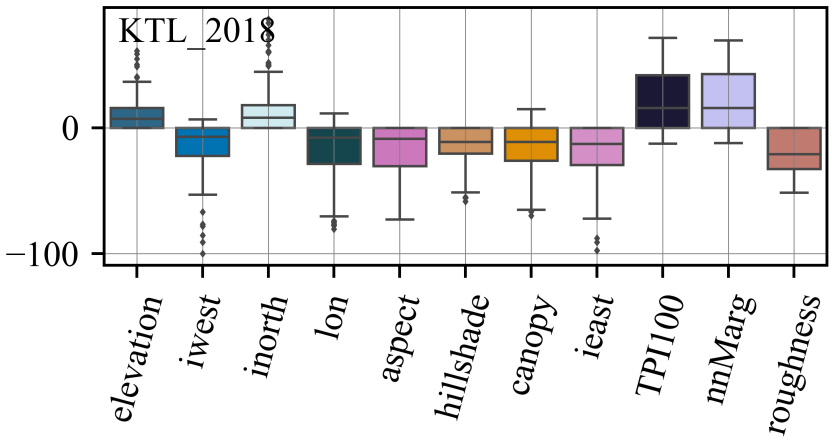

(b) Importance

Figure 3.8: Box plot for yearly statistics of the relative feature importance of the Elastic Net for each of the sites (KTL is shown here, the rest are in the supplement) and water years. Negative coefficients indicate that given feature is negatively correlated to SWE. Only coefficients with relative importance of more than 15% are shown.

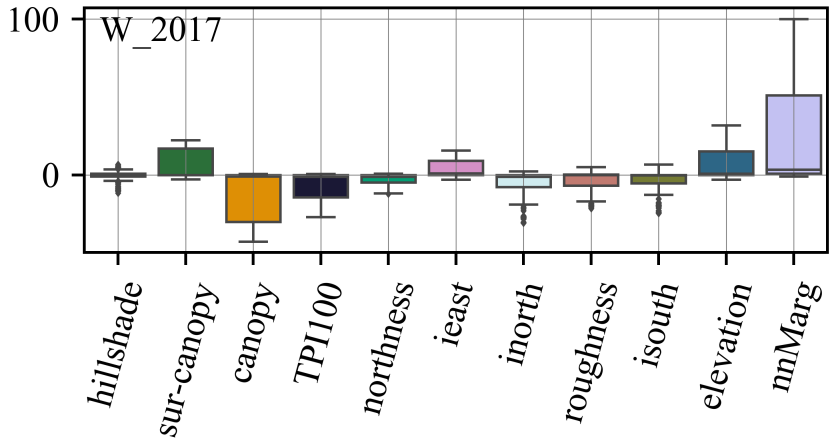

(a) Importance, basin-wide snow-pillows

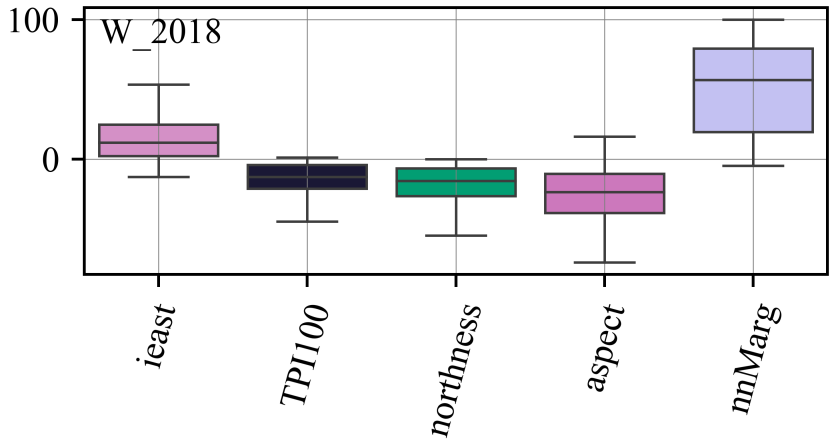

(b) Importance, basin-wide snow-pillows

Figure 3.9: Box plot for yearly statistics of the relative feature importance of the Elastic Net for the watershed. Negative coefficients indicate that given feature is negatively correlated to SWE. Only coefficients with relative importance of more than 15% are shown.

Figures 3.6 to 3.9 show the yearly aggregated r^2 and relative importance of each feature, respectively. The sign of the importance coefficients is preserved in Fig. 3.8 and 3.9 to show the Elastic Net model's fit result in terms of positive or negative correlation with SWE. *Aspect* in Fig. 3.9b is on average negatively correlated with SWE given the measurements, unlike *elevation* in Fig. B.13 and 3.9a. Many features preserved their importance and direction from 2017 to 2018 for GRZ (*lon*, *TPI*, *TPI100*, *sur-canopy*, *isouth*, *roughess*) and for KTL (*roughness*, *nnMarg*, *elevation*, *canopy*, *aspect*, *iwest...*), but not much for BKL (*iwest* and *sur-canopy* only).

3.3.4 Normalized coefficient of correlation with runoff

In the NCC analysis, BKL is not included because the site is not located upstream of the flow meter in the East-Branch (EB) sub-basin. Only water year 2017 is shown because flow measurements for year 2018 are not yet available.

The NCC of the WSN daily SWE loss (simulating snow melt) with flow measurements was considerably higher for both GRZ and KTL, for the majority of the lag days (reaching up to 100% for some lags) compared to the snow pillow estimate as shown in Fig. 3.10a and 3.10b, respectively. Hence, the WSNs at GRZ and KTL provided noticeable improved forecast of the snow melt dynamics for the East-Branch sub-basin, in comparison to the estimate of the snow pillow present at the sites.

3.4 Discussion

Snow pillows often measure biased estimates of the local SWE average as shown by comparison to the deployed WSNs. Sometimes, variations are noticed even with sensor nodes in direct proximity to the pillow, especially in the presence of trees (Meyer, Jin, and Wang 2012). Node 7 at GRZ, which is situated not more than 10 m away from the snow pillow, seems to have received much more snow than the pillow, and took approximately one week longer for snow to totally melt. Snowcourse surveys typically take monthly samples from 10 points in transects from single locations inside the 1 km^2 from October to April. Our results confirm that snow-course measurements in their majority are spatially more representative than the snow pillow since they follow more closely the WSN mean than the pillows do. However, snow courses can still have considerable bias in representing the 1 km^2 as shown in the case of GRZ 2017 (Fig. 3.3),

We have shown that Wireless Sensor Networks constitute a high-temporal-resolution distributed-sampling technology that is able to mitigate some of the shortcomings of existing operational methods for representative sampling. An added advantage is that the areal coverage of WSNs can be much broader and representative than that of snow courses. This high spatial variability of SWE exhibited in less than 1 km^2 for all sites and both water years is not surprising and similar results have been previously reported in the literature.

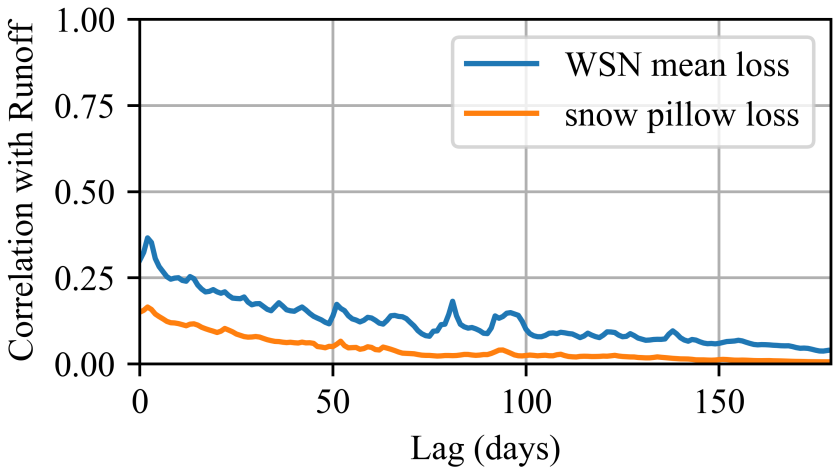

(a) GRZ, 2017

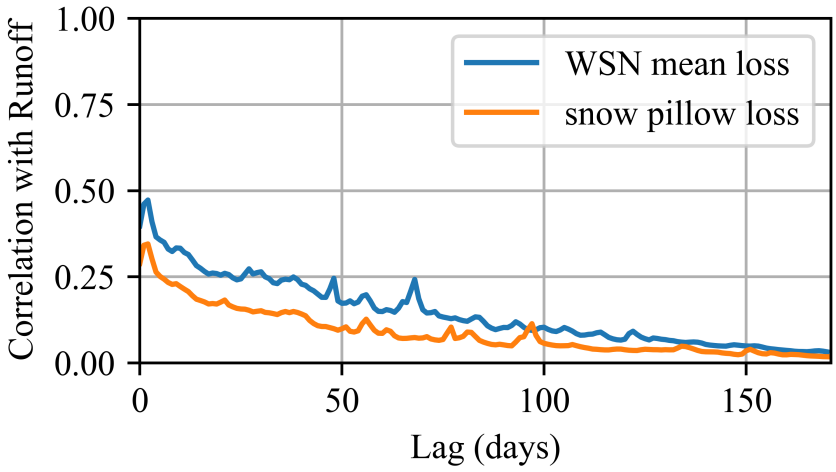

(b) KTL, 2017

Figure 3.10: Normalized cross correlation coefficient of the SWE loss (snow melt) reported by each measurement system: snow pillow in yellow and aggregated WSN in blue, with runoff for different lags at (a) GRZ and (b) KTL.

Studies in Colorado show that the spatial variability of SWE at the local scale (50 m) can be as large as that on the watershed scale (Clark et al. 2011).

We have shown that this spatial variability increases as the snow season progresses and is highest during melt season after the snow-pack had accumulated variability from multiple precipitation and melt cycles. The widening of the envelope in Fig. 3.3 during snowfall compared to melt imply that precipitation events add more variability to SWE than melt does at this scale. This suggests that features that explain the spatial variability of these accumulation periods will have a sustained strong impact on the distribution of snow throughout the snow season until either the snow melts or a new storm occurs. This lasting spatial effect of accumulation season storms is most clearly revealed during water year 2017 at KTL with *isouth* and *roughness* in Fig. 3.4b; at GRZ with *roughness* and *canopy*; and at BKL with TPI100 and *iwest* in Fig. 3.4a.

Nevertheless, high variability exhibited spatially is not apparent inter-annually. Results show a strong preservation of the spatial distribution of SWE from year to year. It is important to note that our study was conducted between two very different water year types: one of the wettest years on record and a dry year, where one would intuitively think consistency would not be observed as well as it would between similar year types. Even though the relative amount of deviation from the WSN mean varies, for some cases significantly, its direction (sign) is generally conserved (e.g. nodes GRZ 5, GRZ 11, KTL 12, BKL 1). Similarly, spatial stationarity rank-wise was preserved even at the watershed scale (+-1). This corroborates previous findings of strong inter-annual stationarity of the spatial distribution of SWE (Dominik Schneider and Noah P. Molotch 2016; Erickson, Williams, and Winstral 2005; Jeffrey S. Deems, Steven R. Fassnacht, and K. J. Elder 2008; Schirmer et al. 2011). For instance, Erickson, Williams, and Winstral (2005) found a similar pattern in the maximum accumulation during two study years, with a correlation of up to 0.97. The dataset in Erickson, Williams, and Winstral (2005) from Colorado shows consistent patterns between years as well, with dependency on dominant wind direction at each site. This inter-annual consistency in mountain snow distribution was exploited in the spatial interpolation method of Zheng et al. (2018), where the nearest neighbor technique was used to find the best historical LIDAR scan fit with current conditions. The corollary is that relative bias in the spatial representativeness of snow pillows at GRZ and KTL (and potentially other locations) is likely to be uniform between different years.

Comparing water years 2017 and 2018, mean annual SWE at GRZ decreased from 50% to 19% of mean annual SWE across the three sites. Similarly, mean annual SWE at KTL decreased from -33% to -50% of mean annual SWE across the three sites. However, BKL showed an opposite trend, with water year 2017 and 2018 representing -17% and 31% of mean annual SWE across the three sites. Given its location on the western rain-shadow of the watershed, BKL is the first site to receive precipitation. During a dry year, most storms are likely exhausted before they reach the deeper and dryer side of the watershed where GRZ and KTL are located. Further studies spanning multiple wet and dry years can validate this phenomenon. GRZ is at a higher elevation than BKL and has an uninterrupted topographic opening that extends to the mouth of the basin, and from there all the way to

the Pacific Ocean, which could explain why it received the most SWE. On the other hand, the relatively remote and shielded location of KTL shades it from most incoming seasonal atmospheric rivers and storms. For example, GRZ is located on a ridge that could attenuate some of these storms.

The previous analysis is in line with the 30-year normal legacy PRISM (Parameter-elevation Relationships on Independent Slopes Model) precipitation map shown in Fig A.1 that reveals a decrease in the precipitation gradient starting highest from the south-west boundaries, as well as a higher precipitation normal at BKL followed by GRZ and finally KTL. Although Fig. A.1 suggests that BKL should have the highest precipitation, a considerable percentage of precipitation would be rain and not snow due to the site's low elevation and consequently does not contribute to SWE.

Features that contribute to the stationarity relate to topography, vegetation, solar radiation and even seasonal storm and wind directions. Scattered storms and small-scale wind distribution and precipitation events are likely to decrease stationarity. BKL, the site where we observed the least relative stationarity in SWE distribution is the one with the most precipitation occurring as rain, and this could suggest that mixed rain-snow regions increases the inter- and intra-yearly spatial variability of SWE. Consequently, a warming climate would decrease the skill in historical-based snow-interpolation techniques.

As also noted by Clark et al. (2011), Fig. 3.6 to 3.9 reveal that spatial variability of SWE is shaped by a range of different processes that occur across the spatial scales. Many of the newly introduced features such as *iwest*, *isouth*, *inorth*, *nnMarg*, *TPI100* and *sur-canopy* described in 3.2.5 frequently show up as important features and for some days explain the most variance in the sites (e.g. BKL 2017: *iwest* and TPI100; BKL 2018: *sur-canopy*; KTL 2017: *isouth*, *nnMarg*; KTL 2018: *nnMarg* and watershed-scale: *nnMarg*). Features such as *iwest*, *isouth*, *inorth* and *ieast* although derived from the equation for hillshade, were able to explain, as suspected, the effect of the incident storm events on SWE patterns. It is likely they did not show up as significant on the watershed scale because the direction depends on the pillow location. *TPI100* and *TPI* are shown to be of some importance in explaining the distribution of SWE, especially during frequent accumulation and melt events where the effect of snow loading and melt are high, respectively.

Many studies attribute *canopy* and *aspect* as main spatial predictors involved in snowmelt (Roger C. Bales et al. 2006). This was shown clearly in the spring melt season in Fig. 3.5, but only in second place to *nnMarg*, which was a consistently dominant feature for both water years on the watershed scale. This is in total agreement with the findings of Dominik Schneider and Noah P. Molotch (2016) where he found that the historical product based on the SWE reconstruction model (Rittger et al. 2016), similarly to *nnMarg*, largely improved the physiographically-based regression, explaining more than twice the variance in each of the physiographic features. This is not the case however at the 1 km^2 scale where other features were sometimes more prominent.

Results show clearly that the predictors of the spatial variability of snow differ between the WSN sites, and between the local WSN site and all eight snow pillows scattered across the watershed (Clark et al. 2011; Jost et al. 2007). For the same site however, one can argue

that inter-yearly predictors remain the same to some extent, but the magnitude of their effect differs and is sometimes masked by other features. GRZ's *longitude* and *TPI100* are consistent inter-yearly with *sur-canopy* being more dominant during the wet year.

Many identified features presented in the results adhere well to what was found in Clark et al. (2011), where they conduct a study on previous spatial SWE sampling publications and conclude that the dominant processes for the local-scale (i.e. 1 km^2), consist of the effect of wind, gravity and topography on snow such as drifting and snow loading (*TPI100* and *roughness* related) and snow interception and redistribution by canopy (*sur-canopy*). We add to this the interception of and shading from directional snow storms by topography.

nnMarg is prominent during melt because the historical reanalysis product it is derived from is based on data assimilation of a physical snow model with the high resolution 30 m Landsat fractional snow cover (fsc), and it has been shown that there is a strong relationship between the fsc and SWE in the Sierra Nevada (Rittger et al. 2016). This could explain why the feature underachieved during peak snow season at the local scale where satellite fsc is not as informative as during early accumulation and late melt season when snow cover is patchy.

Both GRZ and KTL's daily "simulated" SWE melt showed a major consistent improvement in the cross correlation with runoff compared to the pillow's. This implies that melt from GRZ and KTL's WSNs would be able to better forecast the outflow of the East Branch and subsequently downstream reservoir inflows. It also suggests that the WSNs' mean melt dynamics are more representative on the East-Branch sub-basin scale compared to the pillow. We should note that the pillow at GRZ is surrounded by canopy which could have relatively deteriorated its spatial representation. However the pillow at KTL is located in an open meadow. For instance, the suspected rain-on-snow event shown by the sharp spike at the start of February 2017 is mostly pronounced at KTL compared to the other sites (Fig. 3.3). In fact, this event caused the flooding from the Oroville Dam overflow that resulted in serious structural and environmental damage, along with liabilities to civil safety (Associated Press 2017; W. Davis and Hurt 2017). Given the available systems, Fig. 3.10b implies that the WSN at KTL is able on average to most accurately predict the EB runoff, and could be used to forecast events such as the Oroville incident few days in advance.

3.5 Conclusion

Data analysis for water years 2017 and 2018 reaffirms that existing automatic point measurement systems (snow pillows) yield biased estimates of the local spatial SWE, with biases that can reach up to 50%. Unlike current systems in operation, WSNs were successful in capturing the spatial variability across the 1 km^2 regions.

Data from the two years show a strong average inter-year consistency in the spatial patterns of SWE both intra-site and inter-site, with the majority of stations and sites preserving their relative rank.

Newly proposed static features that attempt to model regional shading by topography from directional snow storms as well as the dynamic feature that finds the nearest historical Landsat assimilated SWE map have shown to be skillful linear predictors on the local and watershed scales respectively.

Features simulating the topographic shading of directional incident snow storms based on the hillshade equation as well as the down-sampled Topographic Position Index achieved high coefficients of determination (up to 0.8 and 0.9) only locally at two WSN sites.

A linear regression fit shows that the nearest neighbor feature consistently explained up to 90% of the variance in the watershed-scale SWE, which is around 50% more than the next highest variable, a finding corroborated by the literature. We highly encourage the adoption of such dynamic feature in future basin-scale interpolation studies, especially that our data reassert that spatial snow patterns exhibit a strong inter-annual stationarity.

Lagged cross-correlation of snow melt with a downstream flow meter showed a significant improvement of up to 100% for two of the study sites compared to existing systems suggesting that the dense spatio-temporal information added by WSNs is not only crucial for spatial interpolation but also could be instrumental in improving runoff forecasting and water management.

Notwithstanding the importance of the results achieved in the present study, some of its limitations stem from the fact that our analysis is drawn from data at only one basin and just over two water years. With respect to spatiality we suggest drawing further data from airborne LiDAR in representative areas to help further evaluate our findings.

In addition, we propose the following to improve runoff forcasting skills of the present WSN system. First, we recommend that more clusters of WSNs be installed; and/or the wireless communication range of the technology be increased, for instance by moving to sub-1GHz frequency. This would allow greater spatial coverage and improve the ability of the signals to better penetrate dense canopy. Second, we suggest an increase in the use of multi-level watchdog timers and automate contingency plans to help recover from unpredictable failures and allow for better real-time operation. Third, future deployment can benefit from a denser measurement system for research purposes; with slight modification every repeater can itself become a limited-capability sensor node. This would allow for 100s of snow sensors per 1 km2. Fourth, SWE data from WSNs should supplement existing operational stations to develop gridded real-time SWE products at both the sub-basin, basin and regional scales, and to help seamlessly answer the critical question for different stakeholders: "How much water is out there?". Finally, future applications would benefit from the use of WSN dense data in physically-based forecast models and state-aware machine learning algorithms to quantify the forecasting improvement in terms of water and energy budgets in comparison to existing methods. Such applications can incorporate other sensor information such as temperature, humidity, solar radiation and soil moisture that were collected by the presented WSN but were not used in this study.

Chapter 4

Near real-time estimation of high resolution spatial SWE using data blending from scarce in-situ measurements and a historical product

4.1 Introduction

On-the-ground sensors across watersheds in California and across the world lack sufficient coverage to accurately determine spatial snowpack information or other hydrologic inputs and states (**lackOfSens**). However, with the advent and rapid development of accessible cyber-physical systems technology, watershed instrumentation is expected to increase. We find many such systems in the recent literature (Kerkez et al. 2012; Lundquist, Cayan, and Dettinger 2003). The four state-of-the-art Wireless Sensor Networks based measurement systems have been recently deployed in the Feather River watershed to better represent the variability of SWE across the landscape and complement the spatial estimate acquired from existing snow pillows (Sami A. Malek et al. 2017).

Dozier, Bair, and R. E. Davis (2016) outlines the existing methods for spatial SWE estimation: (1) spatial interpolation from in-situ sensors constrained by remote sensing, (2) SWE reconstruction using snow melt models given the point of disappearance of snow determined from remote sensing, (3) global SWE remote sensing based on passive microwave, (4) a snow model assimilated by dense in-situ sensors and (5) emerging methods such as airborne LiDAR altimetry.

SWE reconstruction presented in Rittger et al. (2016) on its own cannot be used in a real-time context because its estimate depends on a future observation of snow disappearance. Remote sensing from NASA such as the Advanced Microwave Scanning Radiometer - EOS

(ASMR-E) and Moderate Resolution Imaging Spectroradiometer (MODIS) (Justice et al. 1998) provide coarse estimates of SWE (16 km x 16 km) and fractional snow cover (500 m x 500 m) respectively, with no information about sub-pixel variability. MODIS fractional snow cover does not provide information about the amount of snow after the pixel is saturated (i.e. totally covered with snow); and when it is useful during the melt phase, it is often subject to canopy induced error (Raleigh et al. 2013). ASMR-E's low resolution makes it not practical not useful for estimating the intra-basin distribution of SWE in complex terrain. On the other hand, in-situ operational sensors provide frequent highly accurate measurements but at low spatial scale. Airborne Light Detection and Ranging (LiDAR) scans combined with snow density values provide SWE estimates at a large spatial scale, but as a stand-alone method are currently expensive to conduct at the needed temporal scale.

Many studies have tried to combine different measurements with a physical snow model to benefit from both the accuracy of the measurements and the temporal resolution and continuity of the model (Stigter et al. 2017; Xu and Shu 2014; Sun, Walker, and Houser 2004; Magnusson et al. 2014). Such methods are typically used with dense in-situ measurements, remote sensing or interpolation from scarce measurements, and require forcing data such as precipitation and temperature.

K. Elder, Rosenthal, and R. Davis (1998) used binary regression trees with features such as elevation, radiation and slope angle to interpolation detailed snow measurements and combined the result with MODIS fractional snow cover scans to compute the SWE volume. The features chosen explained 60-70% of the observed variance of SWE. Note that such a survey was done once and required 12 transects and 10 snow pits field measurements for a basin of roughly 16 km^2.

Dominik Schneider and Noah P. Molotch (2016) used regression with augmented explanatory variables from a historical remote sensing-based SWE reconstruction model to interpolate in real-time in-situ SWE measurements across basins in the mid-west of the US. Results show that not only did the added features largely improve physiographically based regression beyond the physiographic conditions represented by the snow sensor network, but on average it explained more than twice the variance of any one of the physiographic variables. Using an accurate historical product for real-time snow interpolation is thus more desirable than solely interpolating based on physiographic features, especially when available instrumentation is scarce.

To that end, Zheng et al. (2018) exploited the inter-annual consistency in mountain snow distribution shown in Erickson, Williams, and Winstral (2005), Jeffrey S. Deems, Steven R. Fassnacht, and K. J. Elder (2008) and Schirmer et al. (2011) mainly due to snow loading, and used the nearest neighbor technique to find the nearest historical LIDAR-derived SWE scan that best fits current conditions, and then corrected the residuals using the Gaussian Process to predict from physiographic features such as elevation, canopy cover, aspect and slope. Results obtained were promising, however around 30 hypothetically placed sensors were used, which implies a significant investment in additional operational instrumentation. Basins with such high instrumentation are very rare in reality, and thus a need arises to achieve similar performance but using fewer sensors, which would enable near-real-time (NRT) spatial SWE

estimation across wide geographies worldwide. Ideally, if need be for better accuracy, we should aim to supplement existing systems with those that add the most information.

The work described in this article aims to combine the spatial information contained in historical products with realistic scarce in-situ measurements of SWE, in order to generate a near real-time daily SWE spatial product at high spatial resolution. Unlike the majority of previous work described above, the method we propose does not explicitly use any physiographic features to spatially interpolate SWE. It blends various approaches outlined by Dozier, Bair, and R. E. Davis (2016). We use information derived from (2), (3), (4) and (5), depending on the historical product that is selected, to implement (1) using methods derived from data assimilation (4). Section 4.2 presents the statistical Ensemble Optimal Interpolation (EnOI) method we will use, its mathematical formulation and variations. The method and performances of its variations ensemble selection schemes are first compared using simulations conducted on the Feather River Basin using a daily 90-meter resolution SWE product spanning 30 years and the entirety of the Sierra Nevada mountain chain. The proposed method is then compared to prominent methods from the literature using simulations conducted on the Tuolumne River Basin, where bi-weekly 50-meter LiDAR-derived SWE scans have been conducted for the past four years (since 2014). This study seeks to answer the following questions:

1. To what extent does the proposed improve the estimation of daily spatial SWE?
2. Which covariance structure scheme in EnOI better explains spatial patterns of daily SWE?
3. How does the proposed method compare with existing methods from the literature?
4. For the statistical *menoi* variation, is it better to use high-accuracy sparse historical SWE scans or lower-accurate dense ones in the daily SWE estimate?
5. How does the proposed method compare to SNODAS: the current operational SWE product?
6. How to incorporate data from newly deployed sensor networks into the proposed method?

4.2 Materials and Methods

The main scheme of the study consists of assimilating an a priori random field representing the possible spatial SWE distributions with the daily SWE measurements using the Ensemble Optimal Interpolation method (EnOI) described in 4.2.1 .

4.2.1 Ensemble Optimal Interpolation (EnOI)

The adopted EnOI method consists of a Bayesian approach to optimally combine background estimates with measurements. The forward model is not dynamical or physically based, and thus the method can be thought of as more similar to an Ensemble based Gaussian Process (GP). An Ensemble approach is used because due to the high resolution of the SWE maps, the dimension of our system is high making it impractical to handle the covariance matrices required for this method, which would have the size of the square of the number of pixels. After estimating the background SWE map as the mean of the field, a difference between the estimate and the actual observations, often called residuals, will likely remain. Such residuals are re-evaluated to further improve the estimate by updating the background field with observations across the spatial extent. We first define ensemble members $\Psi_i \in \mathbb{R}^n$ (i = 1, ..., N), where N is the ensemble size and n is the dimension of the model state. The ensemble of model states is stored in a matrix A:

$$A = (\Psi_1, \Psi_2, ..., \Psi_N) \in \mathbb{R}^{nxN} \tag{4.1}$$

In our case, A holds all the N historical maps Ψ_i of SWE linearized into columns of length n. n is thus equal to the product of the map's rows and columns. The state-space equations can be written as:

$$x_t = \bar{A} + \epsilon \tag{4.2}$$

Where x_t is the background forecast map field of day t and is completely defined by the selected prior ensemble A with mean $\bar{A}$. d_t is the observation vector made of a collection of SWE sensor measurements at time t. ϵ accounts for the forecast error, assumed to be random normal and is defined by the covariance of the selected ensemble A. The observed states (or pixels) are retrieved from the state space using the following equation:

$$d_t = Hx_t + \gamma \tag{4.3}$$

$H \in \mathbb{R}^{mxn}$ is the measurement operator relating the true model state Ψ_t to the observations d_t and allowing for zero mean normally distributed measurement errors γ. The Ensemble Kalman Filter (EnKF) and EnOI were introduced and used by Evensen (2003) and Burgers, Leeuwen, and Evensen (1998) to efficiently assimilate sensor measurements into non-linear physical models. EnOI is an efficient approximation of the EnKF method and is extensively used in oceanology (Counillon and Bertino 2009; Kaurkin, Ibrayev, and Belyaev 2016a; Fu and Zhu 2011). The ensemble mean of A can be expressed as $\bar{A} = A1_N$ where $1_N \in \mathbb{R}^{NxN}$ is the matrix where each element is equal to $\frac{1}{N}$. We define the ensemble perturbation matrix:

$$A' = A - \bar{A} = A(I - 1_N) \tag{4.4}$$

Given a vector of measurements $d \in \mathbb{R}^m$, where m is the number of measurements, $D \in \mathbb{R}^{mxN}$ is defined to hold the perturbed measurements and $\Upsilon \in \mathbb{R}^{mxN}$ to hold the perturbations only with ensemble mean equal to zero. The measurement error covariance matrix can then be

expressed as: $P_e = \frac{\Upsilon\Upsilon^T}{N-1} \in \mathbb{R}^{mxm}$ Detailed derivation of the Ensemble Kalman Filter analysis equation can be found in Evensen (2009) and can be expressed by both the standard equation in terms of the ensemble covariance matrices:

$$A^a = A + P_e H^T (H P_e H^T + R_e)^{-1}(D - HA) \tag{4.5}$$

or using the ensemble of innovation vectors defined as $D' = D - HA$

$$A^a = A + A'A'^T H^T (HA'A'^T H^T + \Upsilon\Upsilon^T)^{-1} D' \tag{4.6}$$

where $P_e = \frac{A'A'^T}{N-1} \in \mathbb{R}^{nxn}$ is the ensemble covariance matrix. Every model time step, the EnKF integrates N ensemble members in time regardless of the availability of measurements and dynamic covariance of the time-evolving ensemble is used at the analysis step. On the other hand, the EnOI only integrates 1 member $\Psi \in \mathbb{R}^n$ and the analysis is computed in the space spanned by a stationary ensemble denoted A_s of model states as shown in the equation:

$$\Psi^a = \Psi + \alpha A'_s {A'_s}^T H^T (\alpha H A'_s {A'_s}^T H^T + \Upsilon\Upsilon^T)^{-1}(d - H\Psi) \tag{4.7}$$

where a $\alpha \in (0, 1]$ is a parameter giving different weights for the forecast and measurement error covariances. α is used because the variance of a stationary (ie: not changing in time) ensemble over a long period usually overestimates the instantaneous variability. In the subsequent experiments, the parameter α is tuned to minimize the cross validation error at the sensor locations of the day during the test year. The EnOI is thus more computationally efficient than the EnKF but at the cost of slightly lower performance. The forecast model is usually a dynamical model, but in our case, it is simply the mean of the background field. In addition, the forecast model and observations must be unbiased.

Some have used a Multivariate Optimal Interpolation (MVOI) technique where the covariance Pe is modeled by explicit functions (Kaurkin, Ibrayev, and Belyaev 2016a; Kaurkin, Ibrayev, and Belyaev 2016b). However using the model-based covariances of EnOI have more benefits as demonstrated by Kaurkin, Ibrayev, and Belyaev (2016a). The rich data provided by the historical product should provide adequate values for the complex spatial correlations and the anisotropic nature of the snowpack, a task more challenging, if at all possible, to achieve using explicit functions.

Unlike the EnKF, EnOI does not provide an absolute uncertainty estimate for the updated state because of the method of procuring the prior ensemble distribution and the α scaling parameter, however the post-analysis ensemble spread of the field does describe the relative uncertainty between the state pixels. Localization is typically used when the ensemble size is small, to mitigate the effect of spurious correlations appearing between physically non-correlated states (for instance between distant pixels). However, in our case, severe localization will have a potentially detrimental effect since the background estimate's bias is not negligible. Regions with reduced correlations due to localization will retain the background mean estimate after analysis contributing to strong biases in the result. The appropriate way to deal with this issue is to choose a background estimate with low bias.

Moreover, localization becomes an attractive option when the number of sensors become large enough that their field of influence becomes highly superimposed. This is not our case where only scarce measurements are available. Nevertheless a study of the effect of localization is encouraged as future work.

Finally, it is interesting to observe the similitude between EnOI and GP; where GP can be thought of as EnOI with zero background estimate and where the α and localization characteristic length in EnOI are indirectly estimated using optimization methods in GP. Moreover GP supports kernels that could substantially change the state-space covariance structure compared to a simple historical sample covariance used EnOI.

Prior ensemble sampling

We use three different schemes to generate the prior ensemble estimate that describes our prior state as well as the error covariance of that state. In the first scheme, the ensemble consists of all the available historical maps of SWE (except for the test water year). The historical maps of SWE used consist of the 90-meter Landsat-derived reanalysis product in Margulis et al. (2016) and the 50-meter LiDAR-based product in Painter et al. (2016) and are explained in more details in Section 4.2.2. We refer to this scheme by the variable *menoi*. In cases where a dense historical record is used, i.e *menoi*, an eigenvalue-based dimensionality reduction is applied to the ensemble to reduce it to 100 members while retaining the directions of dominant variances. This ensemble is static and does not change throughout the daily simulation.

The use of a static ensemble to represent the error covariance is probably sub-optimal. The covariance structure likely changes in time especially between the accumulation and ablation phases of the snowpack. In the second scheme, the ensemble consists of the collection of historical SWE maps occurring at the same day of each other water year. We name this scheme *menoic*. The Ensemble mean in this scenario consists of the well-known climatologic mean estimate. The ensemble thus changes every day.

In the third scheme, the ensemble consists of the collection of yearly nearest neighbor maps to the measured SWE from the historical record. We name this scheme *menoi_ynn*. This approach should reduce the bias in the prior when sensor locations used in the nearest neighbor procedure are non-biased estimates of the spatial SWE. Note that in all three schemes we employ only data-driven covariances. The *menoic* and *menoi_ynn* schemes use a dynamic ensemble that changes daily, while the *menoi* scheme uses the same static ensemble for all the days of the water year.

4.2.2 Experimental setup

The three different methods outlined above are compared with each other at the Feather River basin. *menoi* is then compared with the feature-selective multivariate regression (a potentially real-time method) *schn* (Dominik Schneider and Noah P. Molotch 2016) and the non-real-time Landsat-derived method *landsat* (Margulis et al. 2016) obtained from the

recent literature, as well as with the operational method SNODAS at the Tuolumne River basin using the LiDAR derived spatial data product in Painter et al. (2016) as reference.

Sensor locations used in the experiments are those of existing snow pillows. The snow-pillow network is maintained by the Department of Water Resources (DWR). These remote in-situ sensors "directly" measure SWE through the weight of snow and transmit the measurements to an online database. They are typically sparsely scattered throughout the basin as shown in Fig. 4.1 and 4.2. Measurements from other systems such as the WSNs can be incorporated into the estimation process by simply appending rows to the measurement operator matrix $\mathbf{H}$ in equation 4.3 that maps the new measurement value appended to vector $\mathbf{d}$ to the state (or pixel number) in the background vector $\mathbf{x}$.

Historical product selection

Feather River basin

For the ensemble selection (representing covariances) for the Feather River basin, we chose a newly developed state-of-the-art snow water equivalent (SWE) Bayesian reanalysis dataset based on the assimilation of remotely sensed fractional snow-covered area data over the Landsat 58 record (Margulis et al. 2016). The reanalysis datasets ranges from 1985 to 2015. The product's spatial and temporal resolutions are 90 m and daily, respectively. It is reported that a comparison with in-situ data showed a mean and root-mean-squared errors (RMSE) less than 3 and 13 cm, respectively (Margulis et al. 2016).

The product covers the entirety of the Sierra Nevada mountain range (Section 4.2.2). The choice of a widely available product allows for convenient experiment replication on all the watersheds in California.

The Feather River basin is chosen because it is situated in the mountain chain and because the NRT spatial maps of SWE would be useful for a more general objective of improving runoff forecasts specifically at Feather River reservoirs as it is the site of newly installed four autonomous snow sensor clusters. Each cluster is operating a mesh network (Watteyne, Doherty, et al. 2013), covering an area of 1 km^2 with 12 sensor stations and approximately 30 relays.

For the EnOI update step, using the entire historical product as ensemble in method *menoi* yields an ensemble size in the order of 10,000. Such a size can be prohibiting to store in memory using ordinary Desktop computers. We thus reduce it to 100 using the method outlined in Evensen (2009): First, the Singular Value Decomposition (SVD) of the ensemble perturbations A' is computed. We then retain only the first N singular values of the decomposition and regenerate a 100-member ensemble to represent the covariance.

Note that such evaluation with a reanalysis product shows the skill in reconstruction but not necessarily the accuracy of the results because no direct sensing data of SWE was used, whether in-situ or spatial. We thus apply the method on Tuolumne where LiDAR data is available.

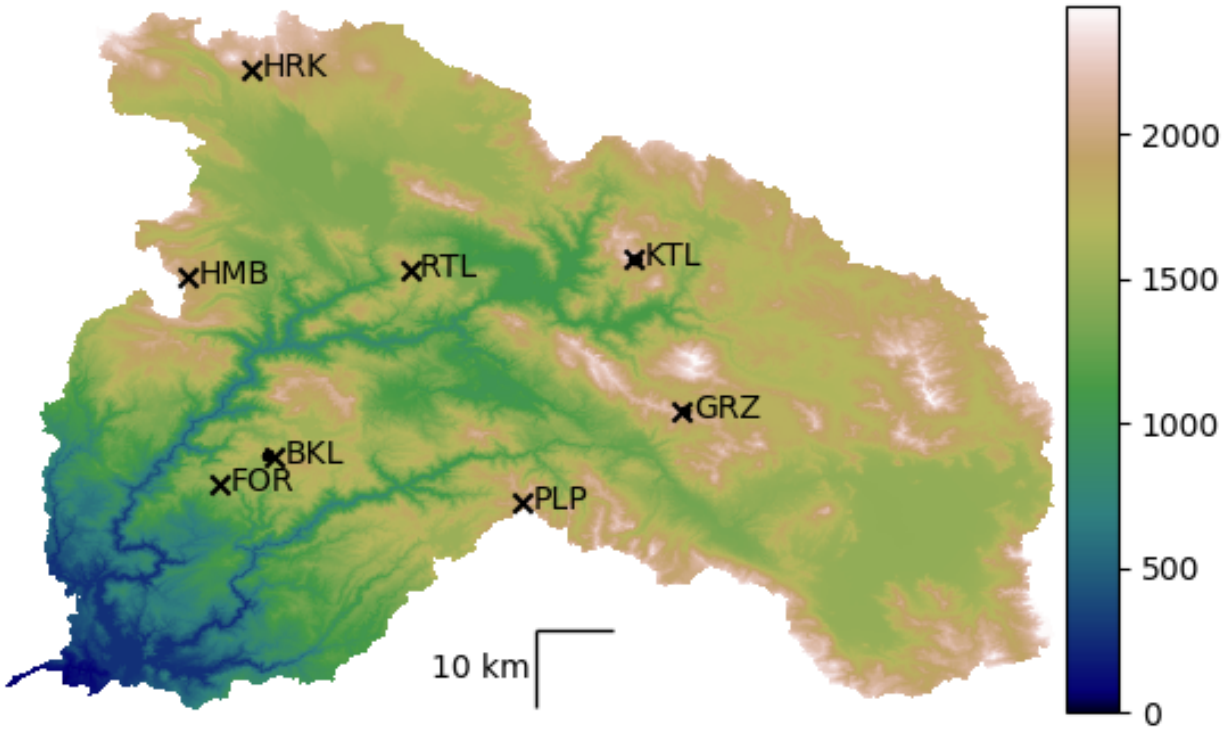

Figure 4.1: Feather River basin sensor locations overlaid on a 90 meter resolution Digital Elevation Model (DEM). Elevation is in meters above sea level. KTL, GRZ and BKL each include a cluster of roughly 12 sensors (Sami A. Malek et al. 2017).

Tuolumne River basin

For Tuolumne River, we use both the product described in Section 4.2.2 above in *menoi_pr* as well as a LiDAR based product (Painter et al. 2016) in *menoi_li* to sample the ensemble from. LiDAR provides rich spatial information (3-m resolution measured snowd-epth and 50-m resolution modeled SWE) and is considered a highly accurate spatial product. NASA's Jet Propulsion Lab in partnership with the California Department of Water Resources has developed the Airborne Snow Observatory; an imaging spectrometer and scanning LiDAR system that measures snow depth at unprecedented basin-wide scale and spatial resolution of 3 m and produces spatial SWE maps at 50-m resolution spanning the Tuolumne and Merced river basins by coupling measured snow depth with the iSNOBAL snow model (Painter et al. 2016). The final product is freely accessible to the research community.

Only four sensor measurements at existing snow pillows locations, shown overlaid on the elevation map in Fig. 4.2, were simulated by extracting their values from the withheld LiDAR test year. Unlike in Section 4.2.2 where the modeled daily SWE maps exist for each day of the test water year, LiDAR derived SWE maps are only available biweekly for the years from 2014 to 2017, and thus we estimate the SWE only for those days. The results

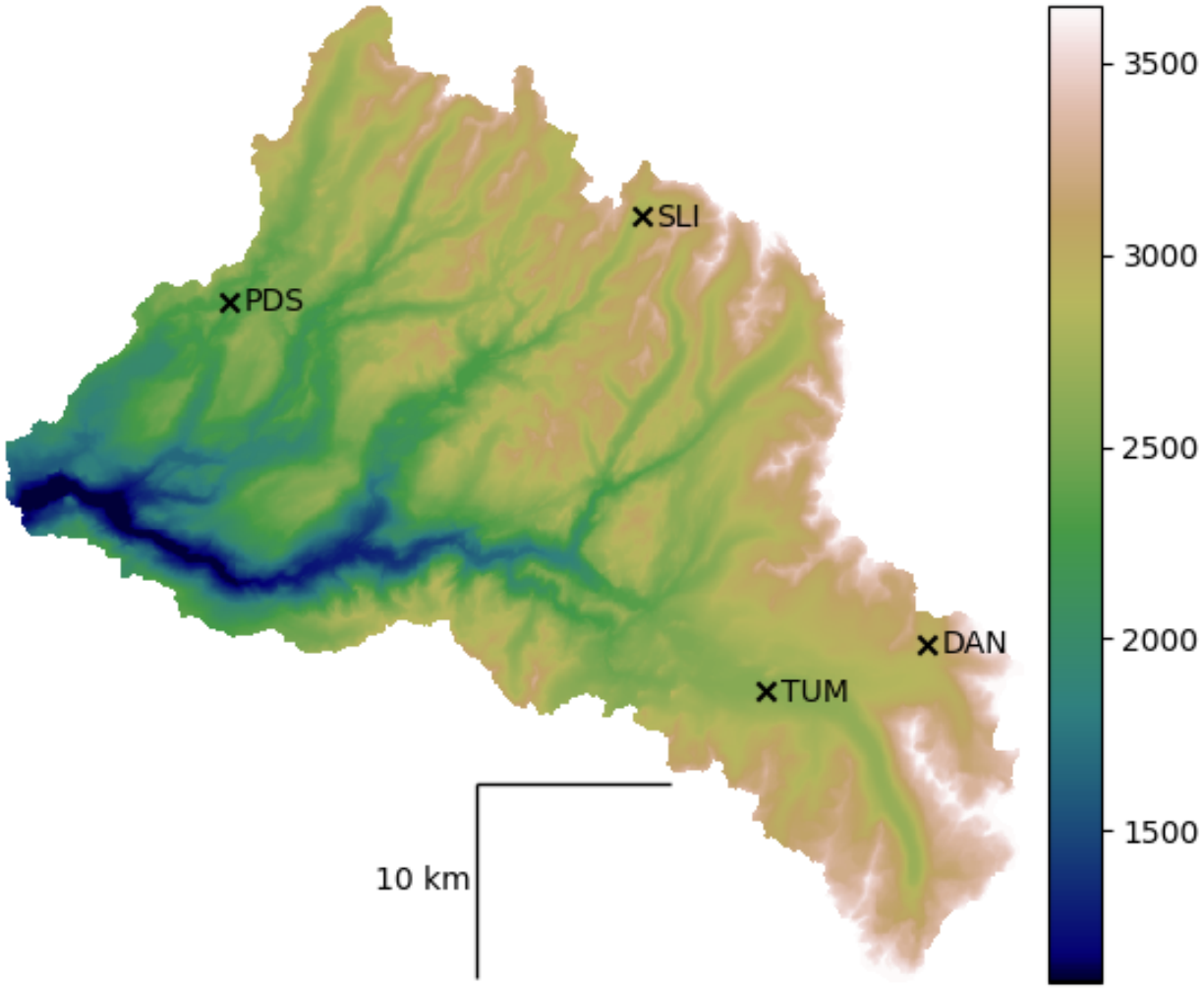

Figure 4.2: Tuolumne basin's 4 snow pillow locations overlaid on a 50 meter resolution DEM. Elevation shown is in meters above sea level.

can demonstrate the potential limit of the method in terms of number of historical scenes available. Results of this experiment can reveal both the reconstruction skill of the proposed methods using both a dense and scarse historical product, and the SWE accuracy of the result compared to LiDAR. We should note however that a modeling error is inevitably introduced when raw LiDAR snow-depth measurements were converted to SWE in Painter et al. (2016).

The real-time product proposed in Dominik Schneider and Noah P. Molotch (2016) and S. R. Fassnacht, Dressler, and R. C. Bales (2003) uses a method that selects the most informative independent variables out of a collection of up to 16 to interpolate SWE measured by a collection of sensors at sparse locations using the multivariate regression. Those independent variables include: elevation, north-western barrier, south-western barrier, distance to

ocean, latitude and closest SWE map from the historical product. The referenced research uses a reconstruction product as historical product, while we will use the LiDAR-derived product instead for the Tuolumne.

The latter product, termed *marg* cannot be generated in realtime as it depends on future satellite observations; nevertheless we also simulate it to compare with LiDAR at Tuolumne.

Finally, after downscaling the SWE maps obtained from using the *menoi_li* and *menoi_pr* methods, we compare them to the operational NRT daily 1 km Snow Data Assimilation System (SNODAS) SWE product (*National Operational Hydrologic Remote Sensing Center. 2004.* 2004) generated by the National Oceanic and Atmospheric Administration (NOAA) as an operational comparison.

Note that for all the experiments, each test water year is excluded from the ensemble selection process and is subsequently used as the "truth".

The different experiments underline the flexibility in dealing with different products and spatio-temporal scales (both 90-m, 50-m and 1 km and daily to bi-weekly) and evaluate whether such method is appropriate and ready to implement operationally.

4.3 Results

Results pertaining to the Feather River and Tuolumne River are presented in Sections 4.3.1 and Section 4.3.2 respectively.

4.3.1 Feather River: from Landsat-derived products

The 32-year simulation-experiment results are shown in Table 4.1. For each year, it shows the error metrics for the peak snow-season day for each ensemble selection method described in Section 4.2.2. The last row that summarizes the findings shows that on average, use of nearest neighbor maps (*menoi_ynn*) exhibits less error than use of all historical SWE maps (*menoic*), which in turn outperforms use of only historical maps for the same day of year (*menoi*), in terms of RMSE, MAE and bias.

However, results also show that no method is error-wise consistently better than the other for that simulation period. The highest errors are seen during dry water years for example 1987 (dry), 2014 and 2015 (critically dry). The minimum achieved MAE is 13%, 22% RMSE (2006-*menoic*) and 0% bias. Figure 4.3 shows the time series evolution of the RMSE as percent of daily spatial mean SWE for each of the methods. The scaled daily spatial mean SWE is also shown in dotted line. The RMSE exhibits a U-shape plot, with RMSEs increasing at the edges of the snow season when the daily spatial mean SWE is low. Similarly to Table 4.1, no method consistently outperforms the other for the three years 1998 (wet), 2002 (dry) and 2016 (average-dry). The *menoi* exhibits a smooth RMSE series, while *menoic* and *menoi_ynn* show a rougher pattern with occasional spikes. On average, *menoi* results in lower RMSE during the peak snow-season for those years, which is corroborated by Table 4.1.

	RMSE, %			MAE, %			Bias, %		
Water year	menoi	menoic	ynn	menoi	menoic	ynn	menoi	menoic	ynn
1985	39	44	36	23	27	21	-19	-23	-11
1986	28	33	28	16	20	15	7	14	3
1987	86	90	73	57	56	46	47	44	34
1988	32	30	30	18	17	17	1	1	-5
1989	36	35	35	21	19	21	1	-13	5
1990	34	45	34	21	28	20	-9	-18	-7
1991	42	52	57	23	29	32	-10	-22	-22
1992	32	34	32	19	20	19	9	9	6
1993	48	50	50	32	33	33	-31	-31	-30
1994	50	53	57	26	29	28	14	16	5
1995	31	30	36	17	18	23	4	8	15
1996	29	26	30	17	15	17	-9	-2	-10
1997	52	53	51	32	33	33	27	27	28
1998	38	38	41	23	22	25	-15	-16	-19
1999	40	39	45	24	21	27	19	16	23
2000	39	44	39	22	27	22	8	14	6
2001	61	57	45	33	36	26	18	24	7
2002	26	25	25	16	14	15	3	0	2
2003	34	37	32	20	22	18	5	-3	-13
2004	28	32	44	16	20	25	2	13	-7
2005	55	47	48	36	31	32	-29	-27	-27
2006	27	28	28	13	14	15	-2	0	5
2007	31	42	47	18	26	27	2	0	0
2008	35	29	40	20	18	25	-6	-8	-18
2009	24	22	33	14	13	20	-5	-2	-10
2010	32	32	30	19	19	18	0	-9	-5
2011	35	37	33	20	22	19	-13	-16	-12
2012	53	51	54	31	27	31	6	2	3
2013	35	43	39	19	23	21	-5	-9	-5
2014	152	129	137	88	50	52	56	24	32
2015	176	138	111	115	84	54	95	68	36
2016	34	44	37	17	23	18	0	8	6
Average	47	47	46	28	27	25	10	9	7 [1]

Table 4.1: Peak snow-season error statistics for each ensemble selection method for water years from 1985 to 2016. For each of *ynn* (*menoi_ynn*), *menoic* and *menoi* the covariance is represented by a sample of yearly nearest neighbor maps, climatologic maps and all maps respectively. (1) The last row, last three columns represent the average of the absolute bias metrics.

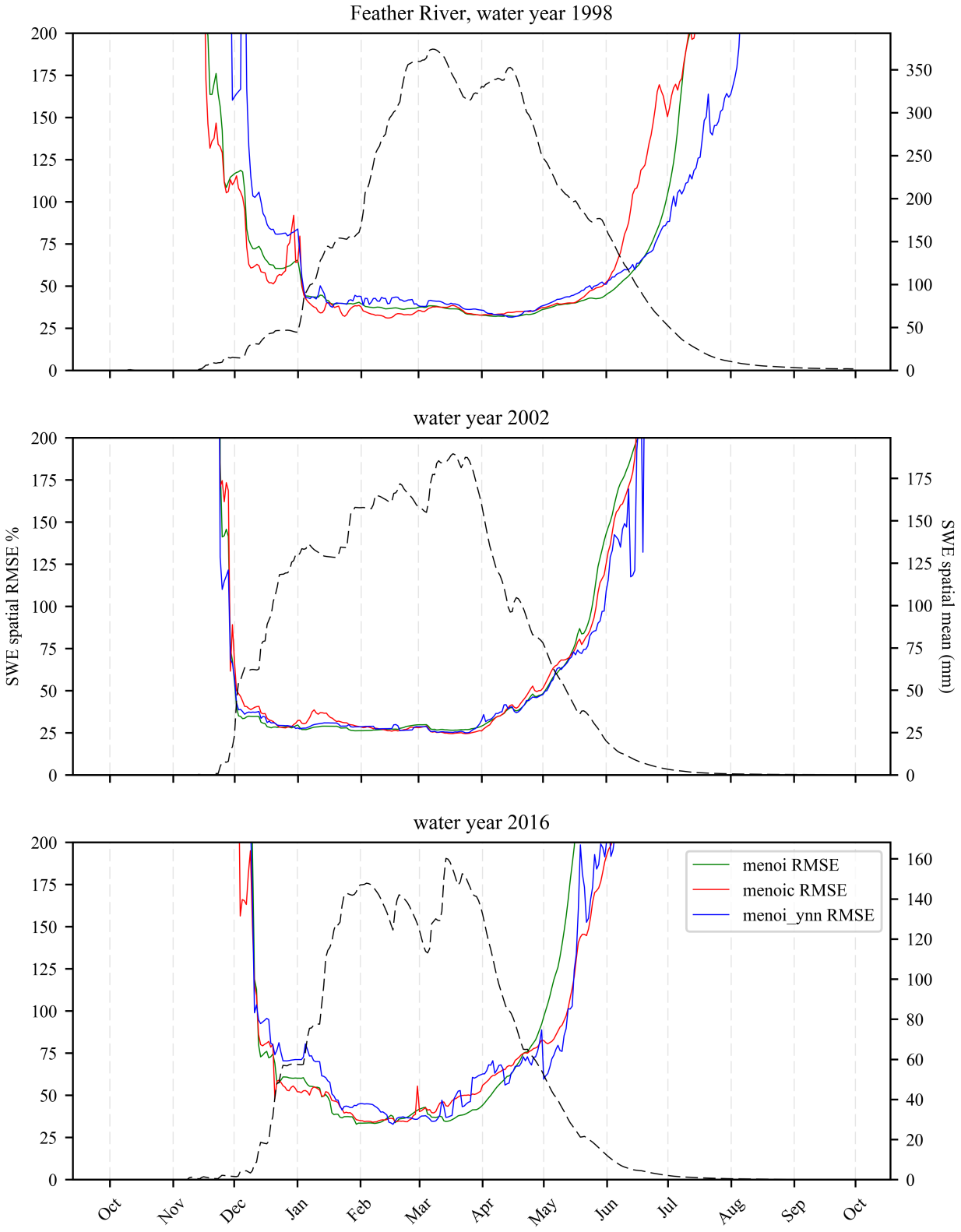

Figure 4.3: Feather River *menoi* RMSE as percentage of the daily spatial mean SWE with different ensemble selection for water-years 1998, 2002 and 2016. For each of *menoi_ynn*, *menoic* and *menoi* the covariance is represented by a sample of yearly nearest neighbor maps, climatologic maps and all maps respectively.

4.3.2 Tuolumne River: from LiDAR & Landsat-derived products

In subsequent figures (Tuolumne), the LiDAR-derived product is the reference for true spatial SWE. This product is only available bi-weekly for the years 2014 to 2017 as evident in Fig. 4.4. Due to the limited number of LiDAR scans, and that the performance of the three methods do not differ substantially, only *menoi* with an ensemble size of approximately 20 is used.

In Fig. 4.4, *menoi_li* extracts the ensemble from the sparse LiDAR-derived product (up to 21 scans) while the *menoi_pr* extracts the ensemble from the Landsat-derived product (total of > 3000 scenes per pixel). The RMSE plots show that on average the *menoi* methods both outperform the feature-selective multivariate regression method *schn*.

For the 2016 average water year, *menoi_li* shows an approximately 25%, 30% and 50% lower in SWE RMSE compared to *marg*, *menoi_pr* and *schn* respectively during the peak snow-season. In the midst of the snowmelt season of the wet water year 2017, both *menoi_li* and *menoi_pr* show a 50% lower in RMSE compared to *schn*. *menoi_li* has a higher RMSE during the early melt season of the dry periods but lower during the later melt season of 2015. *menoi_pr* showed a lower RMSE than the non-NRT *marg* method during the early melt season of the dry year 2014 but not during the end of its snow season, and unlike *menoi_li*, consistently higher RMSE during 2016, compared to *marg*. On average, both *menoi* methods have substantially lower RMSE (up to 80% and 70% during dry and wet years respectively) than the operational SNODAS product.

The heat maps in Fig. 4.5 show a clear higher similarity in the patterns and amount of SWE between *menoi_li* and the true map (LiDAR), compared to the SNODAS map. SNODAS seems to be generally over-estimating SWE across the basin.

4.4 Discussion

The key contribution of this work is that we present a method that can be used to generate real-time high quality SWE maps (90-m and 50-m resolution) using a small number of representative SWE sensors (e.g. Tuolumne only 4 stations were used), which is not possible with traditional regression techniques that necessitate a higher number of sensor stations to adequately fit pre-selected features and observations to models. For instance, the method based on NN and Gaussian Process Regression (GPR) described in Zheng et al. (2018) is a state-of-the-art method that aims to achieve a similar goal as in this paper, however it requires around an order of magnitude more SWE sensors than currently available to adequately find the GPR parameters in order to have a good performance. The work presented here is an attempt to break those constraints, while safeguarding the quality of the result. However, feature-based methods such as Zheng et al. (2018) among many others might better adapt to changing feature conditions. Canopy perturbed by forest fire for instance can be easily accounted for in those methods by updating the vegetation feature. On the other hand, the method presented here would require historical spatial maps of SWE with the new

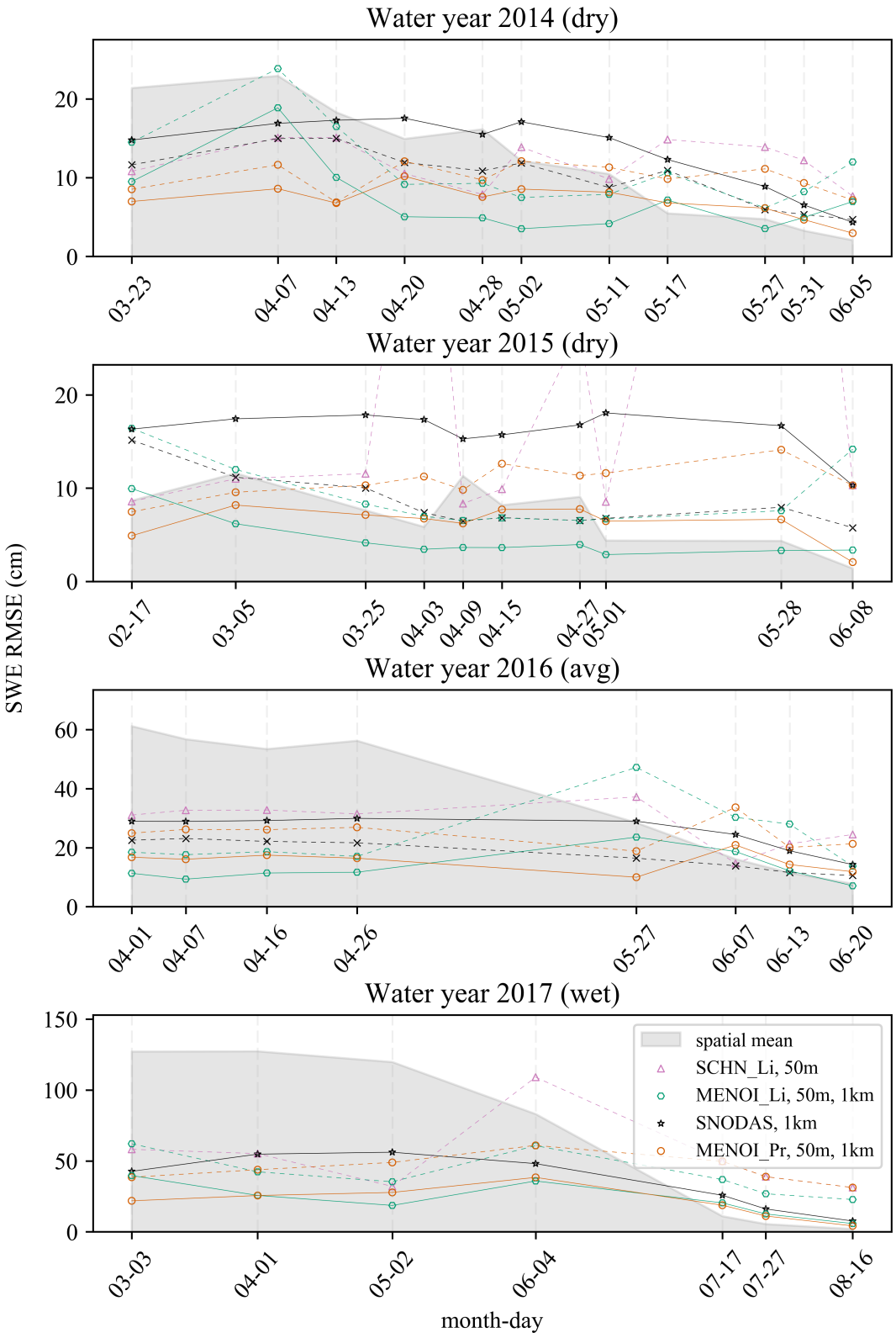

Figure 4.4: Tuolumne basin comparison with existing products. Dashed and solid lines represent products and simulations at 50m and 1km spatial resolution.

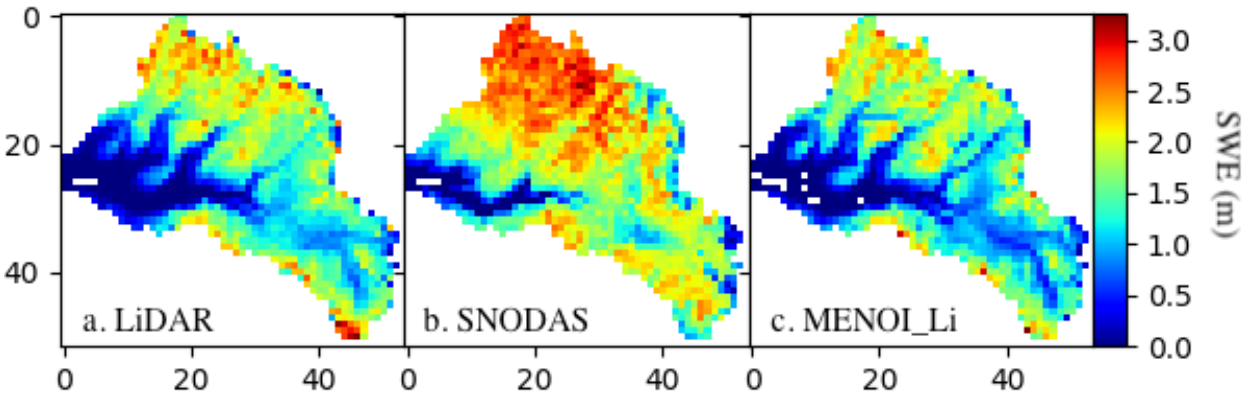

Figure 4.5: Tuolumne's April 1st 2017 1-km resolution spatial distribution of SWE in cm from (a) LiDAR, (b) SNODAS and (c) MENOI_Li. XY coordinates represent the 1-km grid cell number.

reduced canopy. Nevertheless, most features currently used are stationary, e.g. elevation, aspect, northness.

A second contribution is the novel purely data-driven ability to interpolate in-situ SWE observations without the explicit use of physiographic features or satellite observations, but by statistical means through the historical ensemble that incorporates effects of features unknown to the researcher or potentially challenging to measure. For instance, snow loading necessitates wind data that, unlike elevation, are rarely if at all available at the needed resolution or spatial extent. Other features such as differing geographical orientation of mountain ranges also influence snow distribution and can be challenging to model.

4.4.1 Feather River: from Landsat-derived products

As shown in Table 4.1, on average the *menoi_ynn* ensemble selection scheme slightly outperforms the other two (*menoi* and *menoic*) especially in reducing the 31-year average bias (from 28 to 25%) and MAE (from 28 to 25%), and no substantial improvement when it comes to 31-year average RMSE (1% difference). The plots show that the *menoi*, having a stationary ensemble, resulted in the smoothest RMSE series, while the *menoi_ynn* exhibits sudden jumps occasionally due to the changes in the nearest neighbor matched maps.

A synergistic combination of methods could lead to an even superior outcome since no method is consistently better than the other. In some periods, *menoic* had better performance, whereas in other periods *menoi_ynn* was better. Although the *menoi_ynn* improved most metrics, the disadvantages of *menoi_ynn* is that NN scenes could be selected from historical days that are outside the current day snow-season; for instance, when the best matching scene during a summer melt period happens to be a scene from the winter accumulation period of a different year. It is desirable to limit the yearly NN search window to a few months from the current simulation/estimation day to address this potential disadvantage,

and benefit from a more appropriate climatic covariance structure.

Moreover it could be attractive to prune or replace scenes (NN of years with low matching score) from the ensemble with the objective of reducing the background ensemble bias as much as possible without too adversely affecting the covariance structure or the ensemble size (to avoid spurious correlations). The *menoic*'s main disadvantage is that the snow season timings are not inter-yearly constant on the daily scale. Dry years are often shorter than wet years and the dates of onset and disappearance of snow vary. Therefore it constitutes a more biased background field in non-average scenarios. Note that our current estimation methodology is stateless. It would be interesting to add a state to the simulation where the evolution of the state (SWE) and not the state itself is estimated based on *menoi_ynn* with ensemble sampling strategy based on phase (accumulation and ablation) and amount of snow dynamics.

Also evident in Table 4.1 is that errors as low as 22% (RMSE of 2009) and 13% (MAE of 2009) and 0 biases can be achieved. Those well-performing scenarios typically occur when the biases of the estimates are low. During dry years and at the end of the snow-melt season, real-time remote sensing information becomes crucial for accuracy, especially when the majority of sensors are outside the remaining high-elevation snow cover. Given the scarcity of the sensor network used, this could explain the high errors reported during such situations, shown by the U shaped error curves of Fig. 4.3. This error pattern is also found in most of the literature employing interpolation methods (S. R. Fassnacht, Dressler, and R. C. Bales 2003). However, we should note that using near-real-time satellite information of snow cover from MODIS is needed to significantly improve the snow melt season error as demonstrated in D. Schneider, N. P. Molotch, and J. S. Deems (2017). This concern could also be addressed by strategically adding sensors.

4.4.2 Tuolumne River: from LiDAR & Landsat-derived products

Comparison with the 50-m biweekly LiDAR-derived products showed that, on average, the LiDAR-derived *menoi* outperformed other methods during the peak snow-season. During those periods it is better to use LiDAR for ensemble selection in the *menoi* method instead of the Landsat-derived product. This is mostly evident during water year 2016, where it even outperformed the landsat-derived product from Margulis et al. (2016). Note that the latter product cannot be generated in real-time since it uses Landsat information from the future during the reanalysis. However the statistical advantage of sampling from an extensive historical product could be highlighted during the few days where *menoi_pr* outperformed *menoi_li* even during the peak snow-season of the wet year 2017.

The Landsat-derived *menoi* outperformed the selective-regression method from Dominik Schneider and Noah P. Molotch (2016) during the majority of the peak snow periods across all simulation years as shown in Fig. 4.4. It only outperformed the non-real-time landsat-prod during the dry 2014 water year but not the 2016 wet water year (Fig. 4.4). Given that the product used in *menoi-pr* is Landsat derived, it explains why it would have better

performance during dry seasons since Landsat snowcover does not report SWE information but snowcover and thus is mostly useful during the patchy snow cover of dry/melt seasons.

On average, both *menoi-li* and *menoi-pr* greatly outperformed SNODAS as shown in Fig. 4.4, (04-07-2014 exception that warrants further investigation) with improvements up to 64% and 55% respectively on 05-02-2017, with *menoi-li* outperforming *menoi-pr* in peak-snow periods.

Moreover, the *menoi-li* method resulted in 2016 water year RMSE errors (ex: 14-15 cm from 04-01-2016 to 04-26-2016) are similar to those obtained in Zheng et al. (2018) from the interpolation of SWE across the same region, but using 22 measurements with GPR instead of 4 with *menoi*, which implies that the added information from the historical LiDAR product was able to mitigate the information loss of reducing the sensors from 22 to 4, and further reinforces prior findings that SWE exhibits strong inter-annual spatial patterns.

The plots comparing RMSEs with SNODAS (Fig. 4.4) show significant error differences which highlight the importance of the airborne and ground measurement systems in estimating spatial SWE.

In summary, results imply that the proposed method could have a high beneficial impact in the spatial interpolation of SWE whenever historical highly accurate data (such as LiDAR) is available and only few measurements are available (Fig. 4.4).

4.5 Conclusions

We have thus presented and evaluated a scheme that proved to be beneficial for real-time estimation of high resolution spatial SWE across a mountainous basin with austere surface sensing infrastructure. The data-driven scheme was able to interpolate SWE in real-time from ultra-low density observations and could achieve a minimum RMSE of 22% at 90 m resolution (Feather) and 30% at 50 m resolution (Tuolumne) of the peak snow-season spatial SWE mean, on average outperforming regression methods from the literature that can become unstable with few measurements.

It has been found that both the LIDAR-derived product and the Landsat-derived historical product constitute good background fields to estimate the real-time SWE maps with the former performing slightly better during peak snow conditions. The gap in performance is however expected to increase as the number of sensor clusters instrumenting the basin increases as the accuracy of the covariance becomes more influential. Constructing the ensemble representing the co-variance from yearly nearest neighbor SWE maps results in lower prediction bias compared to selecting all SWE maps or a climatologic sample.

Furthermore, experiments at Tuolumne Basin showed that with only 4 sensing locations, we were able to achieve a higher quality real-time product compared to SNODAS reaching up to a 55% (wet and average year) and 80% (dry year) reduction in error using LiDAR as reference.

Finally, a big advantage in spatial SWE interpolation of the method we present, is that different methods of measurements of SWE that need not be spatio-temporally complete

(ex: asynchronous and with data gaps) can be easily incorporated, including in-situ, sensor-networks, transect measurements and remote-sensing by simply manipulating the observation matrix H.

Though such a method relies on a historical dataset, the need for a dense and extensive measurement systems that covers large portions of the watershed and potentially complex modeling using physiographic features are mitigated. Only few sensor clusters at key locations and with a representative estimate of their surrounding resolution are needed. It thus provides a convenient data-driven approach to spatially interpolate IoT devices' measurements. Related future work of interest would be to formulate a method to identify such sensor placements with maximum information gain adapted for large dimensions and find the number of sensors needed to achieve a pre-specified error tolerance. The work presented here represents an important contribution given that no previous study tackles real-time spatial SWE estimation with such scarcity of measurements and high spatial resolution. Moreover, we have validated previous studies where historical SWE maps were found to provide important information for estimating SWE in real time.

4.6 Algorithms and datasets reference

- Landsat-derived historical product (90-m SWE): https://ucla.app.box.com/v/SWE-REANALYSIS/folder/17206944857
- Lidar-derived historical product (50-m SWE): https://aso.jpl.nasa.gov/
- SNODAS (1-km SWE): https://nsidc.org/data/G02158
- Sensor locations from CDEC: https://cdec.water.ca.gov/
- EnOI analysis algorithm code: https://enkf.nersc.no/Code/Analysis/

Chapter 5

Thesis conclusions and future work

We highlight in this section the conclusions of the research underlying this dissertation and propose tasks to undertake in future work and development. Our results show significant improvement of WSN-based system operations, better understanding of physiographic features affecting spatial SWE estimation, more accurate runoff forecasts, and innovative methods for basin-scale extrapolation. More work and research is needed to refine the reliability of the WSN system and the extrapolation methods, in addition to developing a system that provides real-time daily runoff forecasting.

5.1 Thesis conclusions

The previous chapters demonstrated how system-level improvement of alpine Wireless Sensor Network monitoring instrumentation provided unique information at unprecedented spatio-temporal scales. This shows improved potential of streamflow forecasting crucial for water management applications, and provides dense and reliable real-time data to extrapolate into uninstrumented regions at the basin scale, when the information is blended with remote sensing-derived historical products.

WSN-based snow monitoring system

- The presented end-to-end SOL software suite was adequate for collecting dense hydrologic measurements from physiographically representative locations in real-time. The deployment phase is informed by real-time RSSI and PDR input to optimize node placement efficiency that prevents network collapse displaying real-time data, network performance, and logs maintenance activity in charts and interactive maps.
- The proven and truly off-the-shelf SmartMeshIP wireless technology of low complexity and cost that is at the core of the WSN main components is able to cover multi-km^2 deployment areas. It runs an ultra low-power, highly dense and fully bi-directional communication operations, with wire-like reliability and built-in diagnostics that is responsive to over-the-air reprogramming.

- Partly thanks to the sensor node firmware I developed specifically for this study, the system ensures high integrity of the data even with low power operation. This allows for several months of sensor node operation without the need for solar power, for multiple redundancy provisions, and for transmission efficiency by encapsulating a collection of various sensor readings into the same MTTLV frame. Moreover, multi-level replication and recovery added to the datalogger-level ensured that sensor data unable to be forwarded instantaneously are not lost but saved and later re-transmitted through the restored wireless paths, thus guarantying the integrity of the full snow season data.

- In addition, modifications to the sensor and repeater node firmwares reduced their operating power consumption to a couple of milliamps and microamps on average respectively, which proved to be crucial to the resilience of the network, especially during the harsh winter weather season of 2017.

- After shielding protruding sensor wires from wildlife with rugged materials, data received in real-time and recovered from the sensor nodes internal storage proved that the design met the demands of harsh, remote, and wildlife conditions by addressing the majority of tractable challenges posed by such environments.

WSN data analysis and insights

- WSN data show considerable spatial variability of snow depth, even within a 1 km^2 cluster location. Compared with existing snow monitoring systems, these WSNs, equipped with multiple sensor types, can better detect precipitation timing and phase, including rain-on-snow events, and intense snowfall, monitor sub-daily dynamics of infiltration and surface runoff during precipitation or snow melt, and inform hydro power managers about actual ablation and end-of-season date across the landscape.

- Spatio-temporally-dense measurements from the WSN-based clusters are physiographically representative, sensitive to effects of topography, vegetation, and geology on snowfall, snowmelt, and soil infiltration. Data from the clusters instrumenting the North Fork of the Feather River during a wet and dry water year, 2017 and 2018 respectively, successfully captured the spatial variability of SWE across the 1 km^2 regions. Data show that that existing operational autonomous systems are non-representative spatially, with biases that can reach up to 50%.

- Snow exhibits strong inter-yearly similarity in spatial patterns that is preserved throughout the snow season. A comparison between a wet and dry year showed that the majority of stations and sites maintained strong average inter-year consistency of spatial SWE patterns and preserved their relative rank of SWE estimates.

- No one physiographic feature is consistently dominant in explaining the variation of snow across the 1 km^2 region, neither spatially nor temporally across the complete water year. Temporally dense analysis using Elastic Net regression shows that dominant

features at the sub-km^2 scale are site-dependent and differ from those at the watershed scale.

- Incident storm directions have significant effect on the spatial distribution of new snow at some sites. Newly proposed static and dynamic features were skillful linear predictors of SWE distribution on the local and watershed scales. Locally, simulations of topographic shading of directional incident storms achieved coefficients of determination values as high as 0.8 to 0.9.

- On the basin-scale, historical spatial patterns of snow best predict current ones, but not necessarily during the same water year days. The nearest neighbor feature that consists of the historical map best matching current sensor data consistently explained up to 90% of the SWE variance, 50% higher than other best-performing physiographic features.

- WSNs can be instrumental in improving runoff forecasting and water management as they significantly outperform existing snow pillows. At two WSN sites (KTL and GRZ) at the East Branch of the North Fork branch of the Feather River, lagged cross-correlation of snowmelt with stream flow measurements showed a significant improvement of up to 100% compared to existing systems.

Blending sensor data with remote-sensing-derived historical products

- Notwithstanding the WSN contributions in Chapter 2, the scarce number of local WSNs poses some questions relative to the target interpolation necessary to produce representative real-time daily SWE maps at the basin-wide scale. However, updating fields of Landsat and LiDAR-derived historical products with in-situ measurements at actual locations using EnOI, suggests that data from parsimonious WSNs can significantly improve basin-scale interpolation results.

- Blending ground measurements (ex: WSNs, snowpillows) with remote-sensing-derived products at California's Feather River basin using EnOI, we generate 30-year daily SWE simulations at 90 meter resolution. Pixel covariance is derived from the historical Landsat-assimilated product with different sampling schemes. Results show slightly varying performances with a minimum peak snow season RMSE of 22%.

- Constructing the EnOI ensemble representing the covariance from yearly nearest neighbor SWE maps results in a lower estimation bias compared to selecting all SWE maps or a climatologic sample. However, the latter two result in smoother SWE maps time series.

- Evaluatuing the scheme on California's Tuolumne River basin by generating a 4-year bi-weekly SWE simulations at 50 meter resolution, using a LiDAR-based product as the historical dataset to determine the covariance, resulted in a minimum RMSE of 30%

that is comparable to previous studies where many more sensors were used. Compared with SNODAS, reduction in error is up to 55% and 80%, with LiDAR as reference.

5.2 Future work

Findings from this work open doors for future research and development. We propose that future work assume the following main tasks. First, it would prove beneficial to further refine the reliability of the WSN at specific junctures of the system. Second, increasing the number of strategically installed WSN clusters in the basin and refinements of the proposed SWE extrapolation methods would contribute to reducing the basin-wide estimation error to an achievable minimum. Finally, developing a system that feeds and integrates SWE products, along with other measurements, into a runoff model would provide for real-time daily streamflow forecasting.

5.2.1 WSN-based monitoring systems

As WSNs are becoming a reliable alternative to traditional methods of hydrologic monitoring, it becomes expedient to improve the ease of deployment and operational robustness of such systems for operational hydrology beyond academic research.

There are a few measures that will lead to the simplification of the WSN deployment. At the design level, we propose the development of automatic techniques that would identify locations of repeater nodes for optimal connectivity to reduce trial-and-error during the deployment process. When this is not possible, one should maximize the number of line-of-sights between nodes. As for improving the WSN's operational lifetime, the placement should reflect a topology that is denser near the manager (destination of all measurements) and that thins out with increasing distance away from it. On the other hand, new technologies are emerging where the WSN nodes use a lower frequency in communications allowing for an extended wireless range and and better canopy penetration, greatly facilitating deployment and WSN's spatial coverage.

Furthermore, a procedure for intensive in-lab testing and diagnostic in easily accessible environments with conditions similar to the site locations targeted for deployment should be devised to capture software bugs, design flaws, power issues, faulty sensors and equipment before installation.

Concerning the potential improvements that will make the presented WSN-based remote autonomous measurement system operationally more robust and competitive, it is crucial for the system to adopt a hierarchy of criticalities, whereby system components with the greatest potential impact on the overall monitoring operation in case of failure are given highest maintenance priority and recovery capabilities.

Operationally, the WSN-based system could well benefit from upgrading the health monitoring process by developing a state-aware module that generates notification of failure events along the defined hierarchy of criticalities to reduce the substantial effort of debug-

ging various failures, reducing the network formation and self-healing speed at the firmware level to maximize power efficiency, and improving remote reprogramming capabilities of the various nodes for increased flexibility that is crucial for remote systems, increasing the use of multi-level watchdog timers towards automating contingency plans to help recover from unpredictable failures and allow for better real-time operation.

5.2.2 SWE interpolation and runoff estimation

With the prospect of estimating basin-scale spatial SWE distribution, the current relatively scarce WSN instrumentation constitutes one limitation of the present hydrologic study. We suggest the following to improve SWE estimates and potential runoff forecasts.

Additional WSN clusters need to be strategically installed for a better basin-wide SWE estimate accross the Sierra Nevada mountains. Alternatively, increased inter-node wireless communication range with higher canopy/foliage penetration could mitigate the scarcity of clusters per basin by covering larger spans of basin territory, and subsequently increase the sensors cluster field of influence given the potentially inherently long-ranged inter-pixel correlations of snowpack. However the increase in extreme weather conditions and the advent of new weather patterns could make the latter more advantageous.

To further improve the basin-scale estimation of SWE, it is desirable to include the close-by sensor stations that are outside the basin delineation. This can be done by simply including the additional pixels in both the ensemble representing the covariance (thus increasing the system states by n) as well as in the H, R matrices and observation vector described in Chapter 4.

Moreover, it seems beneficial to formulate a method to identify such sensor placements with maximum information gain given an appropriate covariance structure, and find the number of sensors needed to achieve a desired spatial estimate error tolerance. Such method needs to be adapted for large dimensions to be applicable to sub-100 meter spatial resolution.

Adding distance-based localization to the EnOI method could improve the spatial estimation of SWE. Localization would reduce spurious correlations between distance pixels that were caused by the small sample size of the ensemble. This assumes a spatial locality of the natural processes governing snow distribution, and that had we had the infinite ensemble representing the true covariance, the covariance would exhibit inter-pixel correlations that on average decrease with inter-pixel distances. Moreover, the use of localization is favorable especially when extreme weather conditions are becoming more prevalent, introducing new pattern variations on the larger sub-basin scale.

In the experiments conducted in Chapter 4, we separately used a Landsat-derived and LiDAR-derived historical product to characterise the covariance. An attractive option is to use a synergistic blend of different historical products together including those obtained from reconstruction techniques. Starting from the date of snow disappearance and using the energy balance to reconstruct backwards in time the temporal series of SWE up to the peak snow season, reconstruction products could have a better correlation structure for deep snow pixels. Nevertheless, we think that LiDAR scans remain the most encompassing and

richest spatial information of SWE. We thus recommend to have at least one LiDAR scan per year during peak snow season going forward in time to have sufficient scenes to use for representing the covariance of the quantitative interpolation method with most accuracy.

Given that the Landsat-derived product used in this thesis (and similarly the reconstruction-based ones) as well as snow pillows (few per basins) and WSNs (few in very few basins) are available across the entirety of the Sierra Nevada Mountain range, the work in Chapter 4 can, with little additional effort, culminate in a near-real time daily high spatial resolution maps of SWE for all basins in California with a single analysis step per day. For a 1 km^2 resolution product, this operation should be feasible to run even with the limited computational power of a present personal computer, but would need additional memory requirements for sub-100 m^2 resolutions. Nevertheless, it is most desirable to use near-optimal sensor placement techniques to complement existing ground sensors with new WSN clusters, hence minimizing the product's estimation errors.

We should note that the presented method, given the ensemble sampling approach, estimates SWE day by day and is oblivious of previous day estimates and sensor measurements. One can extend interpolation into the temporal dimension, especially given that snow processes naturally exhibit strong temporal correlations on the daily scale. For instance, this can be done by augmenting the system states to include n measurements of the past n days (and subsequently the ensemble) that get updated in addition to the usual current day measurements. On a similar note, one could use a state-aware forward model. For every time step, a noise field with covariance structure derived from the historical products is added to the previous state and the resulting state is subsequently updated by current available measurements. This should result in a temporally smoother spatial product with gap-filling capabilities that are instrumental in our application where measurements are occasionally missing or unreliable.

We hope that research presented in this dissertation as well as our future work directions will help to guide towards the goal of seamlessly answering the critical question for different stakeholders: "How much water is out there?" Finally, SWE maps produced can be ingested in real-time using data assimilation methods into precipitation-runoff models and the improvement observed in predicted runoff, hydro-power and water management efficiency and economic gain should be evaluated and quantified. Given the WSN lagged-correlation advantage presented in Chapter 3, one could also adopt a purely data-driven approach and use the sensor clusters directly for runoff forecasting, by feeding the dense WSN data or WSN-derived spatial SWE product into state-aware machine learning algorithms.

Bibliography

Associated Press (2017).
"Oroville Dam Spillway Repair Costs to Top $500M, Doubling Initial Estimate". In: URL: https://www.nbclosangeles.com/news/california/Oroville-Dam-Repair-Costs-California-Flood-Storm-451903223.html (visited on 10/30/2017).

Avanzi, Francesco et al. (2014). "A Processing-Modeling Routine to use SNOTEL Hourly Data in Snowpack Dynamic Models". In: *Advances in Water Resources* 73, pp. 16–29. DOI: 10.1016/j.advwatres.2014.06.011.
URL: https://doi.org/10.1016/j.advwatres.2014.06.011.

Bales, Roger C. et al. (2006). "Mountain Hydrology of the Western United States". In: *Water Resources Research* 42.8. DOI: 10.1029/2005WR004387.
URL: http://dx.doi.org/10.1029/2005WR004387.

Baraka, K. et al. (2013). "Low Cost Arduino/Android-Based Energy-Efficient Home Automation System with Smart Task Scheduling". In: *2013 Fifth International Conference on Computational Intelligence, Communication Systems and Networks*, pp. 296–301. DOI: 10.1109/CICSYN.2013.47.

Barnett, T.P., J.C. Adam, and D.P. Lettenmaier (2005). "Potential Impacts of a Warming Climate on Water Availability in Snow-dominated Regions".
In: *Nature* 438, pp. 303–309. DOI: 10.1038/nature04141.
URL: http://dx.doi.org/10.1038/nature04141.

Bavera, D et al. (2014). "A Comparison Between Two Statistical and a Physically-based Model in Snow Water Equivalent Mapping".
In: *Advances in Water Resources* 63, pp. 167–178. ISSN: 0309-1708.
DOI: 10.1016/j.advwatres.2013.11.011.
URL: http://dx.doi.org/10.1016/j.advwatres.2013.11.011.

Bray, Tim (2014). *The JavaScript Object Notation (JSON) Data Interchange Format*. Tech. rep. RFC7159. IETF. URL: https://tools.ietf.org/html/rfc7159.

Brun-Laguna, Keoma et al. (2016).
"SOL: An End-to-end Solution for Real-world Remote Monitoring Systems".
In: *Personal, Indoor, and Mobile Radio Communications (PIMRC), 2016 IEEE 27th*

Annual International Symposium on. IEEE, pp. 1–6.
DOI: 10.1109/PIMRC.2016.7794864.
URL: https://doi.org/10.1109/PIMRC.2016.7794864.

Bühler, Y. et al. (2016). "Mapping Snow Depth in Alpine Terrain with Unmanned Aerial Systems (UASs): Potential and Limitations". In: *The Cryosphere* 10.3, pp. 1075–1088.
DOI: 10.5194/tc-10-1075-2016.
URL: http://www.the-cryosphere.net/10/1075/2016/.

Burgers, Gerrit, Peter Jan van Leeuwen, and Geir Evensen (1998).
"Analysis Scheme in the Ensemble Kalman Filter".
In: *Monthly Weather Review* 126.6, pp. 1719–1724.
DOI: 10.1175/1520-0493(1998)126<1719:ASITEK>2.0.CO;2.
eprint: https://doi.org/10.1175/1520-0493(1998)126<1719:ASITEK>2.0.CO;2.
URL: https://doi.org/10.1175/1520-0493(1998)126%3C1719:ASITEK%3E2.0.CO;2.

California Department of Water Resources (2017). "Climate Change". In:
URL: http://www.water.ca.gov/climatechange/ (visited on 10/24/2017).

Clark, Martyn P. et al. (2011). "Representing spatial variability of snow water equivalent in hydrologic and land-surface models: A review". In: *Water Resources Research* 47.7.
DOI: 10.1029/2011WR010745. eprint:
https://agupubs.onlinelibrary.wiley.com/doi/pdf/10.1029/2011WR010745.
URL: https://agupubs.onlinelibrary.wiley.com/doi/abs/10.1029/2011WR010745.

Commission, California Energy (2017). "Total System Electric Generation, 2013-2015". In:
URL: %5Curl%7Bhttp://www.energy.ca.gov/almanac/electricity%5C_data/%7D
(visited on 10/24/2017).

Counillon, Francois and Laurent Bertino (2009).
"Ensemble Optimal Interpolation: multivariate properties in the Gulf of Mexico".
In: *Tellus A* 61.2, pp. 296–308. DOI: 10.1111/j.1600-0870.2008.00383.x. eprint:
https://onlinelibrary.wiley.com/doi/pdf/10.1111/j.1600-0870.2008.00383.x.
URL:
https://onlinelibrary.wiley.com/doi/abs/10.1111/j.1600-0870.2008.00383.x.

Daponte, P. et al. (2018). "A Survey of Measurement Applications Based on IoT".
In: *2018 Workshop on Metrology for Industry 4.0 and IoT*, pp. 1–6.
DOI: 10.1109/METROI4.2018.8428335.

Davis, Wynne and Alyson Hurt (2017).
Oroville Dam Reached Capacity Faster Than Previous 16 Years.
URL: https://www.npr.org/2017/02/17/515597969/oroville-dam-reached-capacity-faster-than-previous-16-years.

De Michele, Carlo et al. (2016). "Using a Fixed-wing UAS to Map Snow Depth Distribution: an Evaluation at Peak Accumulation".
In: *The Cryosphere* 10.2, pp. 511–522. DOI: 10.5194/tc-10-511-2016.
URL: http://www.the-cryosphere.net/10/511/2016/.

Deems, Jeffrey S., Steven R. Fassnacht, and Kelly J. Elder (2008). "Interannual Consistency in Fractal Snow Depth Patterns at Two Colorado Mountain Sites".
In: *Journal of Hydrometeorology* 9.5, pp. 977–988. DOI: 10.1175/2008JHM901.1.
eprint: https://doi.org/10.1175/2008JHM901.1.
URL: https://doi.org/10.1175/2008JHM901.1.

Department of Water Resources California Data Exchange Center (n.d.).
https://cdec.water.ca.gov. Accessed: 2018-01-20.

Dietz, Andreas Juergen et al. (2012).
"Remote Sensing of Snow - a Review of Available Methods".
In: *International Journal of Remote Sensing* 33.13, pp. 4094–4134.
DOI: 10.1080/01431161.2011.640964.
URL: http://dx.doi.org/10.1080/01431161.2011.640964.

Dozier, Jeff, Edward H. Bair, and Robert E. Davis (2016).
"Estimating the spatial distribution of snow water equivalent in the world's mountains".
In: *Wiley Interdisciplinary Reviews: Water* 3.3, pp. 461–474. ISSN: 20491948.
DOI: 10.1002/wat2.1140.

Elder, Kelly, Don Cline, et al. (2009). "NASA Cold Land Processes Experiment (CLPX 2002/03): Field Measurements of Snowpack Properties and Soil Moisture".
In: *Journal of Hydrometeorology* 10.1, pp. 320–329. DOI: 10.1175/2008JHM877.1.
URL: https://doi.org/10.1175/2008JHM877.1.

Elder, Kelly, Walter Rosenthal, and Robert Davis (1998). "Estimating the spatial distribution of snow water equivalence in a montane watershed". In: 12.

Erickson, Tyler A., Mark W. Williams, and Adam Winstral (2005).
"Persistence of topographic controls on the spatial distribution of snow in rugged mountain terrain, Colorado, United States". In: *Water Resources Research* 41.4.
DOI: 10.1029/2003WR002973. eprint:
https://agupubs.onlinelibrary.wiley.com/doi/pdf/10.1029/2003WR002973.
URL: https://agupubs.onlinelibrary.wiley.com/doi/abs/10.1029/2003WR002973.

Evensen, Geir (2003).
"The Ensemble Kalman Filter: theoretical formulation and practical implementation".
In: *Ocean Dynamics* 53.4, pp. 343–367. ISSN: 1616-7228.
DOI: 10.1007/s10236-003-0036-9.
URL: https://doi.org/10.1007/s10236-003-0036-9.

Evensen, Geir (2009). *Data Assimilation. The Ensemble Kalman Filter*. Springer-Verlag Berlin Heidelberg.

Fassnacht, S. R., K. A. Dressler, and R. C. Bales (2003). "Snow water equivalent interpolation for the Colorado River Basin from snow telemetry (SNOTEL) data". In: *Water Resources Research* 39.8. ISSN: 00431397. DOI: 10.1029/2002WR001512.

Finger, David et al. (2012). "Projections of Future Water Resources and Their Uncertainty in a Glacierized Catchment in the Swiss Alps and the Subsequent Effects on Hydropower Production during the 21st Century". In: *Water Resources Research* 48, pp. 1–20. DOI: 10.1029/2011WR010733. URL: http://dx.doi.org/10.1029/2011WR010733.

Franz, Kristie J. et al. (2003). "Verification of National Weather Service Ensemble Streamflow Predictions for Water Supply Forecasting in the Colorado River Basin". In: *Journal of Hydrometeorology* 4.6, pp. 1105–1118. DOI: 10.1175/1525-7541(2003)004<1105:VONWSE>2.0.CO;2. eprint: https://doi.org/10.1175/1525-7541(2003)004<1105:VONWSE>2.0.CO;2. URL: https://doi.org/10.1175/1525-7541(2003)004%3C1105:VONWSE%3E2.0.CO;2.

Fu, Weiwei and Jiang Zhu (2011). "Effects of Sea Level Data Assimilation by Ensemble Optimal Interpolation and 3D Variational Data Assimilation on the Simulation of Variability in a Tropical Pacific Model". In: *Journal of Atmospheric and Oceanic Technology* 28.12, pp. 1624–1640. DOI: 10.1175/JTECH-D-11-00044.1. eprint: https://doi.org/10.1175/JTECH-D-11-00044.1. URL: https://doi.org/10.1175/JTECH-D-11-00044.1.

Grünewald, T. et al. (2010). "Spatial and temporal variability of snow depth and ablation rates in a small mountain catchment". In: *The Cryosphere* 4.2, pp. 215–225. DOI: 10.5194/tc-4-215-2010. URL: https://www.the-cryosphere.net/4/215/2010/.

Harder, Phillip et al. (2016). "Accuracy of Snow Depth Estimation in Mountain and Prairie Environments by an Unmanned Aerial Vehicle". In: *The Cryosphere* 10.6, pp. 2559–2571. DOI: 10.5194/tc-10-2559-2016. URL: http://www.the-cryosphere.net/10/2559/2016/.

Hastie, Trevor, Robert Tibshirani, and Jerome Friedman (2009). *The Elements of Statistical Learning*. Springer New York. DOI: 10.1007/978-0-387-84858-7. URL: https://doi.org/10.1007/978-0-387-84858-7.

Henderson, T.C. et al. (2004). "Snow Monitoring with Sensor Networks". In: *International Conference on Local Computer Networks*. IEEE. Tampa, FL, USA. DOI: 10.1109/LCN.2004.117. URL: https://doi.org/10.1109/LCN.2004.117.

Ho, Michelle et al. (2017). "The Future Role of Dams in the United States of America". In: *Water Resources Research* 53.2, pp. 982–998. ISSN: 1944-7973. DOI: 10.1002/2016WR019905. URL: http://dx.doi.org/10.1002/2016WR019905.

Johnson, Jerome B. et al. (2015). "Performance Characteristics of a New Electronic Snow Water Equivalent Sensor in Different Climates". In: *Hydrological Processes*. DOI: 10.1002/hyp.10211. URL: http://dx.doi.org/10.1002/hyp.10211.

Jorg-Hess, Stefanie, Nena Griessinger, and Massimiliano Zappa (2015). "Probabilistic Forecasts of Snow Water Equivalent and Runoff in Mountainous Areas". In: *Journal of Hydrometeorology* 16.5, pp. 2169–2186. DOI: 10.1175/JHM-D-14-0193.1. eprint: https://doi.org/10.1175/JHM-D-14-0193.1. URL: https://doi.org/10.1175/JHM-D-14-0193.1.

Jost, Georg et al. (2007). "The influence of forest and topography on snow accumulation and melt at the watershed-scale". In: *Journal of Hydrology* 347.1-2, pp. 101–115. DOI: 10.1016/j.jhydrol.2007.09.006. URL: https://doi.org/10.1016/j.jhydrol.2007.09.006.

Justice, C. O. et al. (1998). "The Moderate Resolution Imaging Spectroradiometer (MODIS): land remote sensing for global change research". In: *IEEE Transactions on Geoscience and Remote Sensing* 36.4, pp. 1228–1249. ISSN: 0196-2892. DOI: 10.1109/36.701075.

Kashyap, Abhishek, Samir Khuller, and Mark Shayman (2006). "Relay placement for higher order connectivity in wireless sensor networks". In: *INFOCOM 2006. 25th IEEE International Conference on Computer Communications. Proceedings*. IEEE, pp. 1–12.

Kaurkin, M. N., R. A. Ibrayev, and K. P. Belyaev (2016a). "ARGO data assimilation into the ocean dynamics model with high spatial resolution using Ensemble Optimal Interpolation (EnOI)". In: *Oceanology* 56.6, pp. 774–781. ISSN: 1531-8508. DOI: 10.1134/S0001437016060059. URL: https://doi.org/10.1134/S0001437016060059.

— (2016b). "Data assimilation in the ocean circulation model of high spatial resolution using the methods of parallel programming". In: *Russian Meteorology and Hydrology* 41.7, pp. 479–486. ISSN: 1934-8096. DOI: 10.3103/S1068373916070050. URL: https://doi.org/10.3103/S1068373916070050.

Kerkez, Branko et al. (2012). "Design and Performance of a Wireless Sensor Network for Catchment-scale Snow and Soil Moisture Measurements". In: *Water Resources Research* 48.9, pp. 1–18. DOI: 10.1029/2011WR011214. URL: http://dx.doi.org/10.1029/2011WR011214.

Kirchner, P. B. et al. (2014). "LiDAR measurement of seasonal snow accumulation along an elevation gradient in the southern Sierra Nevada, California". In: *Hydrology and Earth System Sciences* 18.10, pp. 4261–4275. DOI: 10.5194/hess-18-4261-2014. URL: https://www.hydrol-earth-syst-sci.net/18/4261/2014/.

Krajči, Parajka et al. (2017). "The Kühtai Data Set: 25 Years of Lysimetric, Snow Pillow, and Meteorological Measurements". In: *Water Resources Research* 53.6, pp. 5158–5165. ISSN: 1944-7973. DOI: 10.1002/2017WR020445. URL: http://dx.doi.org/10.1002/2017WR020445.

L. Montoya, E, Jeff Dozier, and W Meiring (2014). "Biases of April 1 snow water equivalent records in the Sierra Nevada and their associations with large-scale climate indices". In: *Geophysical Research Letters* 41. DOI: 10.1002/2014GL060588.

Laghari, Javaid (2013). "Climate Change: Melting Glaciers Bring Energy Uncertainty". In: *Nature* 502, pp. 617–18. DOI: 10.1038/502617a. URL: https://www.nature.com/news/climate-change-melting-glaciers-bring-energy-uncertainty-1.14031.

Lapen, David R. and Lawrence W. Martz (1993). "The measurement of two simple topographic indices of wind sheltering-exposure from raster digital elevation models". In: *Computers & Geosciences* 19.6, pp. 769–779. DOI: 10.1016/0098-3004(93)90049-b. URL: https://doi.org/10.1016/0098-3004(93)90049-b.

Lee, Sookyoung and Mohamed Younis (2012). "Optimized relay node placement for connecting disjoint wireless sensor networks". In: *Computer Networks* 56.12, pp. 2788–2804.

Lehning, Michael et al. (2006). "ALPINE3D: a Detailed Model of Mountain Surface Processes and its Application to Snow Hydrology". In: *Hydrological Processes* 20, pp. 2111–2128. DOI: 10.1002/hyp.6204. URL: http://dx.doi.org/10.1002/hyp.6204.

Leppänen, Leena et al. (2016). "Sodankylä Manual Snow Survey Program". In: *Geoscientific Instrumentation, Methods and Data Systems* 5.1, pp. 163–179. DOI: 10.5194/gi-5-163-2016. URL: https://www.geosci-instrum-method-data-syst.net/5/163/2016/.

Liao, Yizheng et al. (2014). "SnowFort: An Open Source Wireless Sensor Network for Data Analytics in Infrastructure and Environmental Monitoring". In: *IEEE Sensors Journal* 14.12, pp. 4253–4263. DOI: 10.1109/JSEN.2014.2358253. URL: https://doi.org/10.1109/JSEN.2014.2358253.

Liu, B. et al. (2016). "Performance measures for systems under multiple environments". In: *IEEE/CAA Journal of Automatica Sinica* 3.1, pp. 90–95. ISSN: 2329-9266. DOI: 10.1109/JAS.2016.7373766.

López-Moreno, J. I. et al. (2014). "Snowpack variability across various spatio-temporal resolutions". In: *Hydrological Processes* 29.6, pp. 1213–1224. DOI: 10.1002/hyp.10245. URL: https://doi.org/10.1002/hyp.10245.

Lundquist, Jessica D., Daniel R. Cayan, and Michael D. Dettinger (2003). "Meteorology and Hydrology in Yosemite National Park: A Sensor Network Application". In: *Information Processing in Sensor Networks*. Ed. by Feng Zhao and Leonidas Guibas. Berlin, Heidelberg: Springer Berlin Heidelberg, pp. 518–528. ISBN: 978-3-540-36978-3.

Lundquist, Jessica D. and Fred Lott (2008). "Using Inexpensive Temperature Sensors to Monitor the Duration and Heterogeneity of Snow-covered Areas". In: *Water Resources Research* 44.4. ISSN: 1944-7973. DOI: 10.1029/2008WR007035. URL: http://dx.doi.org/10.1029/2008WR007035.

Magnusson, Jan et al. (2014). "Assimilation of point SWE data into a distributed snow cover model comparing two contrasting methods". In: *Water Resources Research* 50.10, pp. 7816–7835. DOI: 10.1002/2014WR015302. eprint: https://agupubs.onlinelibrary.wiley.com/doi/pdf/10.1002/2014WR015302. URL: https://agupubs.onlinelibrary.wiley.com/doi/abs/10.1002/2014WR015302.

Malek, S. A., S. D. Glaser, and R. C. Bales (2019). "Wireless Sensor Networks for Improved Snow Water Equivalent and Runoff Estimates". In: *IEEE Access* 7, pp. 18420–18436. ISSN: 2169-3536. DOI: 10.1109/ACCESS.2019.2895397.

Malek, Sami A. et al. (2017). "Real-Time Alpine Measurement System Using Wireless Sensor Networks". In: *Sensors* 17.2583. DOI: 10.3390/s17112583.

Malek, Sami et al. (2017). "Real-Time Alpine Measurement System Using Wireless Sensor Networks". In: *Sensors* 17.11, p. 2583. DOI: 10.3390/s17112583. URL: https://doi.org/10.3390/s17112583.

Margulis, Steven A. et al. (2016). "A Landsat-Era Sierra Nevada Snow Reanalysis (1985–2015)". In: *Journal of Hydrometeorology* 17.4, pp. 1203–1221. DOI: 10.1175/JHM-D-15-0177.1. URL: https://doi.org/10.1175/JHM-D-15-0177.1.

Markstrom, Steven L. et al. (2015).
PRMS-IV, the Precipitation-Runoff Modeling System, Version 4. Tech. rep.
U.S. Geological Survey Techniques and Methods, p. 158. DOI: 10.3133/tm6B7.
URL: http://dx.doi.org/10.3133/tm6B7.

Martinec, Jaroslav et al. (1998). *Snowmelt Runoff Model (SRM) User's Manual*.
University of Berne, Department of Geography.

Mehajabin, Nusrat et al. (2016).
"Energy-sustainable relay node deployment in wireless sensor networks".
In: *Computer Networks* 104, pp. 108–121.

Meyer, J. D. D., J. Jin, and S.-Y. Wang (2012).
"Systematic Patterns of the Inconsistency between Snow Water Equivalent and Accumulated Precipitation as Reported by the Snowpack Telemetry Network".
In: *Journal of Hydrometeorology* 13, pp. 1970–1976. DOI: 10.1175/JHM-D-12-066.1.

Milly, P.C.D. et al. (2008). "Stationarity Is Dead: Whither Water Management?"
In: *Science* 319.February, pp. 573–574. DOI: 10.1126/science.1151915.
URL: http://science.sciencemag.org/content/319/5863/573.

Moeser, C. D. et al. (2011). "79th Annual Western Snow Conference". In:
Proceedings of the 79th Annual Western Snow Conference.
Stateline, NV: Western Snow Conference. Chap. Application of a Wireless Sensor Network for Distributed Snow Water Equivalence Estimation.
URL: sites/westernsnowconference.org/PDFs/2011Moeser.pdf.

Morin, S. et al. (2012). "An 18-yr Long (1993–2011) Snow and Meteorological Dataset from a Mid-altitude Mountain Site (Col de Porte, France, 1325 m alt.) for Driving and Evaluating Snowpack Models". In: *Earth System Science Data* 4.1, pp. 13–21.
DOI: 10.5194/essd-4-13-2012.
URL: http://www.earth-syst-sci-data.net/4/13/2012/.

National Operational Hydrologic Remote Sensing Center. 2004. (2004).
URL: https://doi.org/10.7265/N5TB14TC..

Oroza, Carlos A., Ziran Zhang, et al. (2017). "A Machine-Learning Based Connectivity Model for Complex Terrain Large-Scale Low-Power Wireless Deployments".
In: *IEEE Transactions on Cognitive Communications and Networking* to appear.1.

Oroza, Carlos A., Zeshi Zheng, et al. (2016).
"Optimizing Embedded Sensor Network Design for Catchment-scale Snow-depth Estimation Using LiDAR and Machine Learning".
In: *Water Resources Research* 52.10, pp. 8174–8189. ISSN: 1944-7973.
DOI: 10.1002/2016WR018896. URL: http://dx.doi.org/10.1002/2016WR018896.

Painter, Thomas H. et al. (2016).
"The Airborne Snow Observatory: Fusion of Scanning Lidar, Imaging Spectrometer, and Physically-based Modeling for Mapping Snow Water Equivalent and Snow Albedo".
In: *Remote Sensing of Environment* 184, pp. 139–152. ISSN: 0034-4257.
DOI: http://dx.doi.org/10.1016/j.rse.2016.06.018.
URL: http://www.sciencedirect.com/science/article/pii/S0034425716302577.

Parajka, J. and G. Blöschl (2006).
"Validation of MODIS Snow Cover Images over Austria".
In: *Hydrology and Earth System Sciences* 10.5, pp. 679–689.
DOI: 10.5194/hess-10-679-2006.
URL: http://www.hydrol-earth-syst-sci.net/10/679/2006/.

Pister, Kristofer S. J. and Lance Doherty (2008).
"TMSP: Time synchronized mesh protocol".
In: *Proceedings of the IASTED International Symposium Distributed Sensor Networks*. DSN 2008, pp. 391–398.

Prokop, Alexander et al. (2008).
"A comparison of measurement methods: terrestrial laser scanning, tachymetry and snow probing for the determination of the spatial snow-depth distribution on slopes".
In: *Annals of Glaciology* 49, pp. 210–216. DOI: 10.3189/172756408787814726.
URL: http://dx.doi.org/10.3189/172756408787814726.

Raleigh, Mark S. et al. (2013). "Ground-based testing of MODIS fractional snow cover in subalpine meadows and forests of the Sierra Nevada".
In: *Remote Sensing of Environment* 128, pp. 44–57. ISSN: 0034-4257.
DOI: https://doi.org/10.1016/j.rse.2012.09.016.
URL: http://www.sciencedirect.com/science/article/pii/S0034425712003768.

Reba, Michele L. et al. (2011). "A Long-term Data Set for Hydrologic Modeling in a Snow-Dominated Mountain Catchment". In: *Water Resources Research* 47.7.
ISSN: 1944-7973. DOI: 10.1029/2010WR010030.
URL: http://dx.doi.org/10.1029/2010WR010030.

Revuelto, Jesús et al. (2016). "Combining Snowpack Modeling and Terrestrial Laser Scanner Observations Improves the Simulation of Small Scale Snow Dynamics".
In: *Journal of Hydrology* 533, pp. 291–307. ISSN: 0022-1694.
DOI: http://dx.doi.org/10.1016/j.jhydrol.2015.12.015.
URL: http://www.sciencedirect.com/science/article/pii/S0022169415009634.

Rheinheimer, David E et al. (2014). "Simulating High-Elevation Hydropower with Regional Climate Warming in the West Slope, Sierra Nevada".
In: *Journal of Water Resources Planning and Management* 140.May, pp. 714–723.

DOI: 10.1061/(ASCE)WR.1943-5452.0000373.
URL: http://dx.doi.org/10.1061/(ASCE)WR.1943-5452.0000373.

Rheinheimer, David E. et al. (2016). "Valuing year-to-go hydrologic forecast improvements for a peaking hydropower system in the Sierra Nevada".
In: *Water Resources Research* 52.5, pp. 3815–3828. ISSN: 1944-7973.
DOI: 10.1002/2015WR018295. URL: http://dx.doi.org/10.1002/2015WR018295.

Rice, Robert and Roger C Bales (2010).
"Embedded-sensor network design for snow cover measurements around snow pillow and snow course sites in the Sierra Nevada of California".
In: *Water resources research* 46.3.

Rittger, Karl et al. (2016).
"Spatial estimates of snow water equivalent from reconstruction".
In: *Advances in Water Resources* 94, pp. 345–363. ISSN: 03091708.
DOI: 10.1016/j.advwatres.2016.05.015.

Romanov, Peter., Garik. Gutman, and Ivan Csiszar (2000). "Automated Monitoring of Snow Cover over North America with Multispectral Satellite Data".
In: *Journal of Applied Meteorology* 39, pp. 1866–1880.
DOI: 10.1175/1520-0450(2000)039<1866:AMOSCO>2.0.CO;2. URL:
http://dx.doi.org/10.1175/1520-0450(2000)039%3C1866:AMOSCO%3E2.0.CO;2.

Rosenberg, Eric A., Andrew W. Wood, and Anne C. Steinemann (2011). "Statistical applications of physically based hydrologic models to seasonal streamflow forecasts".
In: *Water Resources Research* 47.3, n/a–n/a. ISSN: 1944-7973.
DOI: 10.1029/2010WR010101. URL: http://dx.doi.org/10.1029/2010WR010101.

Ryan, Wendy A, Nolan J Doesken, and Steven R Fassnacht (2008).
"Evaluation of Ultrasonic Snow Depth Sensors for U.S. Snow Measurements".
In: *Journal of Atmospheric and Oceanic Technology* 25, pp. 667–684.
DOI: 10.1175/2007JTECHA947.1. URL: https://doi.org/10.1175/2007JTECHA947.1.

Schirmer, M. et al. (2011). "Persistence in intra-annual snow depth distribution: 1. Measurements and topographic control". In: *Water Resources Research* 47.9.
DOI: 10.1029/2010WR009426. eprint:
https://agupubs.onlinelibrary.wiley.com/doi/pdf/10.1029/2010WR009426.
URL: https://agupubs.onlinelibrary.wiley.com/doi/abs/10.1029/2010WR009426.

Schneider, D., N. P. Molotch, and J. S. Deems (2017).
"Estimating relationships between snow water equivalent, snow covered area, and topography to extend the Airborne Snow Observatory dataset".
In: *The Cryosphere Discussions* 2017, pp. 1–29. DOI: 10.5194/tc-2017-167.
URL: https://www.the-cryosphere-discuss.net/tc-2017-167/.

Schneider, Dominik and Noah P. Molotch (2016).
"Real-time estimation of snow water equivalent in the Upper Colorado River Basin using MODIS-based SWE Reconstructions and SNOTEL data".
In: *Water Resources Research* 52.10, pp. 7892–7910. DOI: 10.1002/2016WR019067.
eprint:
https://agupubs.onlinelibrary.wiley.com/doi/pdf/10.1002/2016WR019067.
URL: https://agupubs.onlinelibrary.wiley.com/doi/abs/10.1002/2016WR019067.

Serreze, Mark C. et al. (1999). "Characteristics of the Western United States Snowpack from Snowpack Telemetry (SNOTEL) Data".
In: *Water Resources Research* 35.7, pp. 2145–2160. DOI: 10.1029/1999WR900090.
URL: http://dx.doi.org/10.1029/1999WR900090.

Skalka, Christian and Jeffrey Frolik (2014).
"Snowcloud: A Complete Data Gathering System for Snow Hydrology Research". In: *Real-World Wireless Sensor Networks: Proceedings of the 5th International Workshop, REALWSN 2013, Como (Italy), September 19-20, 2013*. Ed. by Koen Langendoen et al. Cham: Springer International Publishing, pp. 3–14. ISBN: 978-3-319-03071-5.
DOI: 10.1007/978-3-319-03071-5_1.
URL: https://doi.org/10.1007/978-3-319-03071-5_1.

SmartMesh IP Application Notes (2017). Rev. 15. Linear Technology.

Stewart, Iris T., Daniel R. Cayan, and Michael D. Dettinger (2004).
"Changes in Snowmelt Runoff Timing in Western North America under a 'Business as Usual' Climate Change Scenario". In: *Climatic Change* 62.1, pp. 217–232.
ISSN: 1573-1480. DOI: 10.1023/B:CLIM.0000013702.22656.e8.
URL: https://doi.org/10.1023/B:CLIM.0000013702.22656.e8.

— (2005). "Changes toward Earlier Streamflow Timing across Western North America".
In: *Journal of Climate* 18.8, pp. 1136–1155. DOI: 10.1175/JCLI3321.1.
eprint: https://doi.org/10.1175/JCLI3321.1.
URL: https://doi.org/10.1175/JCLI3321.1.

Stigter, E. E. et al. (2017). "Assimilation of snow cover and snow depth into a snow model to estimate snow water equivalent and snowmelt runoff in a Himalayan catchment".
In: *The Cryosphere* 11.4, pp. 1647–1664. DOI: 10.5194/tc-11-1647-2017.
URL: https://www.the-cryosphere.net/11/1647/2017/.

Sturm, Matthew (2015).
"White Water: Fifty Years of Snow Research in WRR and the Outlook for the Future".
In: *Water Resources Research* 51, pp. 4948–4965. DOI: 10.1002/2015WR017242.
URL: http://dx.doi.org/10.1002/2015WR017242.

Sturm, Matthew and Michael A Goldstein (2017).
"Water and Life from Snow: A Trillion Dollar Science Question".

In: *Water Resources Research* 53, pp. 3534–3544.
DOI: 10.1002/2017WR020840.Received.
URL: http://dx.doi.org/10.1002/2017WR020840.Received.

Sun, Chaojiao, Jeffrey P. Walker, and Paul R. Houser (2004).
"A methodology for snow data assimilation in a land surface model".
In: *Journal of Geophysical Research: Atmospheres* 109.D8.
DOI: 10.1029/2003JD003765. eprint:
https://agupubs.onlinelibrary.wiley.com/doi/pdf/10.1029/2003JD003765.
URL: https://agupubs.onlinelibrary.wiley.com/doi/abs/10.1029/2003JD003765.

Varhola, Andres et al. (2010).
"A New Low-Cost, Stand-Alone Sensor System for Snow Monitoring".
In: *Journal of Atmospheric and Oceanic Technology* 27.12, pp. 1973–1978.
DOI: 10.1175/2010JTECHA1508.1.
eprint: https://doi.org/10.1175/2010JTECHA1508.1.
URL: https://doi.org/10.1175/2010JTECHA1508.1.

Watteyne, Thomas, Ana Laura Diedrichs, et al. (2016).
"PEACH: Predicting Frost Events in Peach Orchards Using IoT Technology".
In: *EAI Endorsed Transactions on the Internet of Things* 1.2016.
DOI: 10.4108/eai.1-12-2016.151711.
URL: http://dx.doi.org/10.4108/eai.1-12-2016.151711.

Watteyne, Thomas, Lance Doherty, et al. (2013). *Technical overview of SmartMesh IP*.

Watteyne, Thomas, Ankur Mehta, and Kris Pister (2009).
"Reliability Through Frequency Diversity: Why Channel Hopping Makes Sense".
In: *International Symposium on Performance Evaluation of Wireless Ad Hoc, Sensor, and Ubiquitous Networks (PE-WASUN)*. ACM. Tenerife, Canary Islands, Spain.

Watteyne, Thomas, Xavier Vilajosana, et al. (2012).
"OpenWSN: a standards-based low-power wireless development environment".
In: *Transactions on Emerging Telecommunications Technologies* 23.5, pp. 480–493.
ISSN: 2161-3915. DOI: 10.1002/ett.2558.
URL: http://dx.doi.org/10.1002/ett.2558.

Watteyne, Thomas, Joy Weiss, et al. (2015).
"Industrial IEEE802.15.4e Networks: Performance and Trade-offs".
In: *IEEE International Conference on Communications (IEEE ICC), Internet of Things Symposium*. London, UK, pp. 604–609. DOI: 10.1109/ICC.2015.7248388.
URL: https://doi.org/10.1109/ICC.2015.7248388.

Welch, Stephen C. et al. (2013). "Sensor placement strategies for snow water equivalent (SWE) estimation in the American River basin".

In: *Water Resources Research* 49.2, pp. 891–903. DOI: 10.1002/wrcr.20100. URL: https://doi.org/10.1002/wrcr.20100.

Wever, N. et al. (2015). "Verification of the Multi-layer SNOWPACK Model with Different Water Transport Schemes". In: *The Cryosphere* 9.6, pp. 2271–2293. DOI: 10.5194/tc-9-2271-2015. URL: http://www.the-cryosphere.net/9/2271/2015/.

Wilson, Margaret F. J. et al. (2007). "Multiscale Terrain Analysis of Multibeam Bathymetry Data for Habitat Mapping on the Continental Slope". In: *Marine Geodesy* 30.1-2, pp. 3–35. DOI: 10.1080/01490410701295962. URL: https://doi.org/10.1080/01490410701295962.

Winstral, Adam, Kelly Elder, and Robert E. Davis (2002). "Spatial Snow Modeling of Wind-Redistributed Snow Using Terrain-Based Parameters". In: *Journal of Hydrometeorology* 3.5, pp. 524–538. DOI: 10.1175/1525-7541(2002)003<0524:SSMOWR>2.0.CO;2. eprint: https://doi.org/10.1175/1525-7541(2002)003<0524:SSMOWR>2.0.CO;2. URL: https://doi.org/10.1175/1525-7541(2002)003%3C0524:SSMOWR%3E2.0.CO;2.

Xia, C., W. Liu, and Q. Deng (2015). "Cost minimization of wireless sensor networks with unlimited-lifetime energy for monitoring oil pipelines". In: *IEEE/CAA Journal of Automatica Sinica* 2.3, pp. 290–295. ISSN: 2329-9266. DOI: 10.1109/JAS.2015.7152663.

Xu, Jianhui and Hong Shu (2014). "Assimilating MODIS-based albedo and snow cover fraction into the Common Land Model to improve snow depth simulation with direct insertion and deterministic ensemble Kalman filter methods". In: *Journal of Geophysical Research: Atmospheres* 119.18, pp. 10, 684–10, 701. DOI: 10.1002/2014JD022012. eprint: https://agupubs.onlinelibrary.wiley.com/doi/pdf/10.1002/2014JD022012. URL: https://agupubs.onlinelibrary.wiley.com/doi/abs/10.1002/2014JD022012.

Zhang, Ziran, Steven D. Glaser, Roger C. Bales, Conklin Martha, and Marks Daniel (2017). "Technical Report: The Design and Evaluation of a Basin-scale Wireless Sensor Network for Mountain Hydrology". In: *Water Resources Research* 53, pp. 4487–4498. DOI: 10.1002/2016WR019619. URL: http://dx.doi.org/10.1002/2016WR019619.

Zhang, Ziran, Steven D. Glaser, Roger C. Bales, Conklin Martha, Rice Robert, et al. (2017). "Insights into Mountain Precipitation and Snowpack from a Basin-scale Wireless Sensor Network". In: *Water Resources Research* 53. DOI: 10.1002/2016WR018825. URL: http://dx.doi.org/10.1002/2016WR018825.

Zhang, Ziran, Steven D. Glaser, Thomas Watteyne, et al. (2016). "Long-term Monitoring of the Sierra Nevada Snowpack Using Wireless Sensor Networks". In: *IEEE Internet of Things Journal* to appear, pp. 1–9.

Zheng, Zeshi et al. (2018). "Spatial snow water equivalent estimation for mountainous areas using wireless-sensor networks and remote-sensing products". In: *Remote Sensing of Environment* 215, pp. 44–56. ISSN: 0034-4257. DOI: https://doi.org/10.1016/j.rse.2018.05.029. URL: http://www.sciencedirect.com/science/article/pii/S0034425718302578.

Zou, Hui and Trevor Hastie (2005). "Regularization and variable selection via the elastic net". English (US). In: *Journal of the Royal Statistical Society. Series B: Statistical Methodology* 67.2, pp. 301–320. ISSN: 1369-7412. DOI: 10.1111/j.1467-9868.2005.00503.x.

Appendix A

PRISM and features

This section contains Fig. A.1 showing PRISM 30-year annual precipitation normal in inches covering the period from 1981 to 2010.

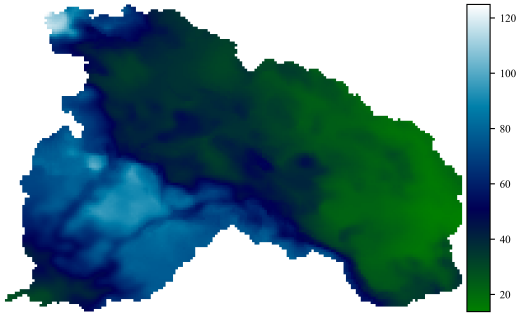

Figure A.1: PRISM 30-year annual precipitation normal in inches covering period from 1981 to 2010.

A.1 Feature details

This section contains the Table A.1 describing the source of each feature used in the analysis.

Table A.1: Source of features used in Elastic Net regression.

Feature Name	Source
elevation	USGS National Elevation Dataset (NED)
canopy	National Land Cover Database (NLCD), Percent Tree Canopy Collection
aspect	f(slope)
longitude	N/A
sur-canopy	f(canopy)
inorth	f(elevation): raking northern light hillshade
isouth	f(elevation): raking southern light hillshade
ieast	f(elevation): raking eastern light hillshade
iwest	f(elevation): raking western light hillshade
hillshade	f(elevation): south east 45 degree high incident light hillshade
TPI	f(elevation): Topographic Position Index
TPI100	f(elevation down-sampled to 100m)
roughness	f(elevation) Wilson et al. 2007
nnMarg	Margulis published dataset Margulis et al. 2016
northness	cos(aspect)